BOEING SCIENTIFIC RESEARCH LABORATORIES DOCUMENT NAS 7-489

BOEING

SCIENTIFIC RESEARCH LABORATORIES

Stress Corrosion Cracking of Titanium Alloys: Electrochemical Mass-Transport-Kinetic Model, Metallurgical and Mechanical Effects, and Proposed Relation of Electrochemical, Metallurgical and Mechanical Effects

T. R. Beck

M. J. Blackburn

Quarterly Progress Report No. 4
for Period of
April 1, 1967 through June 30, 1967

CONTRACT NAS 7-489

SOLID STATE PHYSICS LABORATORY JUNE 1967

CONTRACT NAS 7-489

Stress Corrosion Cracking of Titanium Alloys:

Electrochemical Mass-Transport-Kinetic Model, Metallurgical and Mechanical Effects, and Proposed Relation of Electrochemical, Metallurgical and Mechanical Effects

Quarterly Progress Report ~~No.~~ 4

for Period of

April 1, ~~1967 through~~ June 30, 1967

Prepared by

T. R. Beck

and

M. J. Blackburn

Solid State Physics Laboratory

Boeing Scientific Research Laboratories

Seattle, Washington 98124

TABLE OF CONTENTS

		Page
1.0	SUMMARY	1
2.0	INTRODUCTION	2
3.0	TECHNICAL DISCUSSION	4
	3.1 Electrochemical Mass-Transport-Kinetic Models	4
	3.2 Metallurgical and Mechanical Effects	46
	3.3 Proposed Relation of Electrochemical, Metallurgical and Mechanical Effects	107
4.0	CONCLUSIONS	113
5.0	FUTURE WORK	115
6.0	REFERENCES	116
7.0	APPENDIX	118
	A. Nomenclature	118
	B. Extraction of Chloride from Metal	121
	C. Derivation of Equation for Simple Hydrolysis Model	123

1.0 SUMMARY

A continuum electrochemical mass-transport-kinetic model has been formulated and computations have been made on a digital computer, giving results that appear to be consistent with velocity-current-potential data for duplex annealed Ti:8-1-1. The model predicts that the electrochemically controlled velocity is determined by mass transport of chloride, bromide or iodide ions to the crack tip. The tip current is equivalent to formation of an adsorbed monolayer of halide ions or titanium halide. Data on the relation of velocity to bulk halide ion concentration indicates that a recycling of halide ions by displacement or hydrolysis occurs near the tip. Many similarities are observed to the previously proposed model for pitting corrosion of titanium.

Ti:8-1-1 heat treated to a very brittle condition and Ti-Al alloys after similar heat treatment give stress corrosion cracking velocities greater than predicted from the electrochemical model, indicating an additional mechanical mode of fracture. This mechanical mode is related to rate of change of stress intensity. The velocity in the electrochemical mode appears to be related linearly to stress intensity factor, perhaps through changes in crack angle. Ti:8-1-1 heat treated to a ductile condition gives stress corrosion cracking velocities less than predicted from the electrochemical model. It is proposed that ductile (non-susceptible) phases retard crack propagation in this case.

2.0 INTRODUCTION

This report describes part of a study of stress corrosion cracking of titanium alloys initiated in July 1965 (1) and continued under NASA sponsorship beginning July 1966 (2). This is the fourth Quarterly report in the series (3) and covers the period April 1 through June 30, 1967. The contribution on metallurgical and mechanical effects in this report was made by Dr. M. J. Blackburn, who is in part supported by the present program. The assistance of J. C. Williams is acknowledged. Professor E. A. Grens II of Berkeley, worked with T. R. Beck on the formulation and the implementation of the mass-transport-kinetic model for SCC velocity (4) and his services are acknowledged.

As this report marks the completion of the first year of work on the contract, it is appropriate to measure the progress against the original work statements (2). The work statements and the work completed are listed below.

1. "Determine electrochemical polorization curves for a variety of alloys and heat treatments and electrolyte compositions". It was determined in the precontract studies (1) that polarization curves for oxide-covered titanium had little relation to the SCC problem except that under open-circuit conditions the anodic current for SCC propagation may come from cathodic reactions on the exterior surface of the specimens. Effort has therefore been concentrated on the more relevant processes of, oxidation of, or hydrogen ion reduction on, newly generated titanium alloy surfaces. Various

salt solution environments have been investigated using mill-annealed Ti:8-1-1 alloy. Further work is planned with other alloys and environments.

2. "Conduct tensile tests with notched specimens of a variety of titanium alloys and heat treatments in electrolyte environments at controlled potentials based on 1 ." The bulk of the experimental work has been conducted under these conditions. Ti:8-1-1 and Ti-Al binary alloys with various heat treatments have been investigated. Further work is planned with other alloys.
3. "Conduct a limited number of engineering tests on standard precracked specimens of selected alloys and heat treatments at selected electrolyte environment compositions and potentials based on 2 ." Four point bend tests on 1/2 inch thick specimens of Ti:8-1-1 alloy have been made. The results are consistent with data on the smaller notched specimens and very limited further testing of the larger specimens is planned.
4. "Conduct applicable physical, metallurgical and chemical examinations including determination of fracture path." Work done to satisfy this objective includes, electron fractography, determination of cleavage plane, studies of dislocation arrangements and slip modes, phase studies, collection of chemical analyses and physical properties, tensile and strain rate tests, and analyses for chlorine. Further analyses will be conducted as required to provide data for test of the theoretical models.

5. "Conduct theoretical analysis of mechanisms in conjunction with 1 through 4 ." A continuum electrochemical mass-transport-kinetic model has been formulated, that appears to fit the observed relation of velocity to potential and with modification, to salt concentration. Some tentative relations to metallurgy and mechanics are proposed. A more rigorous formulation of metallurgical and mechanical effects and further definitive experiments are planned to test the models.

3.0 TECHNICAL DISCUSSION

3.1 Electrochemical Mass-Transport-Kinetic Models

In this section, several models for describing the electrochemical mass transport and kinetic phenomena are described and compared to experimental data.

3.1.1 Preliminary IR Drop Model

The preliminary IR drop model was proposed to explain the linear relationship between crack propagation velocity and applied potential and between the associated anodic current and potential (1). Each line had an intercept at about -800 to -900 mv and it was assumed that this intercept was the potential at the tip of the crack. The difference between the applied potential and this intercept could therefore be interpreted as the potential drop in the crack. The kinetic data for growth of multilayers of oxide on a plane surface as illustrated in Fig. 1 (1), showed a very rapid decay of current density with time.

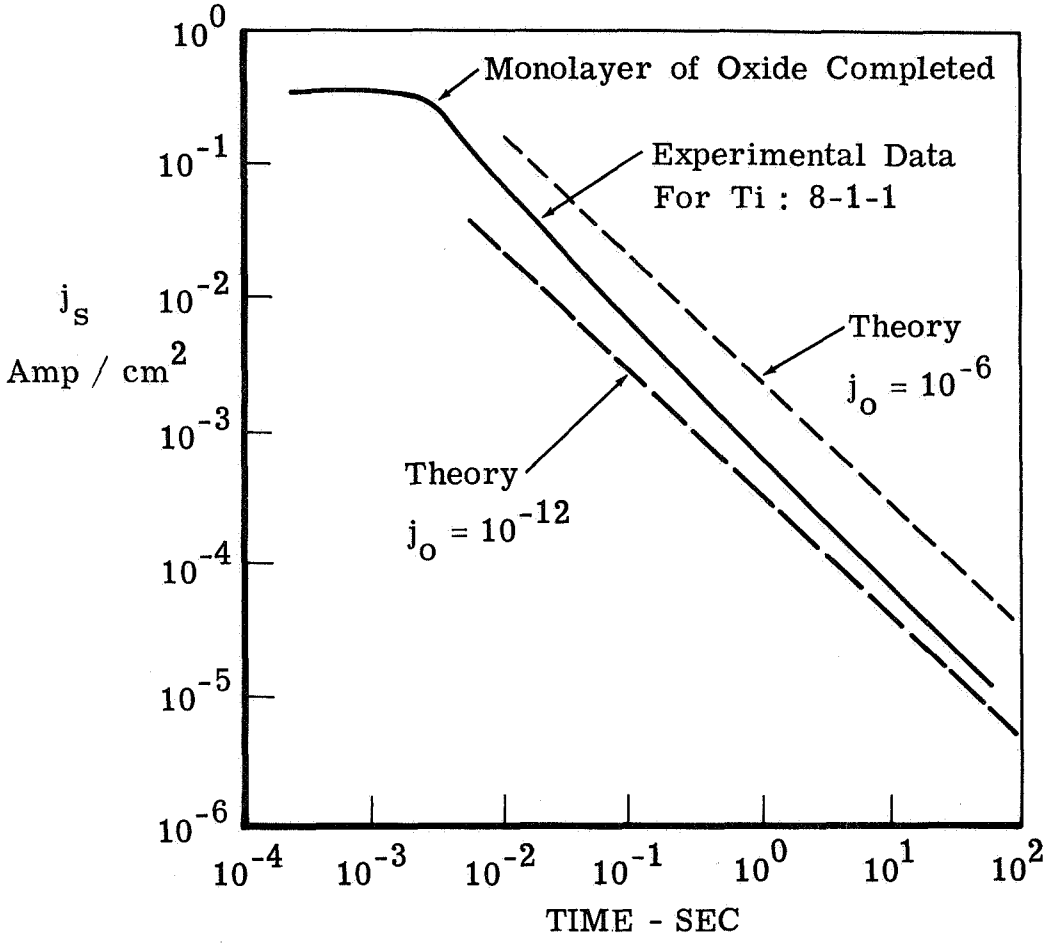

FIG. 1 Kinetic Data for Growth of Oxide on Ti:8-1-1 Alloy (1)

Applied to a propagating crack, the kinetic data indicated that most of the anodic current would flow most of the way into the crack. Assuming a constant current, a constant angle, and a constant conductivity electrolyte, the resistance of the electrolyte would be (1):

$$R_e = \frac{\rho}{w\gamma} \ln (\ell/\delta) \qquad \text{Equation 1}$$

The resistance calculated from the slope of the current versus potential plot for a 0.127 cm thick specimen with about a 0.1 cm crack length was about 18,000 ohms (1). Assuming a bulk electrolyte resistivity of 20 ohm cm (for 0.6 M KCl solution) and a crack angle of 0.05 radians (approximately 3 degrees observed) requires that $\ln(\frac{\ell}{\delta})$ be about 5 or that $\frac{\ell}{\delta}$ be on the order of 100. This appeared to be a reasonable value assuming $= 10^{-2}$ cm, i.e., about $^1/10$ the specimen thickness 0.12 cm (0.050 in.) where appreciable current enters from the sides of the crack; and $= 10^{-4}$ cm. The value of δ could not be defined a priori with precision but it must certainly be larger than 10^{-6} to 10^{-5} cm from the geometric apex because this is the zone where the electrical double layers on the walls of the crack would intersect in a 3° crack. A finite time would be required for the first monolayer to form, so $\delta = 10^{-4}$ cm would appear to be the right order of magnitude.

This simple model also gave the right order of magnitude for total current. The current required to form the first monolayer on the two walls is:

$$I_M = 2\, Q_o V \,. \qquad \text{Equation 2}$$

The current to build up multilayers of oxide is:

$$I_W = 2 \int_{\delta}^{\ell} i \, dy \qquad \text{Equation 3}$$

But from Fig. 1:

$$i \approx \frac{A}{\tau} \qquad \text{Equation 4}$$

The age of the surface at a point y distance from the geometric apex is:

$$\tau(y) = y/V \qquad \text{Equation 5}$$

Eliminating i and τ from Equations 3, 4, and 5 gives:

$$I_W \approx 2 \, A \, V \, \ell n \, (\ell/\delta) \qquad \text{Equation 6}$$

The total current is therefore:

$$I \approx 2V \, [Q_o + AV \, \ell n(\ell/\delta)] \qquad \text{Equation 7}$$

Assuming $Q_o = 425 \times 10^{-6}$ coul/cm^2 [1], $A \approx 10^{-3}$ coul/cm^2 (experimental data, Fig. 1), and $\ell n(\ell/\delta) = 5$ (as from the calculation of resistance) gives $\frac{\Delta I}{\Delta V} \approx 1.08 \times 10^{-2}$. This again is the right order of magnitude in respect to the experimental data.

The simple model, although it gave order of magnitude agreement with experiment, was deficient in several respects; such as, it neglected the effect of potential gradient on kinetics of oxidation and the effects of changes in electrolyte concentration in the crack on resistance. Therefore, a more rigorous analysis was formulated, which was outlined in a previous report (3, 2nd Quarterly) and paper (4).

3.1.2 More Rigorous Mass-Transport-Kinetic Model

Fig. 2 shows the more rigorous mass-transport-kinetic model of the propagating SCC and definitions of some of the terms. There is a uniform, small-angle crack with angle, γ, propagating at a velocity, V, through the material. A moving set of coordinates was chosen with the zero at the geometric apex of the crack. This system has the advantage that the wedge of electrolyte can be considered to be in plug flow moving with the apex at a velocity, V, and a quasi-steady-state approximation can be made. The convection term in the mass-transport equations can also be neglected.

The lower boundary of the mass-transport model is δ^P, where the two double layers on the walls intersect. From δ^P to δ there is a zone in which the first monolayer of oxide is formed on the walls. At δ the oxide coverage, θ, is equal to unity. From δ to ℓ multilayers of oxide are formed. The length ℓ is defined as that distance at which appreciable current begins to flow in from the sides of the crack rather than axially down the crack. The length ℓ was considered to be about 1/10 the thickness of the specimen. At point y from the

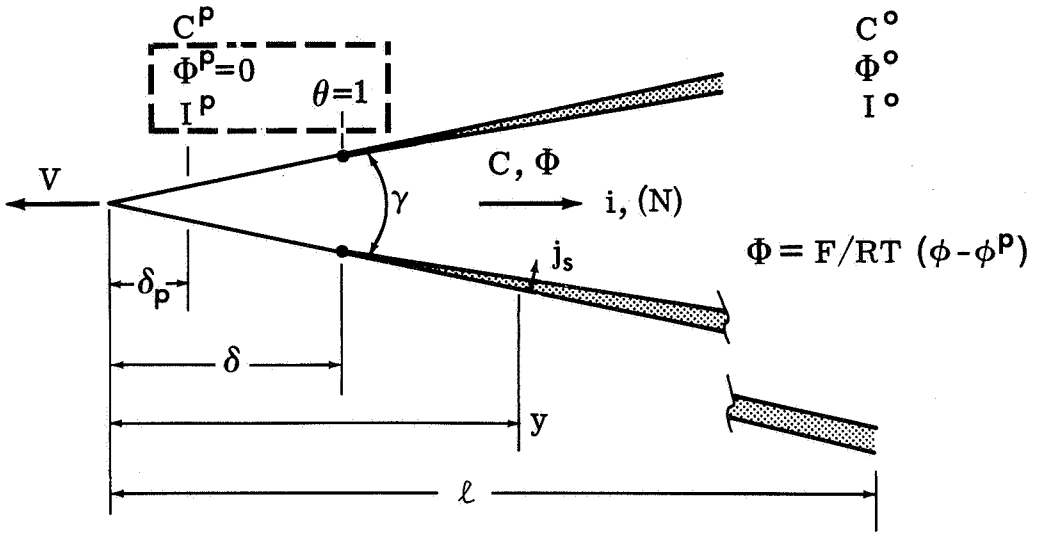

FIG. 2 Mass Transport - Kinetic Model for SCC

geometric apex there is a surface current density for oxidation, j_s , and a nondimensionalized potential in the electrolyte, Φ . The potential was nondimensionalized with $\frac{F}{RT}$ and referenced to the potential at δ^p . There is a concentration in the electrolyte, C, and a current density in the cross section of the crack, i, which is related to the fluxes of the various ions, N. In this one-dimensional model, no gradients were considered across the width of the crack.

There is one equation for j_s in the distance δ^p to δ where bare metal is oxidized and another equation for j_s in the region δ to ℓ where multilayers of oxide are forming. The boundary conditions at δ^p are $\Phi = 0$ and I^p equals the tip current; and at $y = \delta$ θ is unity. The problem is solved by the Runge-Cutta-Gill numerical integration procedure implemented on a digital computer, iterating until the concentration at ℓ converges to the bulk concentration. Calculations give the concentration at the tip and the potential and current density at ℓ .

The system of equations used in the model is given in Table I. It is beyond the scope of this paper to explain all of the equations (the model is described fully in Reference 4 to be published), but a few comments are required. It is assumed that the only wall reactions are oxidation of titanium by water and hydrogen ion reduction. Therefore the alkali metal cation from the bulk solution is not reacted and its current is zero at all positions in the crack. The halide was assumed to be not involved in the wall reactions but may be involved at the crack tip so its current is zero or a constant. The hydrogen ion current varies with position and depends on the rates of the wall reactions.

Table I: System of Equations used in Mass-Transport-Kinetic Model

Flux Equations:

$$N_+ = -D_+ \frac{dC_+}{dy} - z_+ D_+ C_+ \frac{d\Phi}{dy} = 0$$

$$N_- = -D_- \frac{dC_-}{dy} - z_- D_- C_- \frac{d\Phi}{dy}$$

$$N_H = -D_H \frac{dC_H}{dy} - z_H D_H C_H \frac{d\Phi}{dy}$$

Equation 8

Electroneutrality: $\sum z\ C = 0$ Equation 9

Relation of current density and fluxes: $i = F \sum z\ N$ Equation 10

Relation of total current to current density: $I = i\ \gamma\ y$ Equation 11

Mass Balance: $dI = \gamma\ (i\ dy + y\ di) = 2\ j\ dy$ Equation 12

Kinetic Equations:

$$j = j_s - j_H$$ Equation 13

$$@\ \delta \leqslant y \leqslant \ell,\ j_s = j_o \exp\left\{\frac{B(\Phi-\Phi_e-X)}{\frac{K}{V}\int_{\delta}^{y} p\ j_s\ dy}\right\}$$ Equation 14

$$j_H = 0$$ Equation 15

$$@\ \delta^p \leqslant y \leqslant \delta,\ j_s = i_m(1-\theta)\ \exp\{\tfrac{n}{2}\ (\Phi-\Phi_e)\} + j_o\ \theta \exp\left\{\frac{B(\Phi-\Phi_e-X)}{t_o}\right\}$$

$$j_H = i_H\ (i-\theta)\ \exp\{\tfrac{1}{2}(\Phi-\Phi_H)\}$$ Equation 16

Table I (continued)

Definition of Surface Overpotential, X:	$j_s = i_o \, 2 \sinh \{\frac{n'}{2} X\}$	Equation 17
Definition of θ:	$\theta = \frac{1}{Q_o V} \int_{\delta p}^{y} j_s \, dy$	Equation 18

Values of the parameters used in the solution are given in Table II. All of the parameters except γ, δ^P and ℓ came from sources independent of the SCC experiments. The diffusivities are approximate values. The angle γ is the approximate value observed on the surface of specimens with propagating cracks. The exchange current densities are order of magnitude values estimated from the electrochemical kinetics experiments (3, 2nd Quarterly). The value of B in the high-field conduction equation came from Johansen et.al., (5). The value of K was calculated from the density of bulk rutile. The reversible potentials for oxidation and hydrogen ion reduction were from Latimer (6), converted to the SCE scale, and nondimensionalized. The charge density of a monolayer of oxide is based on one oxide ion per titanium atom in the basal plane (1). The value of δ^P is based on the minimum double layer thickness of 2.5 Å on each wall and the angle of 0.05 radians. The value of ℓ is 1/10 of a unit thickness specimen.

The first calculations were made before the kinetic data for hydrogen ion reduction on bare metal were available and i_H was assumed zero. The potential of the tip was assumed to be -900 mv or 35 in dimensionless form. (This is the zero potential in the calculations.) The tip current, being unknown, was assumed to be zero. A typical velocity of 10^{-2} cm/sec was chosen for the initial calculation. The experimental values of current and potential (1) for this velocity are respectively about 200 μA/cm and -400 mv or -20 in dimensionless form referenced to the tip potential.

Table II: Values of Parameters used in Mass Transport - Kinetic Model

$D_+ = 1 \times 10^{-5}$ cm^2/sec

$D_- = 1 \times 10^{-5}$ cm^2/sec

$D_H = 6 \times 10^{-5}$ cm^2/sec

$z_+ = +1$

$z_- = -1$

$z_H = +1$

γ = 0.05 radians (3 degrees)

$i_H = 2 \times 10^{-8}$ amp/cm^2 (or zero)

$i_m = 2 \times 10^{-3}$ amp/cm^2

$i_o = 2 \times 10^{-3}$ amp/cm^2

$j_o = 10^{-12}$ to 10^{-6} amp/cm^2

$n = -1$

$n' = 1$

$B = (6 \times 10^{-6}$ cm/volt)/ $\frac{F}{RT}$

$K = 4.85 \times 10^{-5}$ cm^3/coul

Φ_e = 40 (dimensionless potential)

Φ_H = 7 (dimensionless potential)

$Q_o = 425 \times 10^{-6}$ coul/cm^2

$\delta^p = 10^{-6}$ cm

$\ell = 10^{-1}$ cm

Of the kinetic parameters used in the calculations, j_o had the dominant effect and the lower and upper bound levels of 10^{-12} and 10^{-6} amps/cm^2 from Fig. 1 were used. As shown in Table III, a 10^{-6} fold variation of j_o only gives a 4-fold change in the current and about a 2-fold change in the potential. The reason for this is that the higher the value of j_o the faster a resistive oxide layer is built up thus limiting the current. Also the faster the oxide layer is formed, the greater the rate of generation of hydrogen ion and the higher the conductivity of the electrolyte and therefore, the smaller the potential change. Calculated currents approach the same order of magnitude as obtained by experiment, but the potential is at least 20 fold too low. The reason for this is that the hydrogen ion carries most of the current in the model and hydrogen ion concentration increases continually toward the tip when there is no hydrogen ion discharge. On the first iteration of the calculations using constant bulk solution conductivity the computer solution gave about the same potential as the experiments, but when the concentration was allowed to build up and hydrogen ion carried the current, the potential was too low.

At this point it became apparent that a lower conductivity must be obtained in the crack in order to obtain potentials compatible with experimental results. The only way that this could be accomplished in the model was to have some process which would make the concentration decrease. The only feasible way to accomplish this appeared to be to have

Table III: Initial Results

For $V=10^{-2}$ cm/sec,
($i_H = 0$ and $I^p=0$ in calc)

	j_o	$I°$ - μA/cm	$\Phi°$
Exp.	---	200	-20
Calc.	10^{-12}	30	-0.5
	10^{-6}	120	-1.0

a mass-transport limiting current density at δ^p such that the concentration at δ^p would approach a very low level. By trail and error it was found that a tip current of 7.2 amp/cm was close to the value of the limiting current, as it gave a concentration of halide ion at δ^p about one-thousandth that of the bulk solution. Results are shown in Table IV and plots of flux, potential and concentration versus position in the crack are shown in Fig. 3. The potential is approaching the right order of magnitude and can be increased further by approaching the limiting more closely thus giving a lower concentration at δ^p.

There are several important implications of this requirement for a limiting current:

1. The halide ion tip current either goes to charge the electrical double layer or to an electrochemical reaction consuming halide ions within the tip zone (i.e., @ $y \leq \delta^p$).
2. The rate of hydrogen ion discharge within the tip zone must be small because if the hydrogen ion current were of comparable value to the halide ion current there would be no potential gradient. This would appear to exclude the hydride mechanism.
3. The limiting tip current corresponds to the order of magnitude for one monolayer adsorbed halide ions or of titanium dihalide, the thermodynamically stable form at the tip potential. The tip current can be defined as:

$$I^p = 2nQ_x V. \qquad \text{Equation 19}$$

Table IV: Results with Inclusion of Hydrogen Ion Discharge Mechanism and Limiting Tip Current

Conditions:

$V = 10^{-2}$ cm/sec

$i_H = 2 \times 10^{-8}$ amp/cm^2

$j_o = 10^{-8}$ amp/cm^2

Results:

$I° = 270$ μA/cm

$I^P = 7.2$ μA/cm

$\Phi° = -4.6$

$C_-^P/C_-^\circ = 10^{-3}$

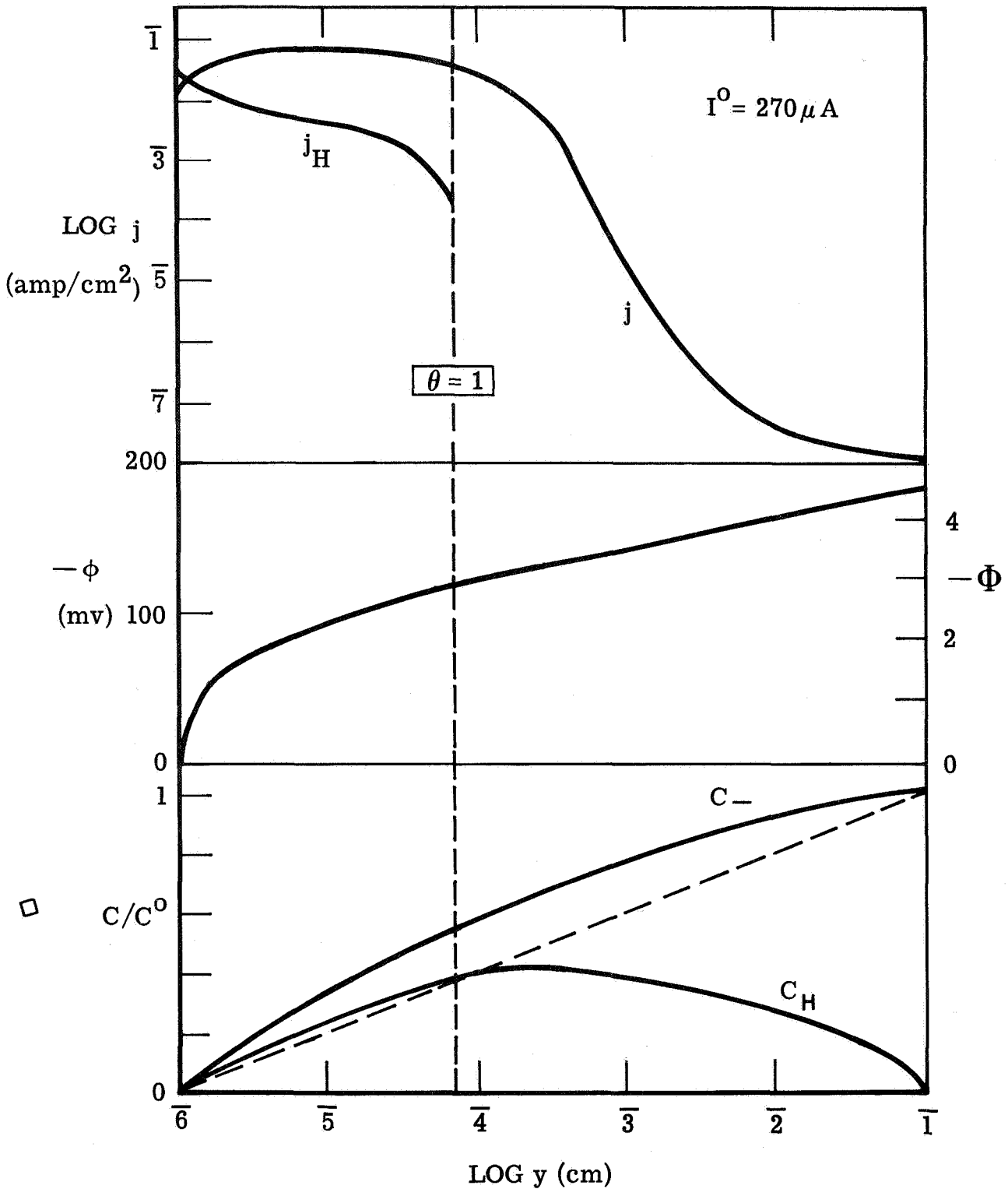

FIG. 3 Calculated Current Density, Potential and Concentration as a Function of Position in a Propagating Stress Corrosion Crack

For I^p = 7.2 μAmp/cm, Q_x = 425 μAmp/cm^2 (for dihalide) and V = 10^{-2} cm/sec; n = 0.85 of a monolayer.

3.1.3 Experimental Tests of Model

(a) Time Constant

The mass-transport-kinetic model predicts that the potential gradient in the crack can be accounted for by concentration polarization. Potential transients on open circuits were measured to test this prediction. Epoxy coated specimens were used in order to limit the electrochemical reactions to the new surface formed in the crack. A crack was propagated at -500 MV in 0.6 M KI solution, the current open circuited and the potential recorded as a function of time, as shown in Figure 4. The time required to reach the new steady-state potential recorded as a function of time, is shown in Figure 4. The time required to reach the new steady-state potential at open circuit was about 20 seconds. It was not clear from the strip-chart record if there was any appreciable IR contribution to the initial potential so a Polaroid photograph was taken of a 500 millisec oscilloscope trace. The potential decay data, plotted against a logorithmic time scale in Fig. 5 indicates essentially no IR component. (In contrast, the relatively large

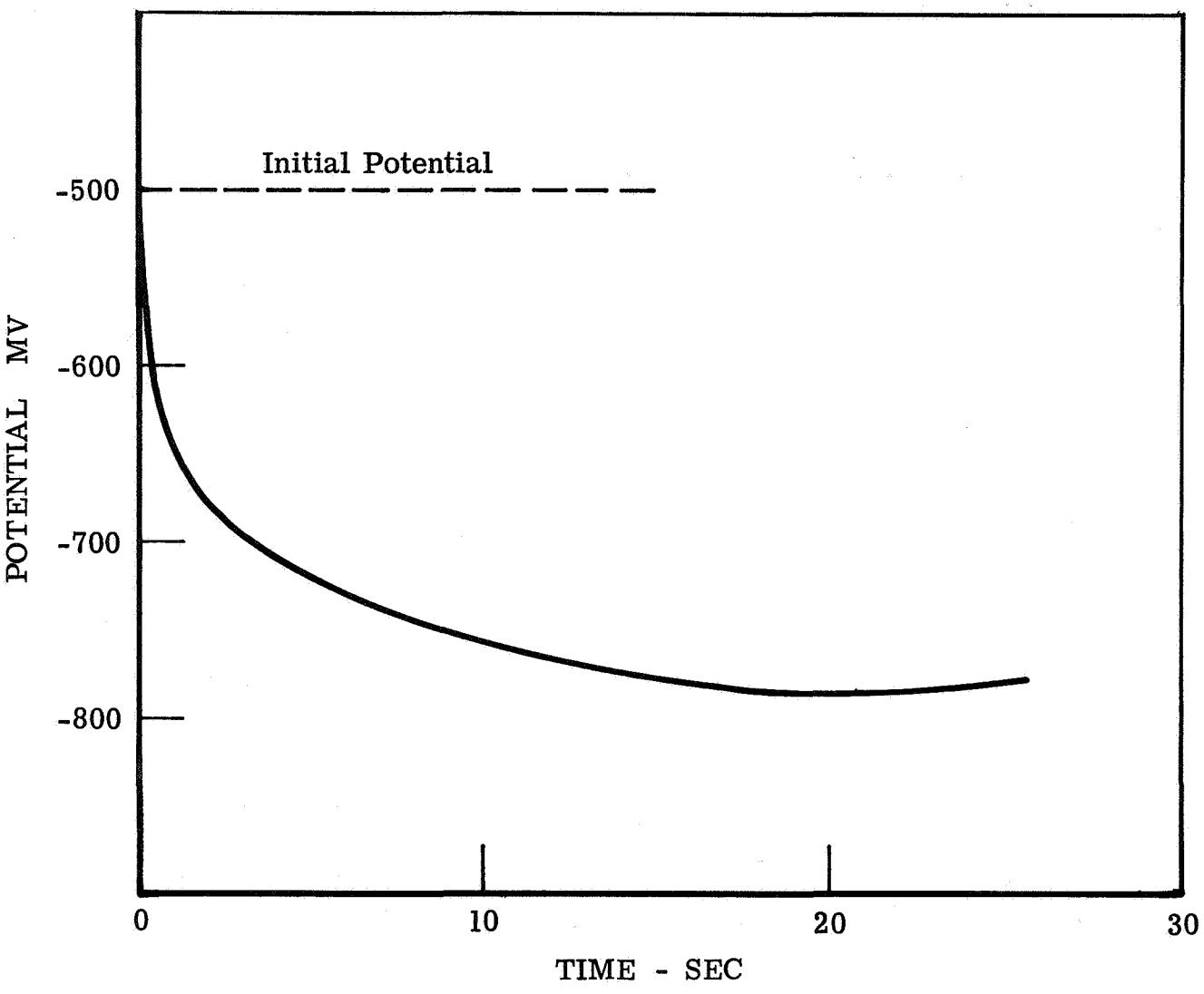

FIG. 4 Change in Potential with Time After Open Circuit from - 500 mv in 0.6 M KI (Sheet 2283)

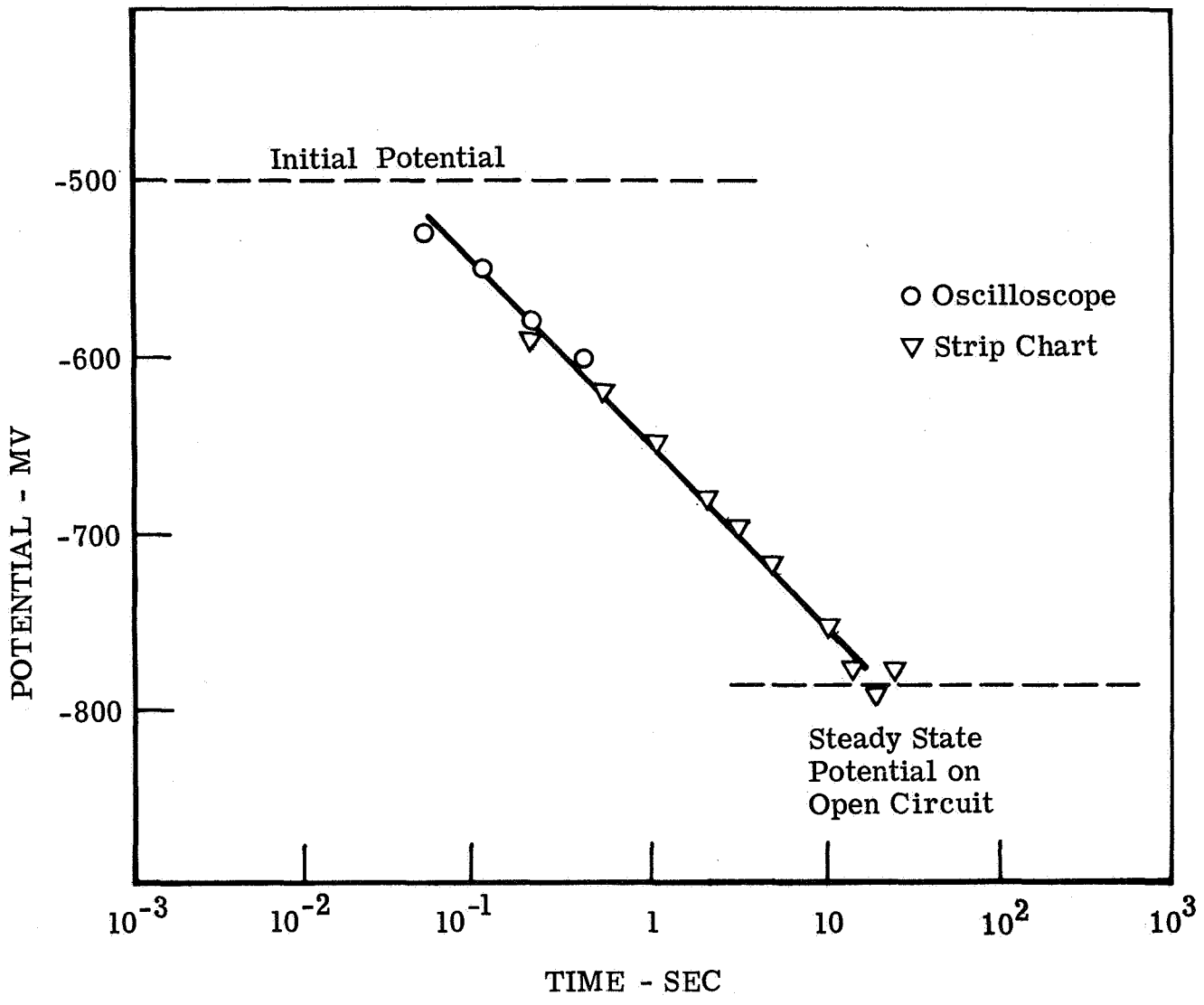

FIG. 5 Change in Potential with Log (Time). After Open Circuit from - 500 mv in 0.6 M KI Sheet 2283)

IR component disappeared in less than 10^{-8} sec in the pitting corrosion experiments previously report (3, 1st Quarterly, Fig. 13).

The time to reach the steady-state open-circuit SCC potential was on the order of 1 to 10 seconds for a number of experiments. The transition time for a diffusional process can be approximated by:

$$T = \frac{\ell^2}{D} \qquad \text{Equation 20}$$

This equation can be used to estimate the diffusion distance ℓ. Assuming a diffusivity of 10^{-5} cm^2/sec gives $\ell = 3 \times 10^{-3}$ to 10^{-2} cm for the above transition times. This diffusion distance is consistent with 1/10 of a 0.12 cm thick specimen considered earlier as the position where current and solution enter the sides of the crack. Unfortunately decay of concentration overpotention and decay of activation overpotential both have the same type of relation to log time (see, for example 7), so further analysis will be necessary to definitively state that the experimentally observed potentials are concentration overpotential. However, the low activation energy for SCC velocity indicates a mass transport limiting process rather than a kinetic process (1).

(b) Open Circuit SCC Potential

During the potential decay experiments it was observed that the potential always decayed to about -800 mv. Fig. 6 shows the initial current and the open-circuit potential asymptote for a series of experiments conducted in 0.6M KCl solution with initial potentials in the range of -900 mv to 0 mv. The current was linear with potential as observed earlier (1, Fig. 22), with an intercept near -800 mv. A cathodic current and an applied potential more negative than -900 mv was required to stop crack propagation. The open-circuit asymptote was near -800 mv regardless of whether the initial potential was positive or negative in respect to this value. The open-circuit potential for SCC crack propagation was nearly the same in chloride, bromide and iodide solution, however, its value changed with SCC velocity.

The steady-state potential of about -800 mv during open circuit crack propagation is consistent with a mixed potential for titanium oxidation and hydrogen ion reduction in 0.1 to 1 normal acid (3, 3rd Quarterly, Fig. 10). If the mixed potential existed throughout the length of the crack there would be no current and potential gradient down the crack and no net hydrogen ion reduction. Further, the net anodic current of halide ions to the crack tip would have to be balanced by a reduction of hydrogen ions, which would cause the solution

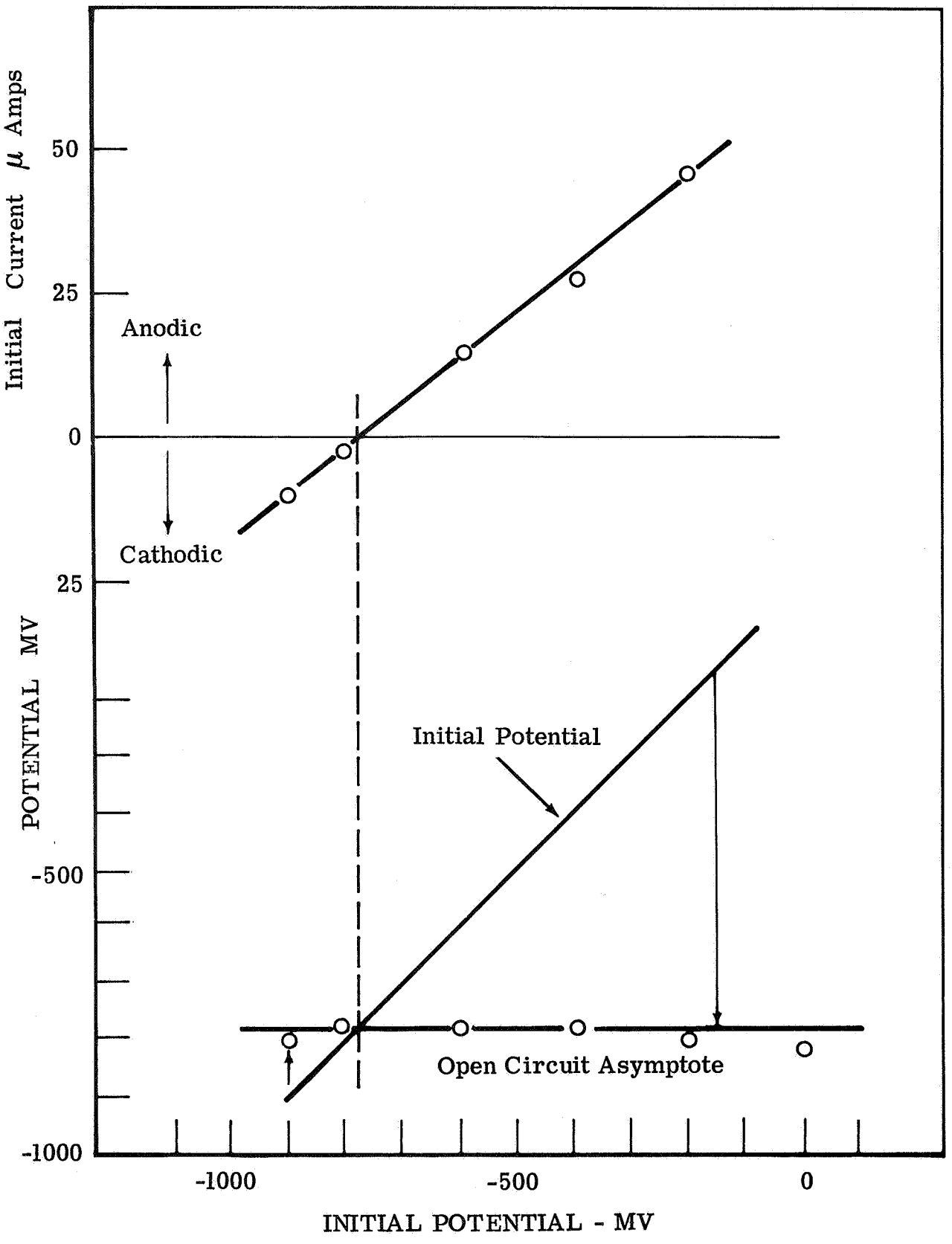

FIG. 6 Initial Current and Open Circuit Potential Asymptote during SCC Propagation in 0.6 M KCl (Sheet 2283)

to go alkaline. An alkaline solution would be inconsistent with a mixed potential of -800 mv for oxide formation and hydrogen ion reduction on open circuit SCC propagation.

Two possible solutions to this dilemma are: the mixed potential is due to titanium halide formation and hydrogen ion reduction; or hydrolysis of the initially formed titanium halide occurs with the generation of hydrogen ion which is reduced at another position in the crack. The first mechanism does not appear to be reasonable because it would require the formation of halide in preference to oxide in alkaline solution. At -800 mv in alkaline solution there would be a large driving force to form oxide and it is highly unlikely that multi-layers of halide would form in preference to oxide which forms rapidly on newly exposed metal. The potential observed during open circuit SCC propagation is one bit of evidence pointing to hydrolysis of titanium halide occurring in the crack. A simplified model for the hydrolysis mechanism and other evidence will be introduced in section 3.1.4.

(c) Extended Range of Potential

The mass-transport-kinetic model does not contain an explicit relation of velocity to applied potential. The potential applied at the mouth of the crack can only influence velocity in the model through its effect on concentration near the crack tip.

Thus, applied potentials more positive or anodic to the open circuit potential increase oxidation relative to hydrogen ion reduction, resulting in a net generation of hydrogen ions. The potential gradient is also in the direction to bring halide toward the crack tip by migration so that the concentration is greater than for pure diffusion and the gradient is steeper near the tip as shown in Fig. 3. At applied potentials more negative than the open circuit mixed potential there would be a net reduction of hydrogen ions and migration of halide ion would be reversed, resulting in a reduced halide ion concentration in the crack and a smaller gradient near the tip. At a sufficiently negative potential, the halide concentration would be reduced to a low level compared to hydroxyl ion concentration and the crack would stop (1). The experimental data already presented are qualitatively in agreement with this model. Quantitatively, however, as will be described later, it appears necessary to also introduce titanium halide hydrolysis into the model to explain the wide range of velocity with potential.

If the velocity is determined by halide concentration near the crack tip there must be an upper limit to the concentration and the velocity in respect to potential. Prior experiments, at potentials below +1000mv, had indicated no such limit

to the velocity. It was decided to extend the range of applied potentials to determine if there is an upper limit. Results are shown in Fig. 7 for 0.6 M chloride and iodide solutions. The experiments were conducted with epoxy coated specimens in order to minimize surface reactions. (Mill annealed specimens of sheet 2208, with chemical analysis shown in Table VI, were used.) A limiting velocity was observed that occurred at about +1000 mv in chloride and iodide. The decrease in velocity at potentials higher than +1000 mv in iodide may have been due to removal of iodide by oxidation to iodine as it was observed that the solution turned brown near the crack. At potentials lower than +1000 mv the velocities were somewhat higher for this mill annealed sheet at about 1/3 the fracture load than for duplex annealed sheet previously reported (1, Fig. 21). This is consistent with the heat treatment effect previously report (3, 3rd Quarterly)

The strength in chloride and iodide solutions appeared to be equivalent at potentials more negative than -500 mv. The strength in iodide solution was independent of potentials more positive than -500 mv. The strength in chloride solution increased at potentials more positive than -500 mv but complete

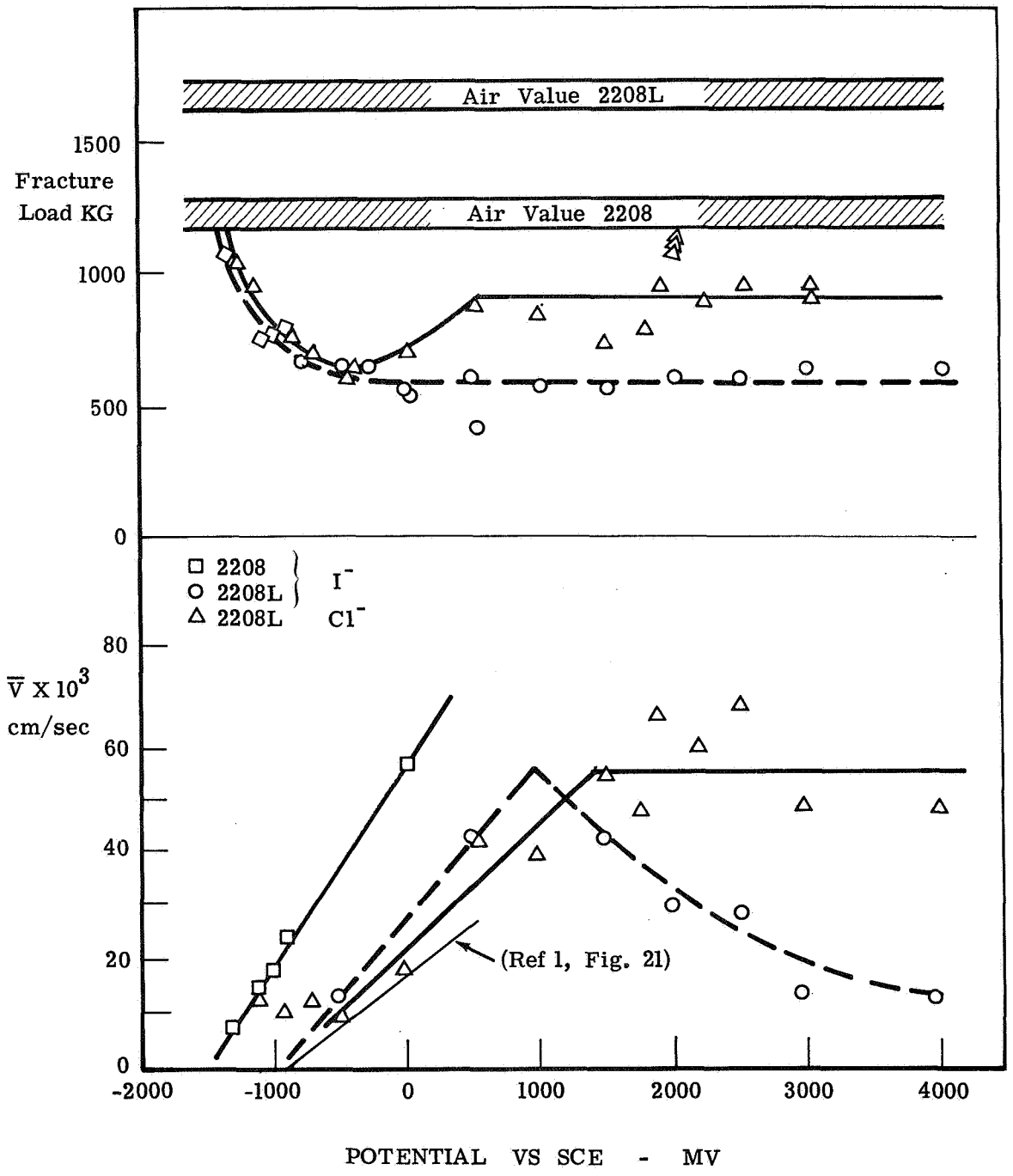

FIG. 7 Strength and Fracture Velocity of Mill Annealed Specimens over an Extended Range of Potentials in 0.6 M Chloride and Iodide Solutions

anodic protection did not occur with this mill-annealed sheet. A plateau in strength about 50% above the minimum at -500 mv but considerably below the air value was observed. There appeared to be some perterbations in strength from the plateau level at +1000 to +2000 mv but not enough experiments were made to determine if this is a real effect. Pitting corrosion was observed to start on the new fracture faces at +2000 mv.

An interesting effect was observed in respect to rolling direction on sheet 2208. Most of the specimens from this sheet were cut transverse to the rolling direction so that the crack propagated longitudinal to the rolling direction (designated 2208L). The cracks propagated in a direction at an angle to the usual course, normal to the tensile direction. Specimens cut in the longitudinal direction, with crack transverse to the rolling direction, appeared to be more notch sensitive as indicated by the lower fracture load in air, and the crack propagated at a higher velocity and in this case, normal to the tensile direction. The direction of crack propagation is opposite to the observations on duplex annealed sheets 2433 and 2533 (3, 3rd Quarterly).

3.1.4 Simple Hydrolysis Model

In this section a simple mass transport model including hydrolysis of titanium halide is described. Some striking similarities are observed between this model and the previously described model for pitting corrosion (3, 1st Quarterly) as well as between the data for the two processes.

It is instructive to first calculate velocity for the limiting case of a mass-transport-controlled velocity with no hydrolysis or wall reactions. This case is represented by the dashed line in the concentration plot in Fig. 3. It can be readily shown that for a small, constant-angle crack in a unit thickness specimen and for constant diffusivity the equation for this condition is:

$$C_-^o = \frac{I_-}{z_- D_- \gamma} \ell n \left(\ell / \delta^p \right) \qquad \text{Equation 21}$$

The tip current can be related to velocity by equation 19:

$$I_- = 2n\, Q_x V$$

Eliminating I_- gives:

$$V = \frac{z_- F D_- \gamma C_-^o}{2n\, Q_x \ell n \left(\ell / \delta^p \right)} \qquad \text{Equation 22}$$

Equation 22 is plotted in Figure 8 and compared to a collection of experimental velocity versus concentration data. The constants used in Equation 22 are given in Table V. The data were taken on three different sheets, at three potentials and with NaCl and HCl electrolytes. Both initial and average velocities are included as sometimes one was more convenient than the other to measure. The data

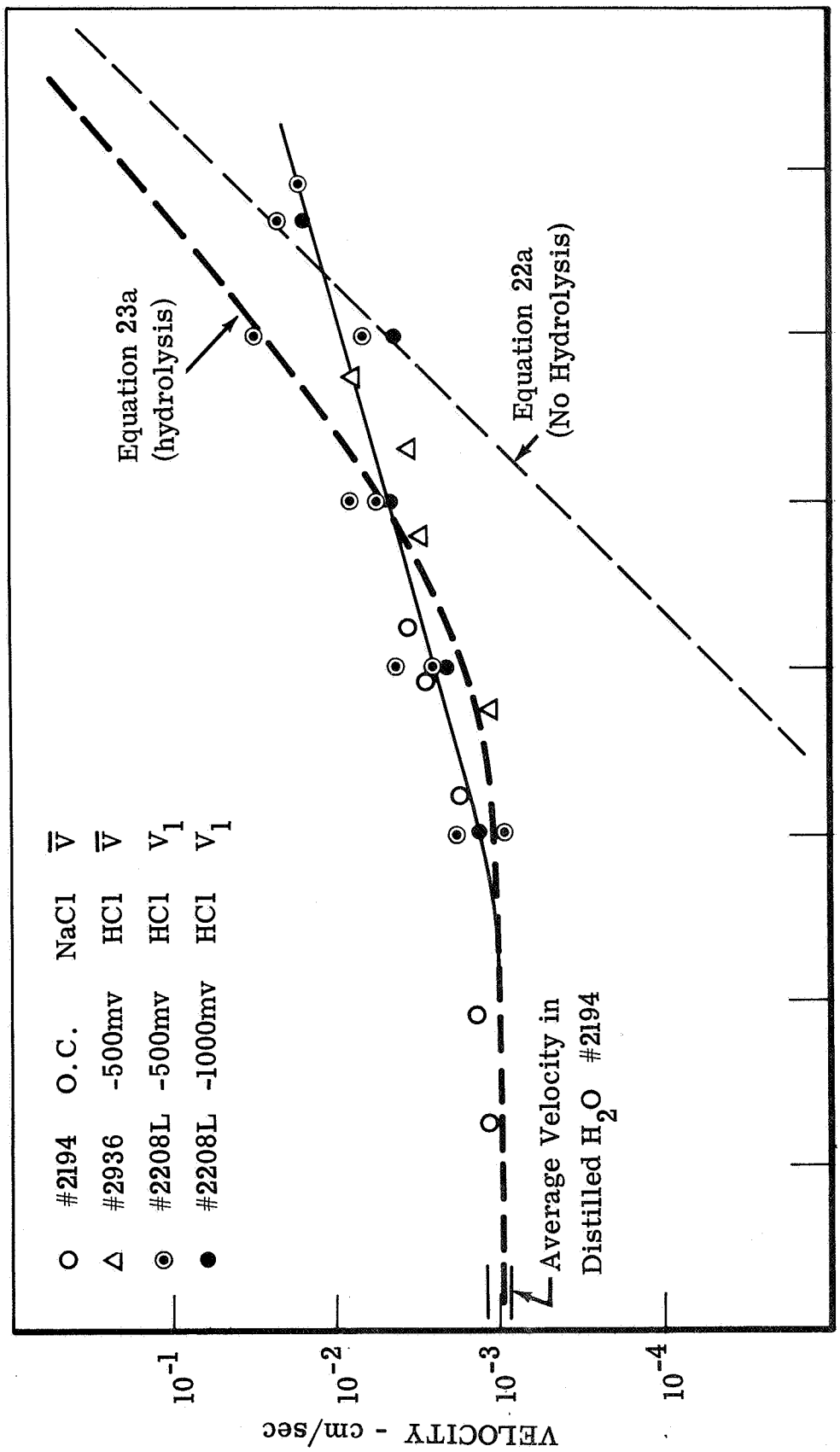

FIG. 8 Correlation of Crack Propagation Velocity with Halide Ion Concentration

Table V

Constants used in Equations 22 and 23 for Plots in Fig. 8

$z_- = 1$ equiv/mole

$F = 96500$ coul/equiv

$D_- = 1 \times 10^{-5}$ cm^2/sec

$\gamma = 0.05$

$n = 1$

$Q_x = 425 \times 10^{-6}$ coul/cm^2

$\ell = 10^{-1}$ cm

$\delta^p = 10^{-6}$ cm

$V^s = 10^{-3}$ cm/sec

$V = 5.0\ C_-^\circ$ cm/sec Equation 22a

where C_-° is in mole/cm^3

$C_-^\circ = 1.18 \times 10^{-2}\ V\ \ell n\ (V \times 10^3)$ Equation 23a

are somewhat scattered as expected but nevertheless show significant trends. The velocity is not linearly related to concentration as predicted from Equation 22, but varies approximately as the 0.27 power over about four decades of concentration. At low concentration, the velocity does not approach zero, but becomes asymptotic to the velocity observed in distilled water.

If it is accepted that a halide mechanism occurs at the crack tip to cause crack propagation, it is mandatory that the halide ion is conserved within the crack in distilled water because there is no significant source. In other words, hydrolysis of titanium halide or displacement of adsorbed halide ions must occur.

Chloride ion can be gathered from the content in the metal as new metal surface is exposed, but this amount is insufficient to cause cracking unless it is allowed to accumulate in the electrolyte in the tip zone. For example, to accumulate a monolayer on both walls of the tip zone of 10^{-6} cm length would require exposing about 10^{-1} cm length of new surface if there were ten parts per million atomic of chloride in the metal and chloride were removed only from the surface layer (Appendix B).

Inclusion of titanium halide hydrolysis in the rigorous mass-transport-kinetic model entailed considerable additional complexity and required hydrolysis rate constants with unknown value. It was therefore decided to test the hydrolysis concept in a much simplified model before altering the more rigorous model. The derivation for the simple hydrolysis model is given in Appendix C, but the basic assumptions and solution are outlined here.

The hydrolysis model is illustrated in Fig. 9. The following assumptions were made:

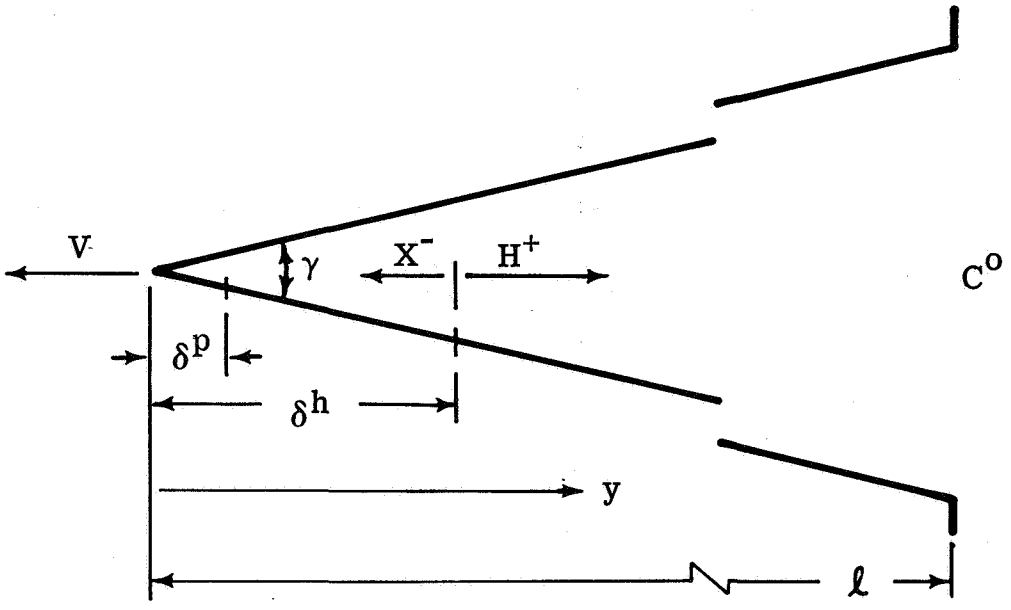

(Hydrolysis Occurs and Goes to Completion at δ^h)

FIG. 9 Hydrolysis Model

1. A small, constant-angle crack propagates at a velocity V through a unit-thickness specimen.
2. The environment is a hydrogen halide solution, i.e., only H^+ and X^- ions are present and their diffusivities are constant.
3. The reaction at the tip is: $Ti + 2X^- \rightarrow TiX_2 + 2e$ with a current $I = 2n\, Q_x V$.
4. The TiX_2 remains adsorbed on the surface to the position, δ^h, where hydrolysis occurs and goes to completion:

$$TiX_2 + 2H_2O \rightarrow TiO_2 + 2X^- + 4H^+ + 2e$$

5. No further oxidation of titanium or hydrogen ion reduction occur in the crack. Therefore, from δ^h to δ^p there is a constant current of halide ions, $I_- = 2n\, Q_x V$ and from δ^h to ℓ there is a constant current of hydrogen ions, $I_H = 4n\, Q_x V$. This last assumption is probably the weakest link but it is justified on the basis that it makes a simple analysis possible (continued oxidation with formation of multilayers of oxide generates considerable more H^+.)
6. A constant time for hydrolysis is assumed such that

$$\delta^h = \delta^{hs}\, \frac{V}{V^s}$$

where the superscript s refers to the condition in pure water where the bulk concentration $C^o = 0$. Using these assumptions and solving the mass-transport equation gives:

$$C_-^{\,o} = \frac{2n\left(1 + \frac{D_H}{2D_-}\right) Q_x}{F\, \gamma\, D_H}\, V\, \ell n\, \frac{V}{V^s} \qquad \text{Equation 23}$$

It turned out that this relationship of velocity to concentration is independent of the values of δ^p and ℓ chosen.

Equation 23 is plotted in Fig. 8 using the constants shown in Table V. Equation 23 appears to have the right form as compared to the experimental data but it gives velocities too high in concentrated solutions. The fit is close enough, however, to warrant adding the hydrolysis step to the more rigorous mass-transport-kinetic model. This work is in progress and will be reported at a later date.

Non-dimensionalized concentration gradients for the simple hydrolysis model and the mass-transport-kinetic model (from Fig. 3) are compared in Fig. 10. The calculations were based on a 0.6 molar bulk solution in each case. The oxidation of titanium to TiO_2 near δ^p is seen to contribute significantly to the slope near δ^p so that the simplifying assumptions of no reaction in the zone from δ^p to δ^h in the simple hydrolysis model was not justified. The experimental dependence of velocity on potential is assumed to occur through the effect of potential on the oxidation reaction rate and therefore the concentration.

Non-dimensionalized concentration gradients for the simple hydrolysis model are plotted in Fig. 11 with bulk concentration as a parameter. The lower the bulk concentration, the greater the ratio of the slope from δ^p to δ^h to the Nernst diffusion slope. This is the reason for the increasing ratio of velocities computed from equations 23 and 22 respectively at low concentrations in Fig. 8.

A striking similarity is seen between the concentration profiles in Fig. 11 and the calculated concentration profiles for the pitting corrosion model (3, 1st Quarterly, Fig. 16). Other than the logarithmic distance scale which results from the wedge shape geometry and the angular shape

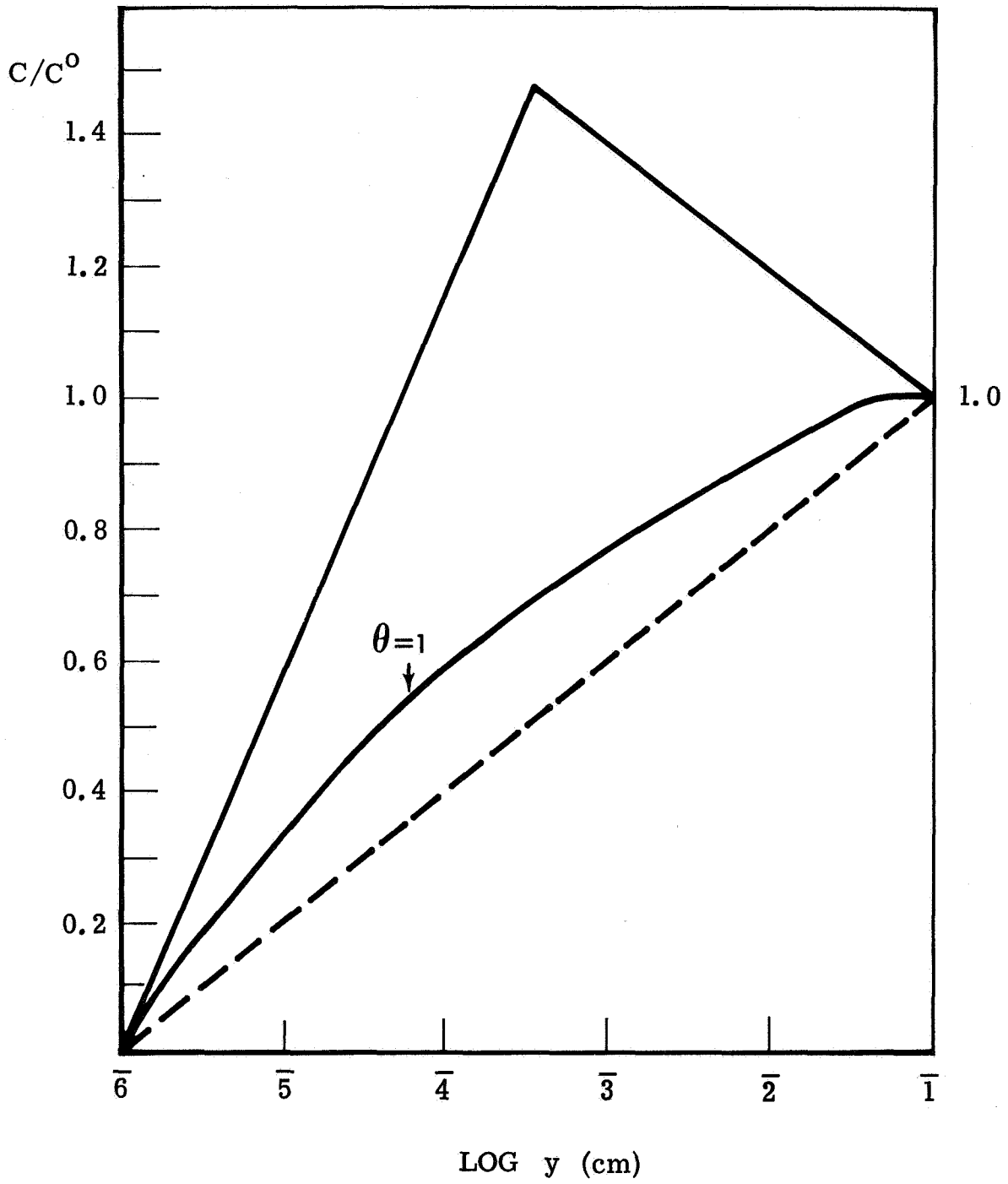

FIG. 10 Comparison of Non-dimensionalized Concentration Gradients in Simple Sydrolysis Model and Mass-Transport-Kinetic Model

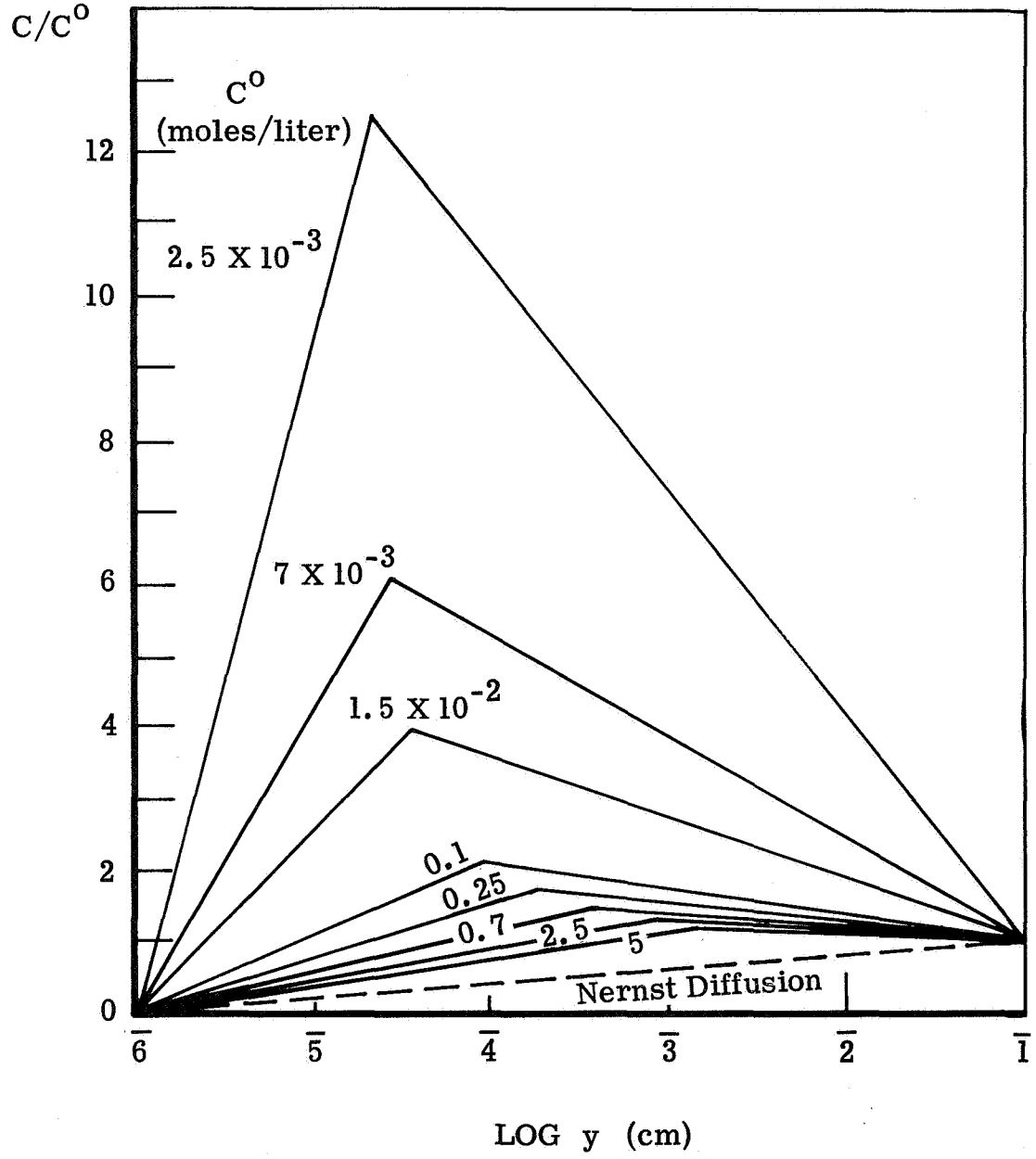

FIG. 11 Effect of Bulk Concentration on Non-dimensionalized Concentration Gradient for Simple Hydrolysis Model

which results from complete hydrolysis at a point rather than distributed reaction, the curves show similar trends. Perhaps it is fortuitous but the experimental SCC velocity varied with the 0.27 power of the concentration (Fig. 8) and the pitting corrosion current density appeared to vary with the 0.27 power of the concentration (3, 1st Quarterly, Fig. 10).

Although there are some similarities between the electrochemistry of SCC and pitting corrosion, there are also some significant differences. One of these is the difference in observed potentials for the two processes as shown in Fig. 12 (redrawn from Fig. 5 and 3, 1st Quarterly, Fig. 13).

In the pitting mechanism the hydrolysis must occur in solution. The lower valent halides are soluble, relatively completely ionized, and not readily hydrolyzed. The tetrahalides are relatively non-ionized and readily hydrolyze to form an insoluble oxide species. Therefore, in order to obtain the hydrolysis necessary to develop high halide concentrations in the boundary layer, the tetrahalides must be formed.

The reversible potentials for various titanium halide reactions are shown in Fig. 13. It is seen that a potential of -760 mv is required to obtain titanium tetrabromide, but higher potentials may be required to obtain some of the intermediates. Therefore, a high overpotential for the tribromide may be required to obtain the hydrolyzable tetrabromide. This may explain the threshold potential and current density for pitting corrosion (3, 1st Quarterly, Fig. 9). The higher threshold potential and current density for the chloride environment (3, 1st Quarterly, Fig. 12) qualitatively is consistent with the higher overpotential required for the corresponding trichloride to tetrachloride step as indicated in Fig. 13.

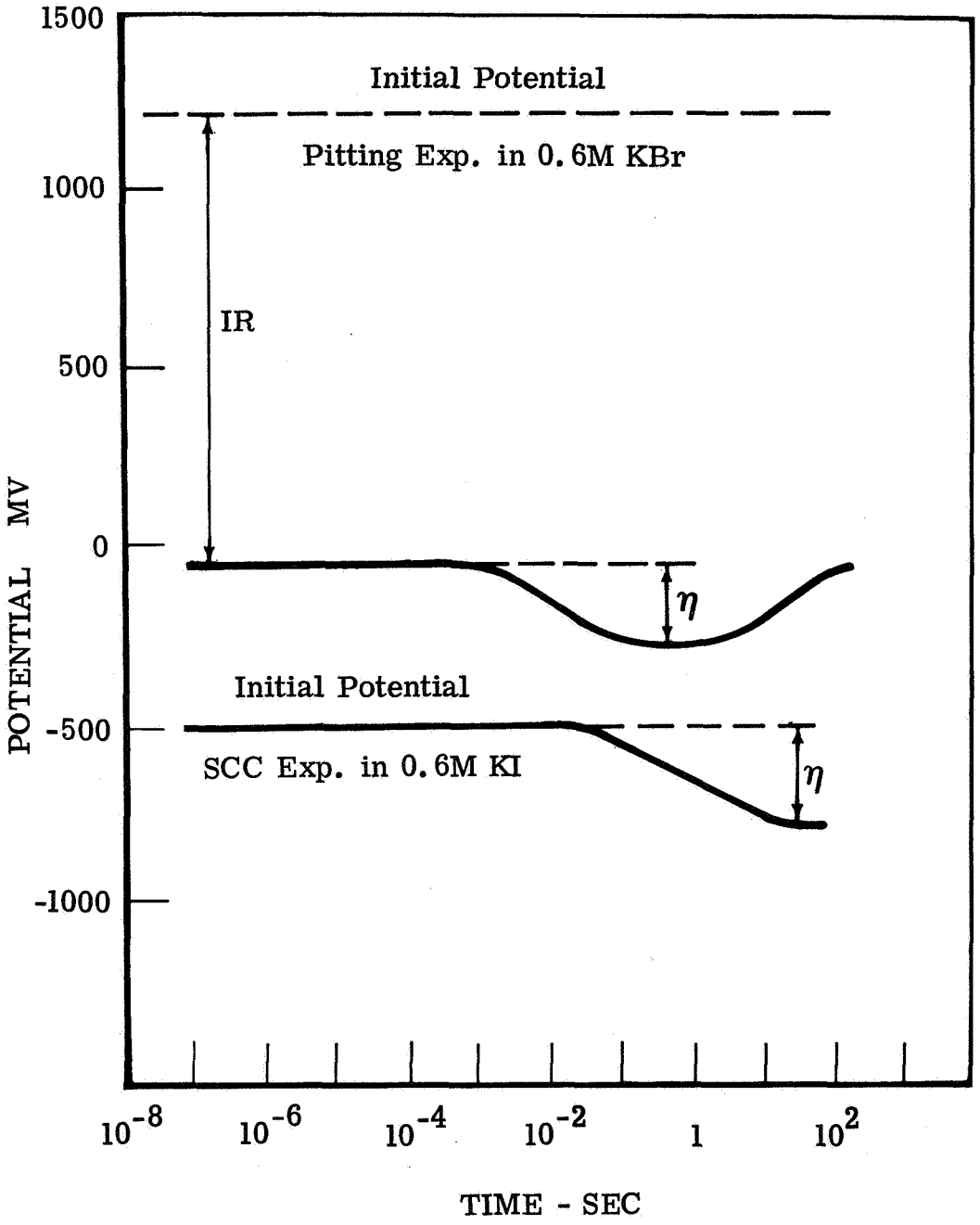

FIG. 12 Comparison of Potential-Decay Data for SCC and Pitting Corrosion

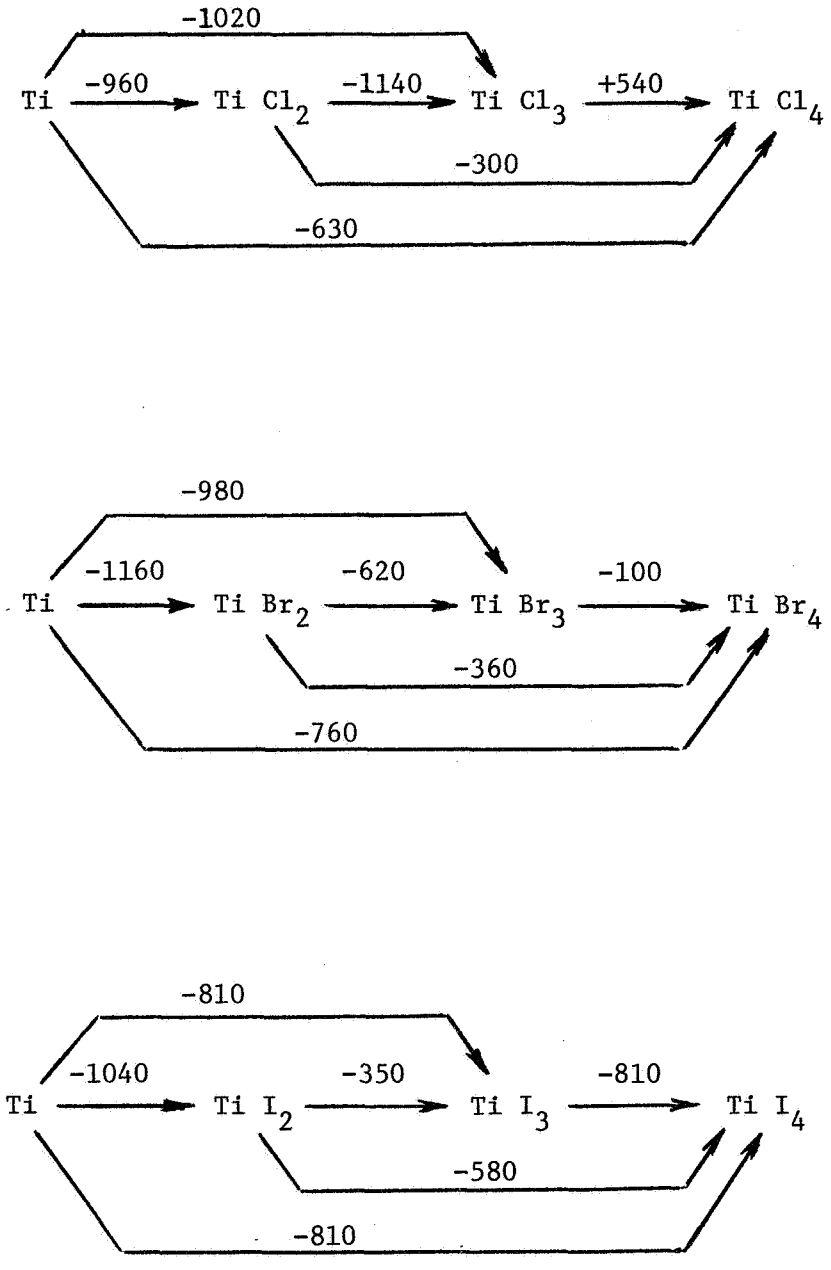

FIG. 13 Reversible Potentials (vs SCE) for Various Titanium Halide Reactions (Based on Latimer)

Further transient studies on the pitting reaction in chloride bromide and iodide solutions will be made to test this hypotheses. Unfortunately, at the time the pitting transient studies were made, the oscilloscope had an intermittent shift in calibration of about 300 mv and it is not known whether the minimum potential (3, 1st Quarterly, Fig. 13) is at -100 mv or -400 mv. (The minimum in Fig. 12 was drawn between these two levels.)

In the SCC mechanism, the hydrolysis must occur on the walls of the crack. The hydrolyzable tetrachloride would not form at an applied potential of less than -630 mv and the tetrabromide at less than -760 mv. If the dihalide or trihalides were to go into solution they would ionize and titanium ions would conduct current from the tip zone. With complete ionization, there would be no flux of halide ions required. The concentration of titanium halide in solution would increase toward the crack tip and the high concentration polorization could not be obtained with the mass-transport-kinetic model.

Further, if hydrolysis of titanium haldies occurred in solution, there should be a considerable difference in velocity with the different halides as observed in pitting corrosion. The SCC velocity, as a function of potential, appears to be relatively independent of whether the environment has chloride, bromide or iodide ions, again pointing to a wall reaction.

It is not certain, however, that a true compound is formed as the halide ion may be absorbed, with the tip current of halide ions being the double-layer charging current. The regeneration of halide ions in solution

would be by a displacement by oxide rather than a hydrolysis in this case. The rate of displacement by oxide could be less sensitive to the particular halide ion than the rate of surface hydrolysis of the dihalide. The mass-transport-kinetic model gives a value of 0.85 for n in Equation 19. The dihalide would give a value of 1 and halide ions adsorbed one-to-one on the surface titanium atoms would give a value of 0.5 for the value of Q_x - 425 μAmp/cm^2 used. A more careful analysis will be required to distinquish between dihalide and absorbed halide.

The large difference in IR drop between pitting corrosion and stress corrosion cracking should be examined. The pitting corrosion threshold current density is about one amp/cm^2 in 0.6M bromide and 20 amp/cm^2 in 0.6M chloride at room temperature. The current density corresponding to the initial potential of 1200 mv in Fig. 12 is 2 amp/cm^2. The actual current density may be considerably larger than this if all of the apparently active surface is not all corroding simultaneously, i.e., there is a dynamic competition between formation of tetrahalide and formation of oxide. During SCC at -500 mv the anodic current is about 20 μamps for a 0.12 cm thick duplex annealed specimen (Fig. 6). Assuming an angle of 0.05 radians, the current density at ℓ = 0.01 cm, where it is assumed that current flows in from the sides of the crack, is:

$$i = \frac{20 \times 0^{-6}}{(0.12)\ (0.05)\ (0.01)} = 0.3 \text{ amp/cm}^2$$

The current flow lines rapidly diverge upon leaving the crack so the average current density contributing to the IR drop is smaller than this

value. A ratio of IR drops considerably greater than 10 would be expected for the two experiments illustrated in Fig. 12. The actual ratio must be more like 100. A 0.013 cm O.D., 0.004 cm. I.D. Luggin capillary tip was used to detect IR drop in the solution adjacent to the side of a specimen near the tip of a propagating crack at -500 mv. The maximum IR drop detected was 15 mv. This is smaller than the estimated error in the oscilloscope transient shown in Fig. 5.

3.2 Metallurgical and Mechanical Effects

3.2.1 Experimental

(a) Alloys

Tests were performed on several 0.060" sheets and on 0.5" plate of Ti:8-1-1. A series of titanium aluminum alloys was also tested, the compositions of which are listed in Table VI.

(b) Specimens

The notched tensile specimens produced from the 0.060" Ti:8-1-1 and the Ti-Al alloys have been described (1, 3). A small number of notched precracked specimens of the 0.500" Ti:8-1-1 plate were tested in four point bending. The specimen configuration and dimensions for the bend test are described elsewhere (8).

(c) Testing

The general testing procedure has been described previously (1, 3). Most specimens were loaded using a slow crosshead speed (0.005 cms/min.) until the first indication of cracking, which was usually the development of an anodic current. After initiation, three methods of loading were employed; the crosshead motion was continued, stopped or reversed. In order to investigate the influence of higher initial loads, specimens were cathodically protected and on attainment of the required load, the potential was switched to the test potential. From such tests values of

TABLE VI

Alloy Compositions (by weight)

(a) Ti:Al

Designation	Al	O	N	H	C
Ti:6wt%Al	6.11	0.110	0.013	0.004	0.016
Ti:8wt%Al	8.04	0.105	0.012	0.004	0.020
Ti:8.65wt%Al	8.62	0.100	0.006	0.0015	0.013
Ti:10wt%Al	10.28	0.100	0.018	0.006	0.018

(b) Ti:8-1-1

Designation	Al	Mo	V	O	N	H	C
0.060" Sht# 2283	7.8	1.04	1.0	0.075	0.0012	0.003	0.040
2194	7.6	1.05	0.98	0.109	0.008	0.004	0.040
2208	7.8	1.0	1.0	0.090	0.015	0.003	0.023
2279	7.7	1.1	1.1	0.090	0.009	0.004	0.025
0.500" plate	7.8	1.0	1.0	0.080	0.010	0.009	0.010

the initiation load (which can be converted to net area stress or stress intensity factor) and velocity of cracking were obtained. Also the stress intensity during a test can be computed from the record of the crack length and load. The variation of susceptibility to SCC with potential has been described (1, 3), the majority of the results presented here were conducted in 0.6M KCl at a potential of -500mV or in 0.6M KI at various potentials.

(d) Crack Propagation Velocity

Velocity was measured by the observation of the movement of a crack past lines on the specimen surface. A typical distance-time plot for a static crosshead test is shown in Figure 14 from which it is seen that three velocities can be defined, V_1, V_2, and $\bar{V}$.

(e) Analysis of Data

The load - crack length data from these tests were analyzed using linear elastic mechanics; calculation of the stress intensity factor, K, was performed using the equations given by Srawley and Brown (9). However, it was found that the conditions for plane strain fracture were usually violated during crack propagation in tests on the 0.060" sheet. Thus some of the SCC crack propagation occurs under mixed plane strain and plane stress conditions. Direct comparison of fracture and velocity data for different conditions is complicated by this change in fracture mode.

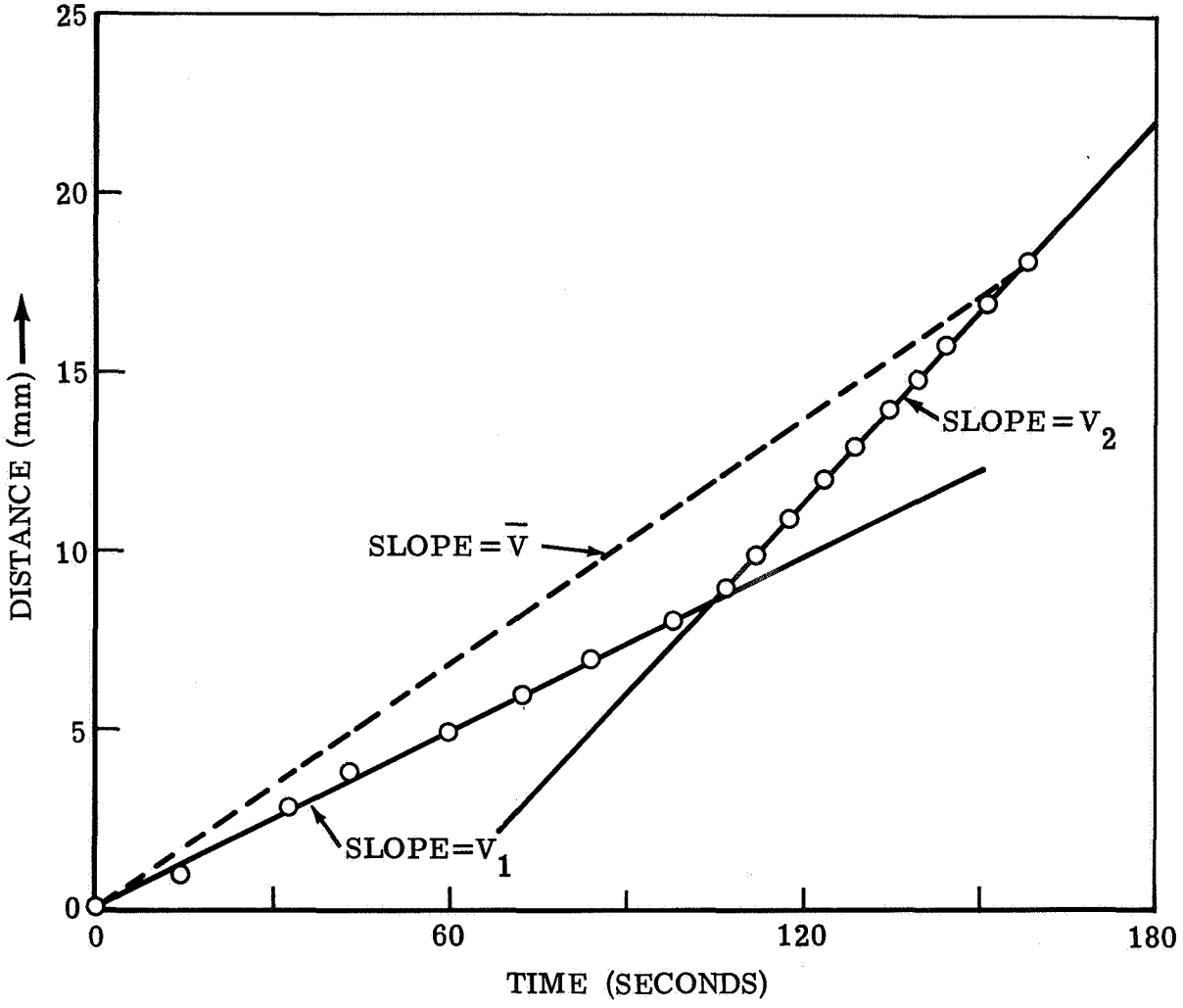

FIG. 14 Typical distance: time record showing definition of V_1, V_2, and $\bar{V}$

(f) Heat Treatment

Heat treatments were performed in argon atmosphere or vacuum furnaces; where necessary, specimens were water quenched. In order to produce a dispersion of the α_2-phase in the α-phase some specimens were step cooled from 800°C. Other specimens were isothermally aged at 600 & 500° C.

(g) Reproducibility of Data

One of the most puzzling features of this work has been the irreproducibility of data from sheet to sheet (there are of course minor inconsistencies in the results from one sheet). Some of the variability can be traced to differences in heat treatment, grain size, distribution of phases and preferred orientation but it appears that other more nebulous factors are present. We can only suggest that some processing factor or impurity elements contribute in some way.

3.2.2 Results

(a) Phase Structure

The phase structure of the Ti-Al alloys (10), Ti:8-1-1 (11, 12) and other commercial alloys (13), have been described in a series of papers. We shall show below that only the hexagonal α-phases in these alloys are considered susceptible to SCC and thus the other phases, e.g., β-phase and α' martensite will not be discussed here. The martensitic transformation β→α'' - martensite, which has a

hexagonal structure, is probably more relevant and it will be shown that there are differences in susceptibility for this phase in the Ti-Al alloys and in the commercial alloys. However, the morphology of the phase and its internal structure are similar in the Ti:8Al and Ti:8-1-1 alloys. In both Ti:8Al and Ti:8-1-1, low temperature aging produces a dispersion of the $\alpha_2(Ti_3Al)$ phase in the α-phase. The morphology and distribution of the α_2-phase in the α-phase in step-cooled specimen is shown in Figure 15. One other aspect of transformation behavior relevant to SCC susceptibility in these alloys is the formation of the ω-phase in the β-phase on low temperature aging. It has been shown that the hexagonal ω-phase is formed in the β-phase of Ti:8-1-1 on low temperature (260°C)aging (13). A subsequent section will show that the presence of this phase makes the alloy more susceptible.

(b) Mechanical Properties and Dislocation Arrangements

Aluminum additions to titanium increases the modulus and yield strength and decreases ductility (14, 15). The yield stress - composition curve tends to be concave upwards and Figure 16 shows such a relationship. However, interstitial solute elements probably have the predominant effect on yield stress and it appears that the effect of aluminum is additive to the interstitial content in determining the absolute strength of an alloy. Thus, the yield stress -

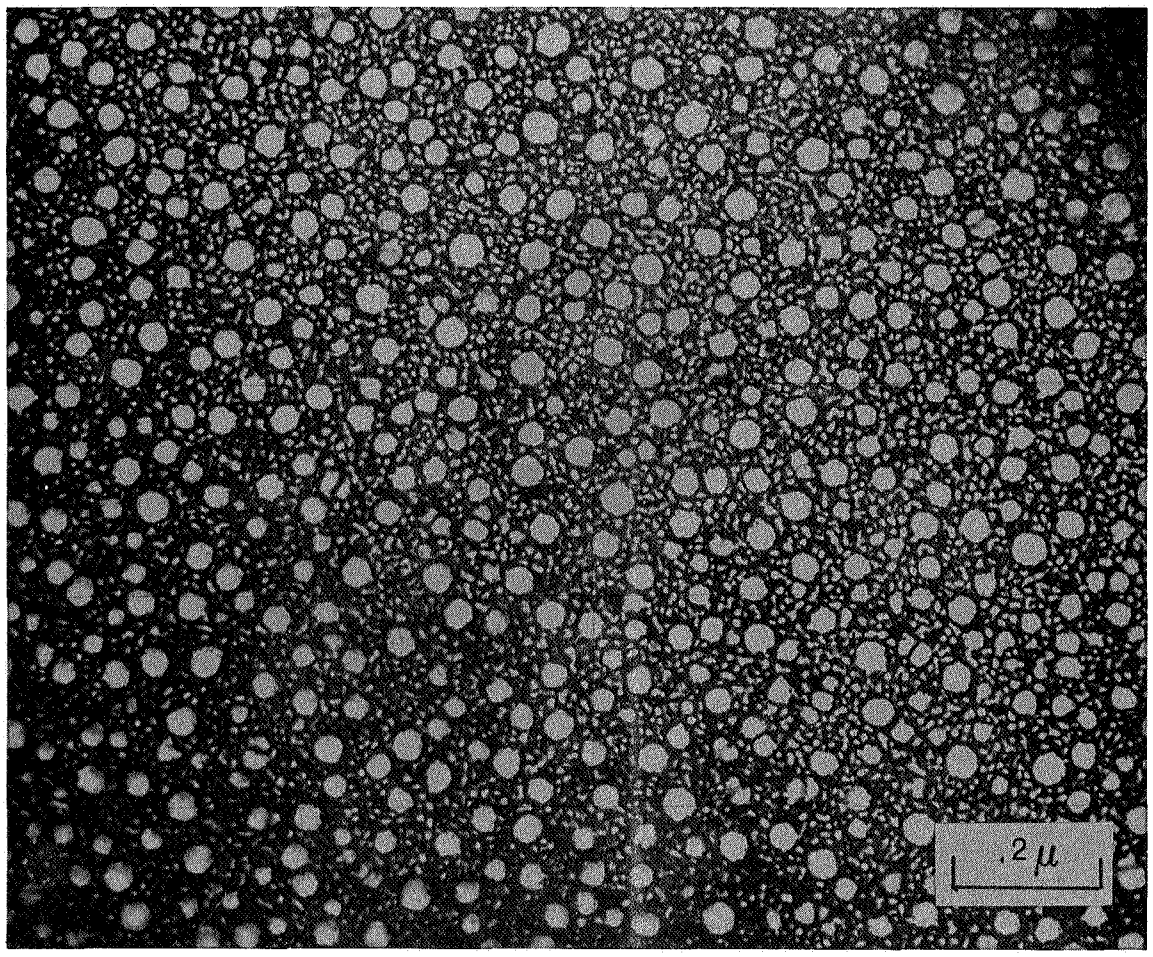

FIG. 15 α_2 particles in step cooled Ti:8.65 wt% Al, showing two particle sizes.
Dark field, $\bar{g} = (11\bar{2}0)\alpha_2$, [0001]α Zone Normal

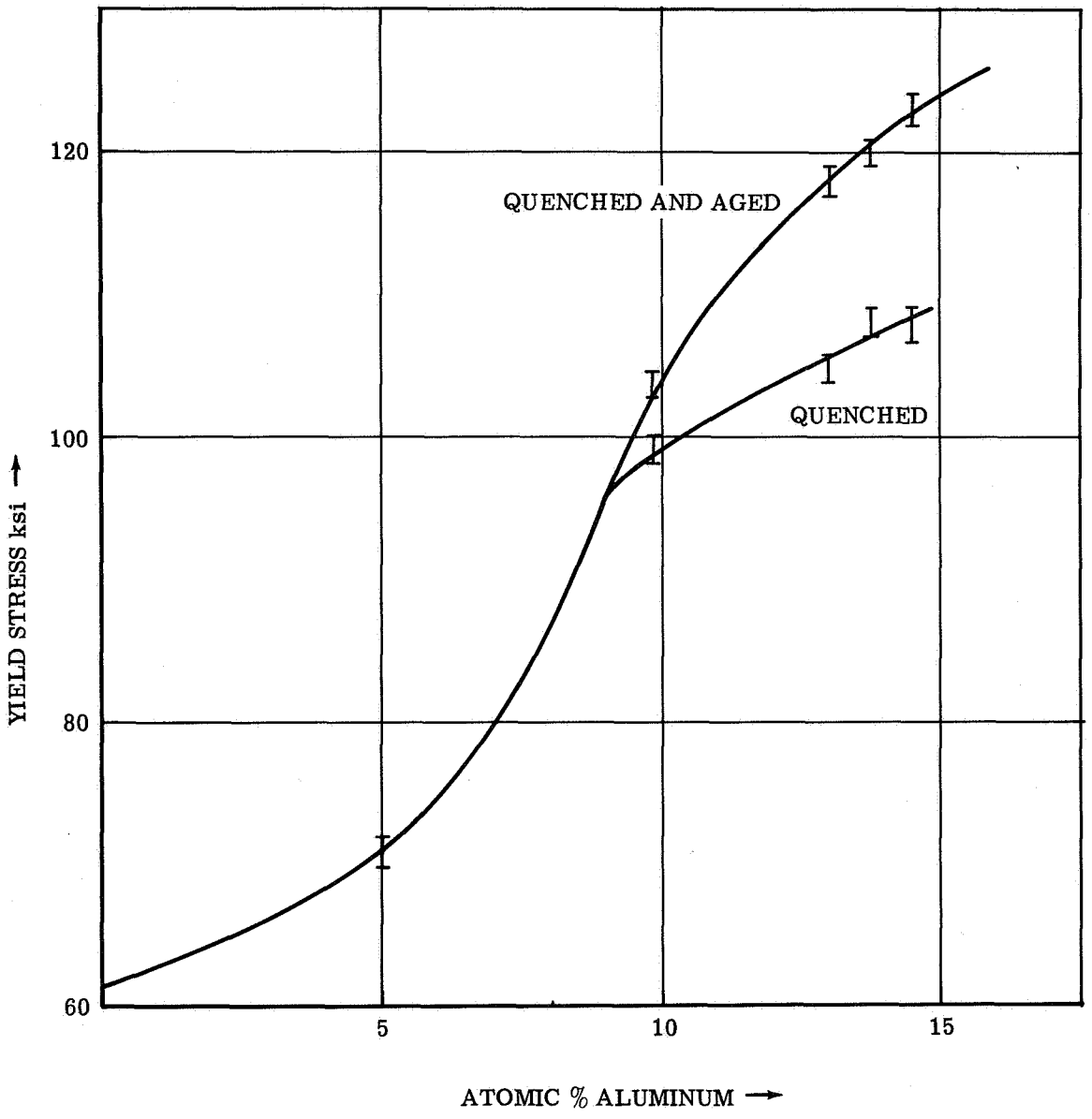

FIG. 16 Variation of yield stress with aluminum content

composition curve is always concave upwards but the position of this curve on the stress axis is largely determined by interstitial content.

Yield strengths of the Ti:8.65 wt% Al alloy have been determined as a function of heat treatment and these results are plotted in Figure 17. Although at present insufficient data is available to determine the grain size dependence of the mechanical properties in this alloy, several coarse grained specimens have been tested. In all cases, these specimens fractured by cleavage without macroscopic yielding.

Dislocation arrangements have been studied in deformed impure Ti, Ti-Al alloys and Ti:8-1-1 and the more important observations are summarized below:

(i) The dislocation arrangements vary from cellular arrays in unalloyed, low oxygen titanium to coplanar arrays in the Ti:8.65 wt % Al alloy as shown in Figures 18 (a) and (b). The transition from cellular to coplanar arrays occurs at an aluminum content of $\sim$5 wt % Al.

(ii) Evidence for $\{11\bar{2}2\}$ slip has been found in alloys containing 0, 4, 5, 6 and 8 wt % Al, but the extent of such slip appears to decrease with increasing concentration. The Burger's vector for this type of slip has not been determined, but it has been shown that it is not $<10\bar{1}0>$. Examples of such dislocations are shown in Figure 19.

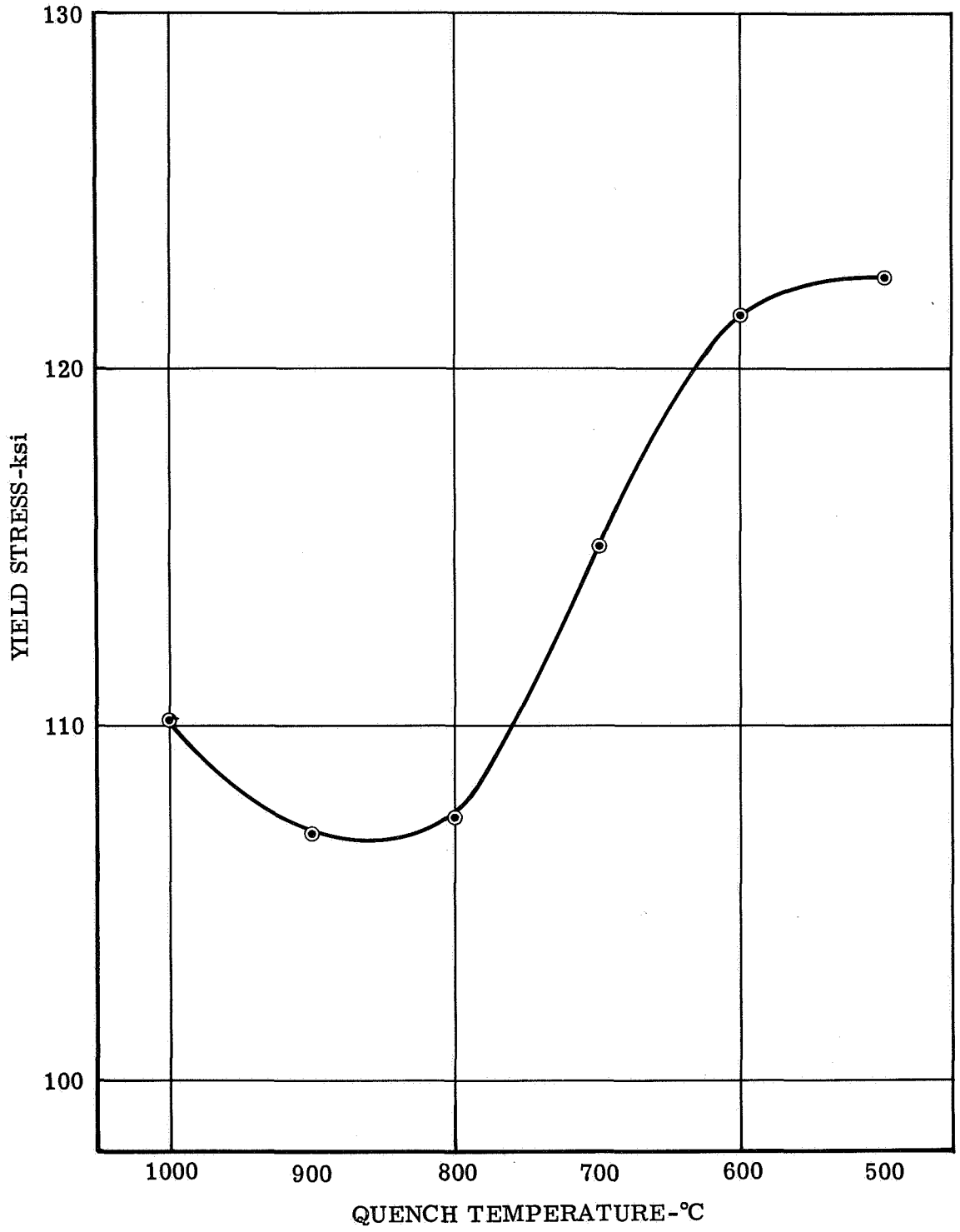

FIG. 17 Yield stress vs. quench temperature for Ti:8.65 wt% Al

FIG. 18 Dislocation arrangements after ~3% deformation

(a) Extensive tangling in commercially pure titanium (1500 ppm oxygen)

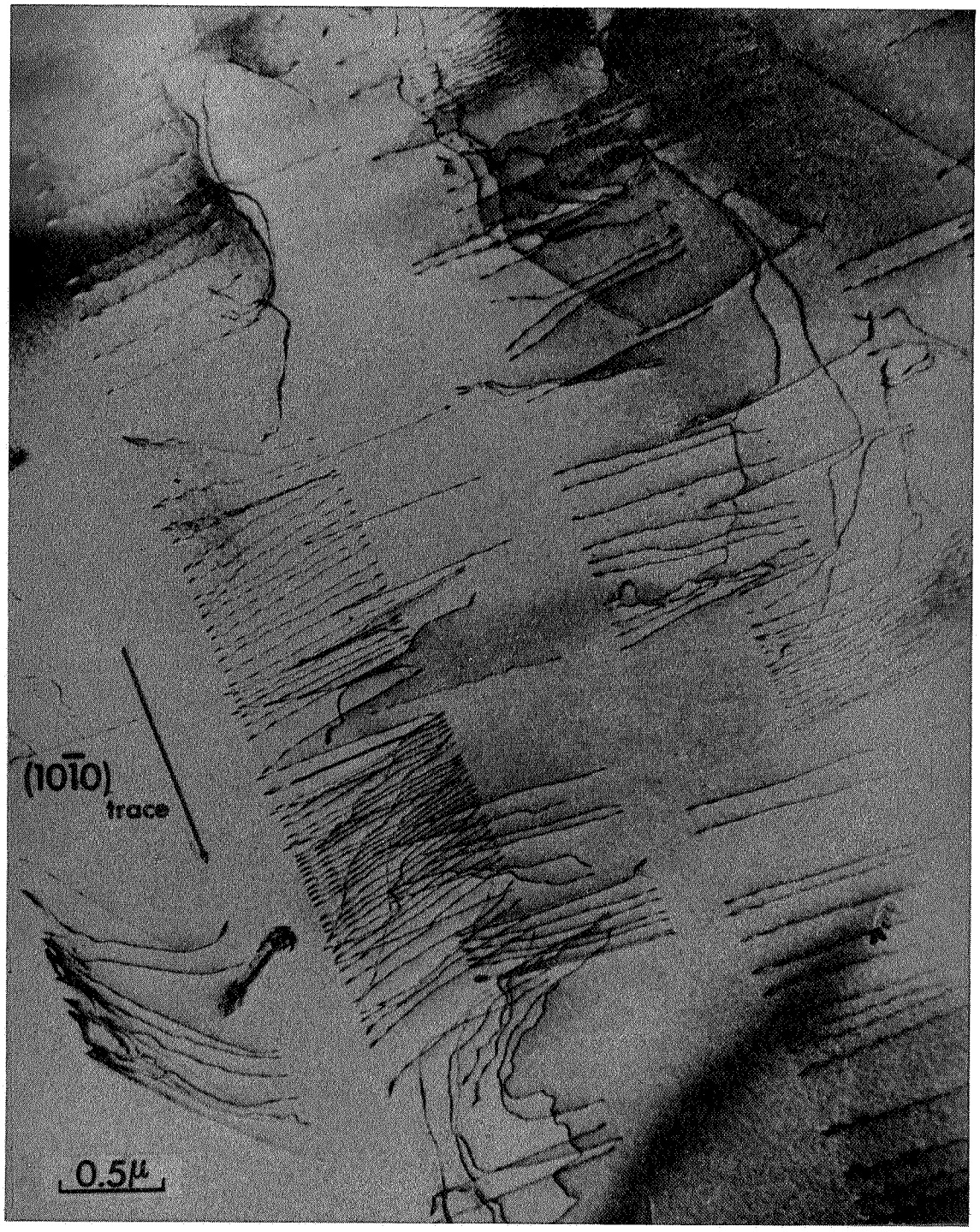

FIG. 18 Dislocation arrangements after ~3% deformation
(b) Coplanar arrays in quenched Ti:8.65 wt% Al

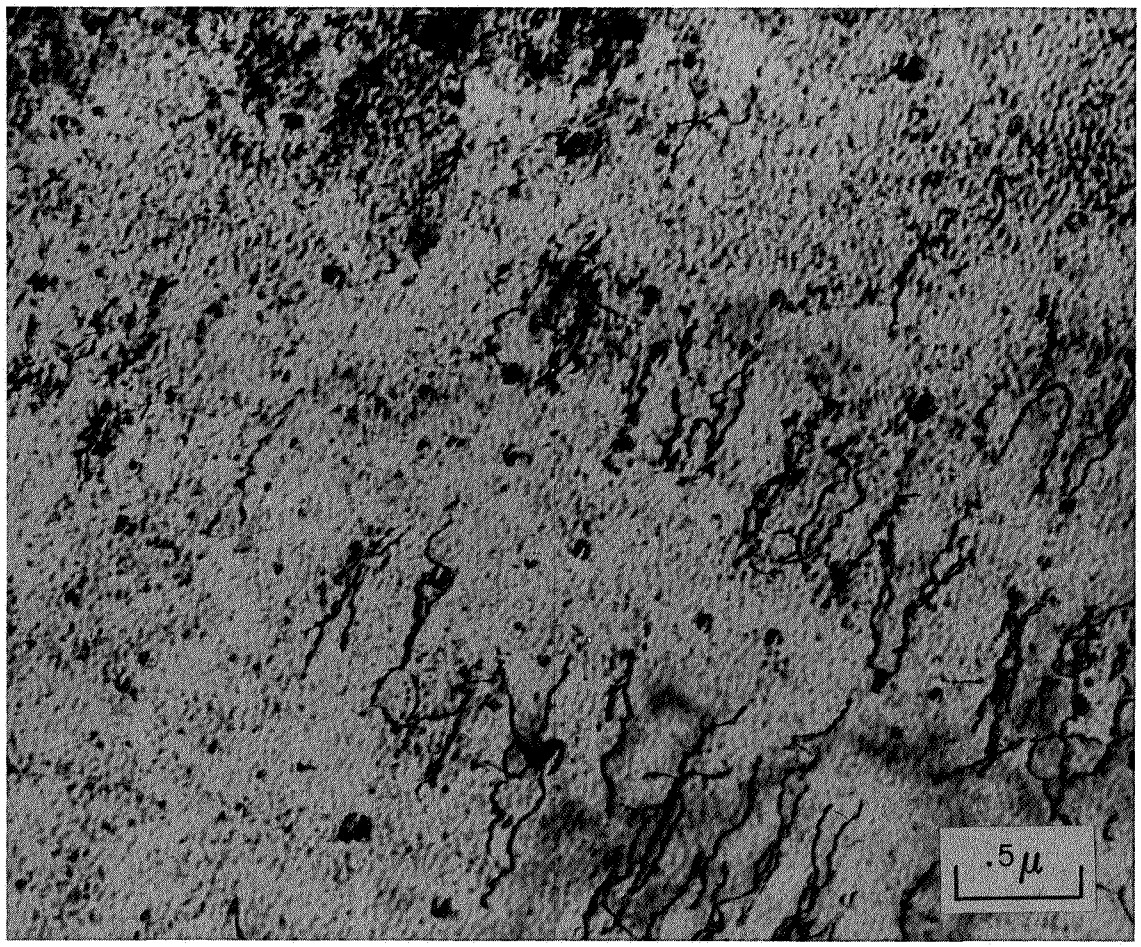

FIG. 19 $\{11\bar{2}2\}$ slip in commercially pure titanium (1500 ppm oxygen). $[11\bar{2}0]_\alpha$ Zone Normal, $\bar{g} = (0002)_\alpha$

(iii) Some dislocation tangling occurs in all alloys at higher strains, but the strain required to produce tangling increases with increasing Al content.

Several additional observations specific to alloys which exhibit coplanar slip, i.e.>5 wt % Al, can also be listed.

(i) The thickness of the slip bands decreases with increasing aluminum content. The extent of basal slip at low strains decreases with increasing aluminum content, resulting in slip predominantely on prism and pyramidal planes (especially at yield).

(ii) Intersection of two prism slip bands often results in blockage of one of the bands. In addition, contrast experiments show that when interpenetration of the slip bands occurs, the dislocation reaction

$$\frac{a}{3}[1\bar{2}10] + \frac{a}{3}[\bar{2}110] \rightarrow \frac{a}{3}[\bar{1}\bar{1}20]$$

seldom occurs.

(iii) Cross slip is infrequently observed.

(iv) In the Ti:8.65 wt % Al alloy, dislocation pairs are frequently observed in the quenched (disordered) condition and are always presented in the ordered condition as shown in Figure 20.

(v) Shearing of ordered (Ti_3Al) domains during deformation has been observed in Ti:8.65 Al alloy; an example of which is shown in Figure 21.

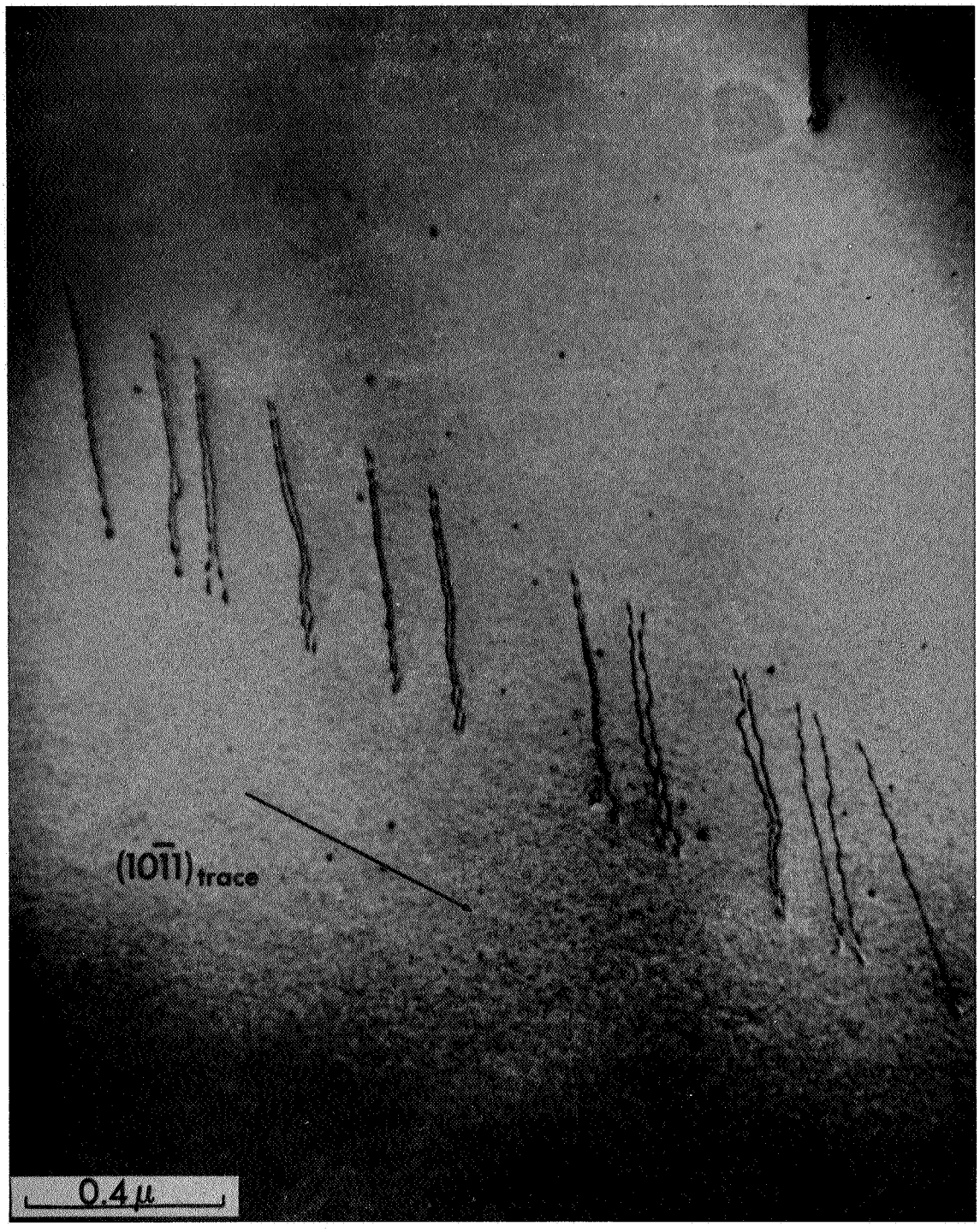

FIG. 20 Dislocation pairs in deformed Ti:8% Al aged at 500°C

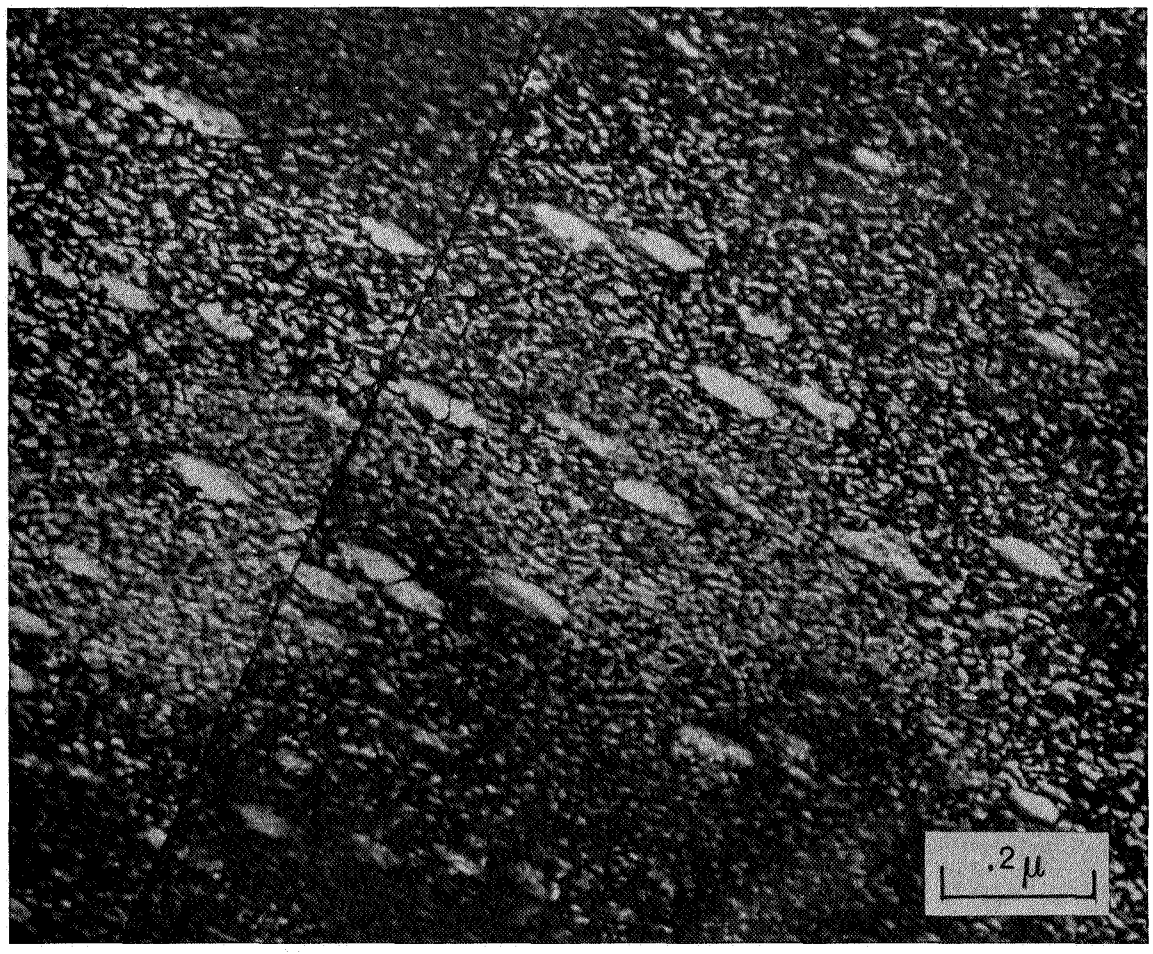

FIG. 21 α_2 particles in step-cooled Ti:8.65 wt% Al which have been sheared during deformation. Dark field, $\bar{g} = [10\bar{1}1]_{\alpha 2}$, $[11\bar{2}0]_{\alpha}$ Zone Normal

Dislocation arrangements have also been studied in deformed commercially pure titanium containing high (0.38 wt %) oxygen. This material also exhibits a marked tendency toward coplanar slip as shown in Figure 22. The slip bands in this material are comparable in thickness to those found in a 6 wt % Al alloy.

(c) Fracture

The fracture surface of a SCC specimen is generally characterized by several macroscopically distinguishable zones as shown in Figure 23. The zone resulting from crack propagation by SCC is marked 'B' while the zone marked 'C' corresponds to rapid fracture after K_{IC} has been reached.

In the type of tests reported here, we can vary the relative extent of these zones by varying the crosshead speed and its direction of motion after slow crack growth (SCC) begins.

Electron fractography has been used to study the fracture mode associated with SCC and several observations can be listed.

(i) The occurrence of cleavage fracture characterizes SCC in all susceptible alloys as shown in Figure 24.

(ii) Regions of ductile fracture are observed in the Ti:8-1-1 alloy. It has been shown that ductile rupture of beta or martensitically transformed beta regions result in such regions and that the alpha

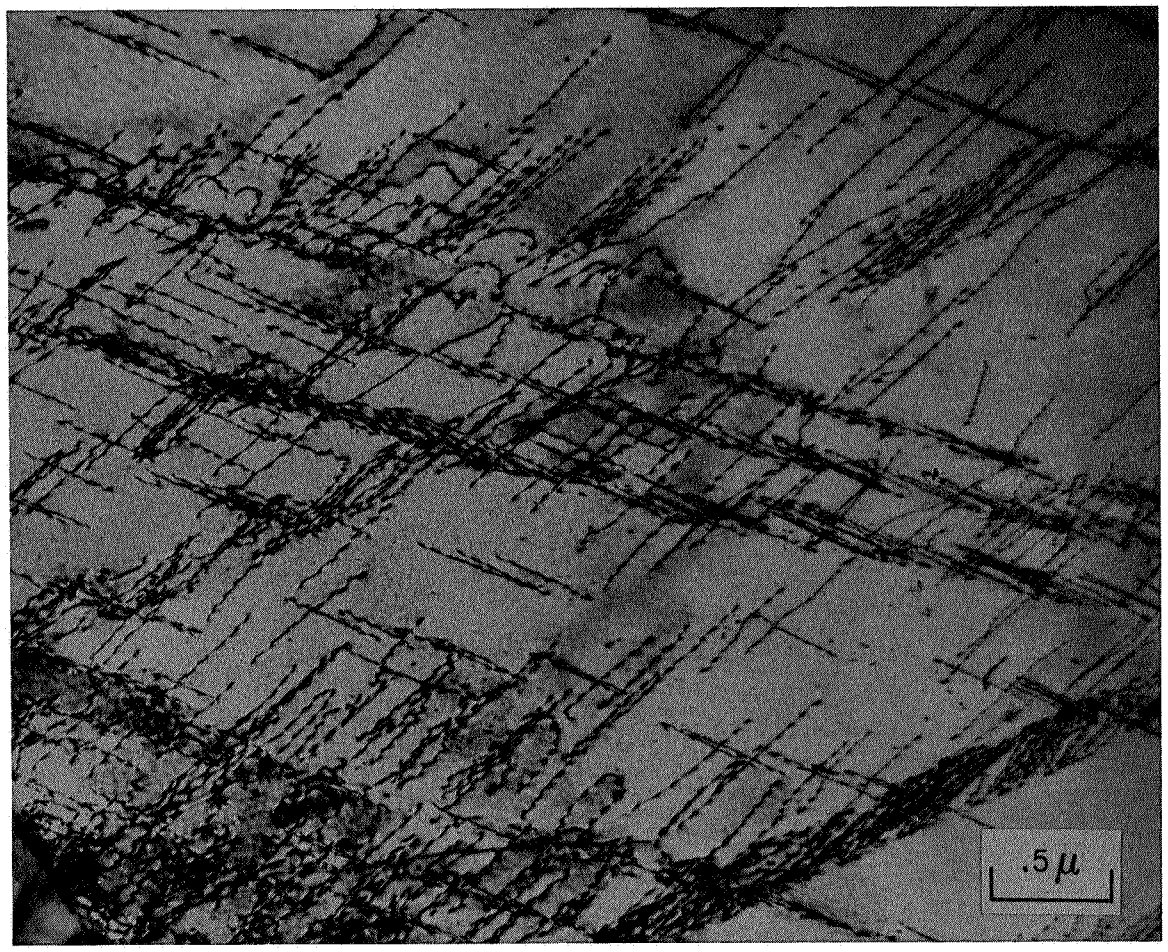

FIG. 22 Dislocation Arrangements in Deformed, High Oxygen Commercially Pure Titanium (3800 ppm oxygen) Showing Tendency Toward Coplanar Slip. $[11\bar{2}3]_{\alpha}$ Zone Normal

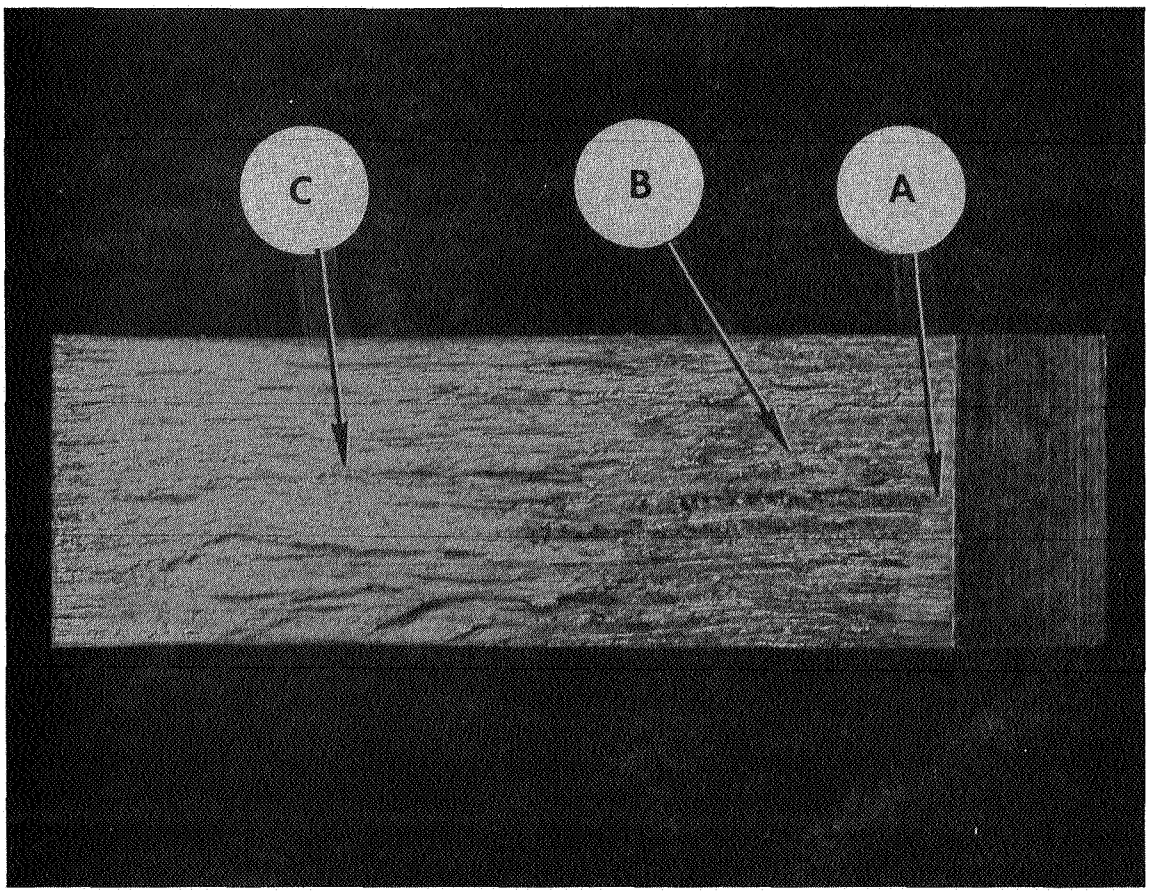

FIG. 23 Fracture surface of 0.500" thick notch bend SCC specimen showing fatigue precrack (A), stress corrosion crack growth (B) and rapid fracture (C). Approx. 4x magnification

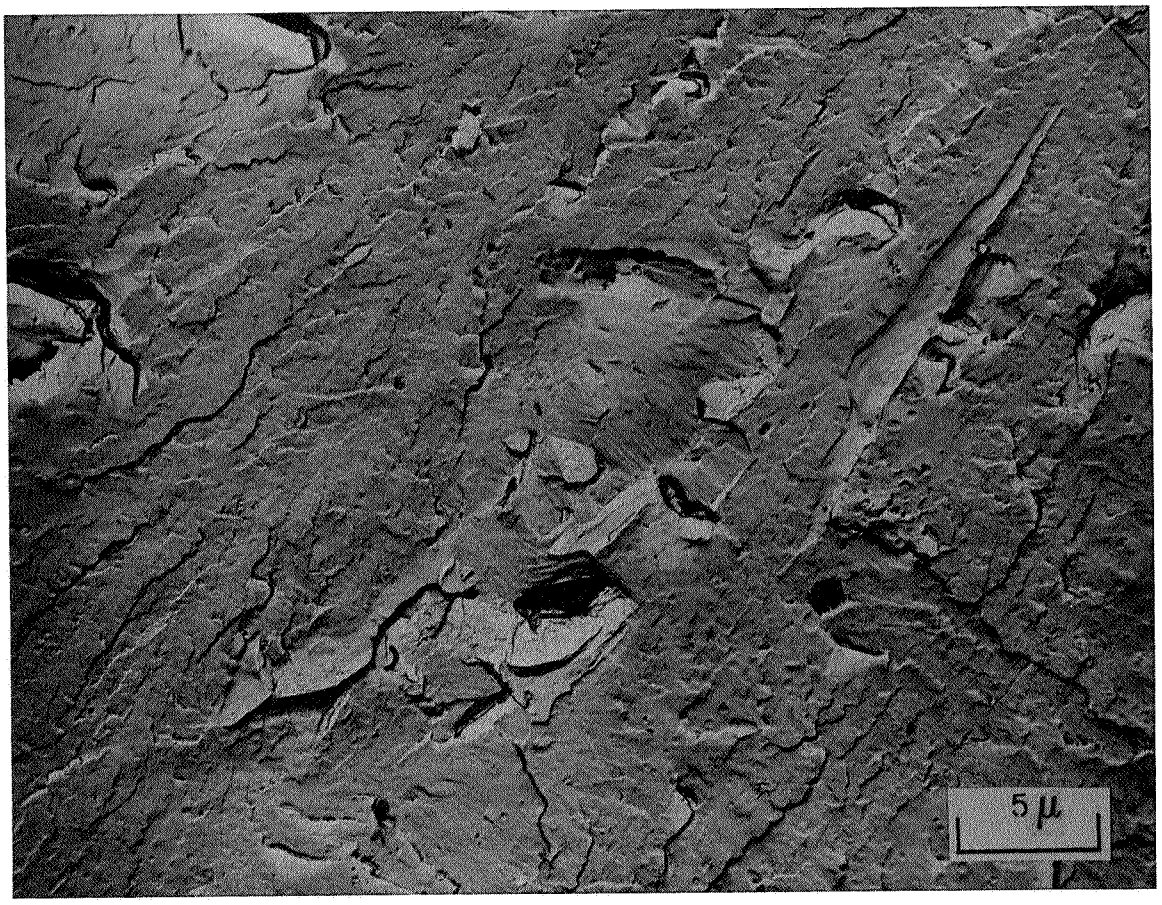

FIG. 24 Electron Fractograph from SCC Zone of a Ti:8-1-1 Specimen Showing Cleavage of Alpha Phase

phase fails by cleavage.

(iii) The fracture mode of the alpha phase usually changes from cleavage in the SCC zone to ductile rupture in the rapid fracture zone.

(iv) As K tends to K_{IC} the areal per cent of cleavage decreases although the transition zone is usually relatively narrow.

The crack path has also been observed optically on electropolished specimens of Ti:Al and Ti:8-1-1 alloys. As seen in Figure 25, the crack is branched and follows an irregular path. Movies taken of the propagation of the surface crack in Ti:8 % Al indicated that propagation occurs discontinuously. However, the branched nature of the crack and the continuity of the current-time plots indicate that cracking is continuous but the macroscopic crack front advances discontinuously.

The cleavage plane has been determined using standard back reflection x-ray techniques in coarse grained specimens of the Ti:8 % Al alloy fractured in air and by SCC. In both cases, the cleavage plane can be described by a 12-14° rotation from the basal plane about $[1\bar{2}10]$ and thus is of the type $\{10\bar{1}7\}$ or $\{10\bar{1}8\}$. The physical significance of this plane is not clear at present.

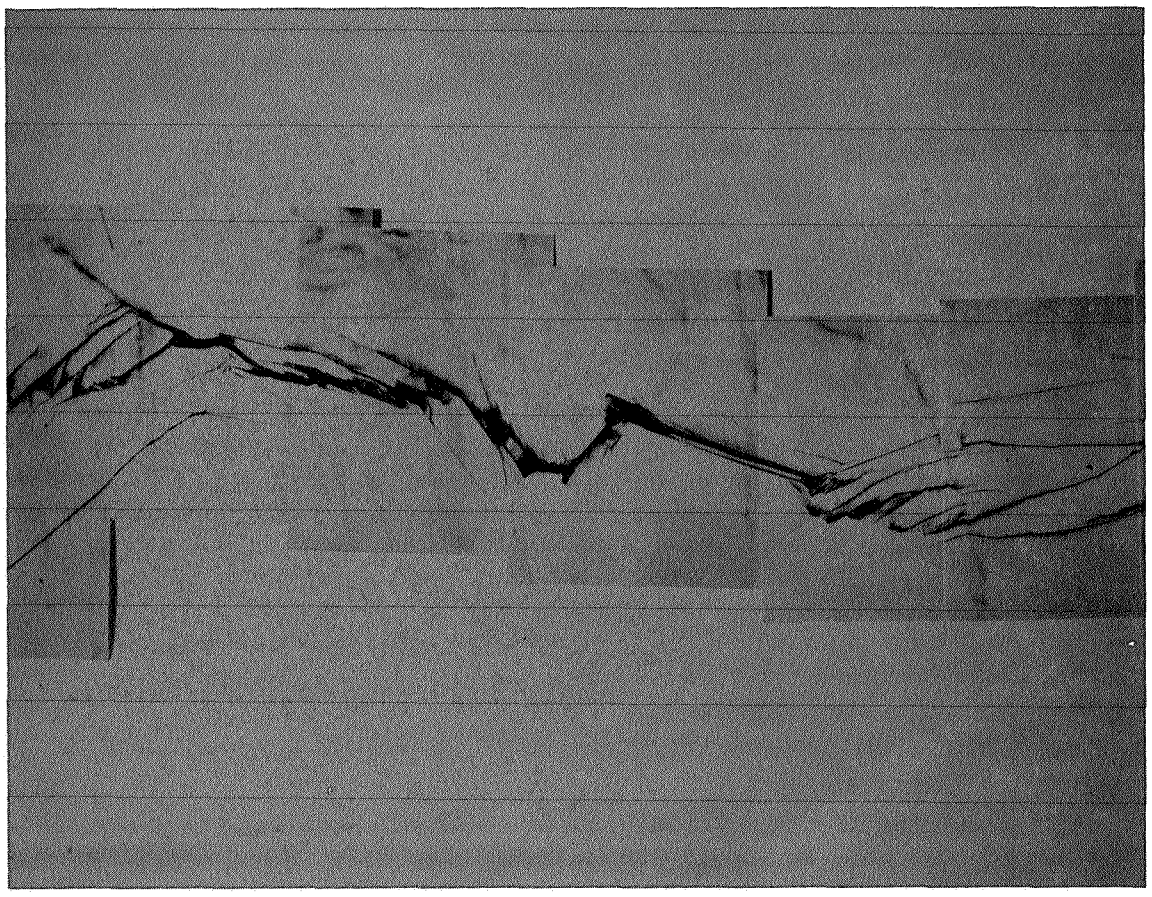

FIG. 25 SCC Crack Profile in Ti:8.65 wt% Al Showing Extensive Branching of the Crack and Limited Extent of Plastic Deformation Which Accompanies Cracking. Magnification: 9 X

(d) Effect of Heat Treatment

1. Fracture Initiation in Ti:8-1-1:

The effect of heat treatment on susceptibility to SCC has been studied in a 0.060" sheet of Ti:8-1-1. Specimens were quenched from a series of solution treatment temperatures and tests performed in air and in 0.6M KCI at -500 V. The results were plotted in Figure 26. However, before analyzing these results several points must be made.

(i) The tests were performed on equiaxed specimens, excluding the transformed structures.

(ii) It should be emphasized that the comparisons are relative as changes in heat treatment produce changes in the fracture mode. Thus, specimens tested in air failed under plane stress and some of the specimens tested in KCl failed under plane strain conditions. Larger specimens are required for an absolute comparison. (Such specimens, however, have the drawback that different cooling rates are produced at the surface and mid section, leading to differences in structure through the thickness.)

(iii) Recent work at NRL has shown that the environment of heat treatment produces changes in susceptibility (16). We have encountered an apparently similar effect in this study. Crack initiation in air in specimens heat treated at 500 to 600°C were found to be dependent upon

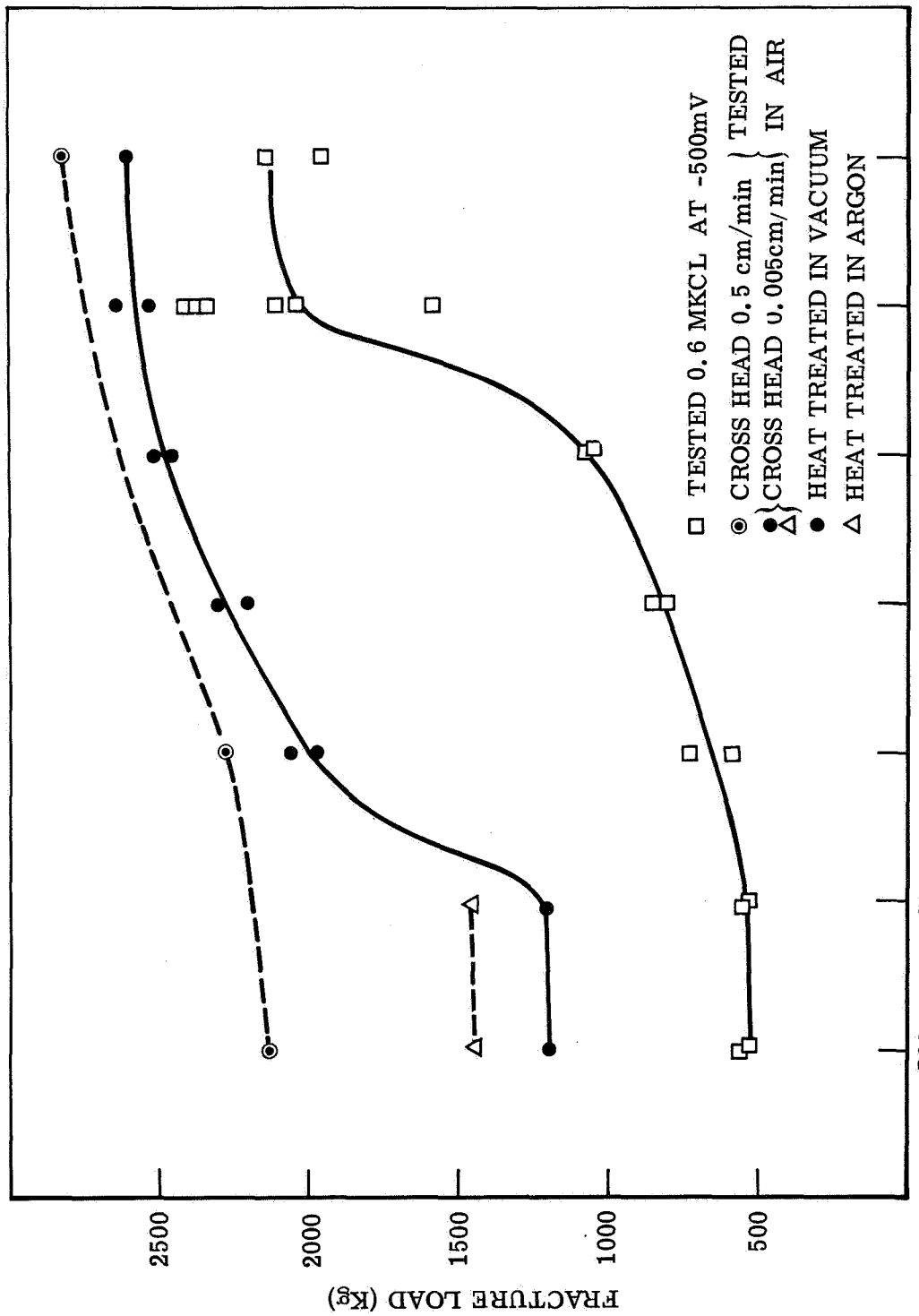

FIG. 26 Sheet 2283. Variation of fracture load with solution temperature for Ti:8% Al:1% Mo:1% V

environment as can be seen in Figure 26. However, these differences were not so marked in specimens tested at faster rates. (See (iv) below or in specimens tested in KCl.)

(iv) Slow crack extension occurred in specimens heat treated at 500 or 600°C which leads to inaccurate air fracture load values. Slow crack growth could be eliminated by testing at faster rates as shown in Figure 26 when the obvious discontinuity between 700°C and 600°C disappears for specimens tested in air.

(v) The phase change $\alpha \rightarrow \alpha + \alpha_2$ that occurs below 680°C is rather sluggish and long aging times are required to approach equilibrium. The effect of this is far more evident in the velocity changes discussed in the next section.

From Figure 26 the following points can be made. Increasing solution treatment temperature tends to increase the fracture load in both air and KCl. For specimens tested in KCl there is a discontinuity between 900 and 1000°C which corresponds to a rapid decrease in the volume fraction of primary α-phase and to the production of the martensitic phases α' & α". Specimens quenched from 1100°C have a completely martensitic structure, α", which although it has a hexagonal structure appears to be virtually immune to SCC.

This behavior should be contrasted with that of the martensites in Ti:8 % Al, discussed below, and in Ti:5 Al-2.5Sn (17) which are susceptible to SCC. The fracture load decreases with solution treatment temperatures below 900°C. Although, as we shall show in the next section, there is a considerable change in velocity between 600 and 700°C, the SCC fracture load does not show a discontinuity in this alloy. However, in material that is step cooled from 800°C a much larger change can be produced; the maximum difference that has been observed is ~600 Kg which corresponds to a change in K of ~24 ksi/$\sqrt{in}$.

The above results apply to specimens which are at equilibrium at the solution treatment temperature, quenched and given no subsequent heat treatment*. It has been shown that retained β-phase can decompose during low temperature aging, and this decomposition has been described in some detail elsewhere (11, 13). It was shown that the ω-phase forms after very long (10,000 hours) aging times at 260°C. Formation of this phase influences susceptibility of Ti:8-1-1 as shown in Table VII producing approximately a two-fold increase in velocity without large changes in the initiation loads. A similar effect has been observed in commercially pure titanium containing 0.30 wt % Fe and

---

* In this investigation, we have not studied the influence of tempering the martensitic structures on susceptibility

TABLE VII

Summary of Results for Long-Time,

Low-Temperature Aged Ti:8-1-1

Ht. Treatment	Specimen Number	Fracture Load (kg)	V_1	V_2	$\bar{V}$
As Rec. Duplex Ann	1050 (L)	710	0.2	6.25	4.7
+10,000 Hrs at 260° C	994 (L)	713	---	14.1	8.85
As Rec. Duplex Ann	1051 (T)	779	3.38	8.39	6.85
+10,000 Hrs at 260° C	990 (T)	750	5.21	28.3	13.3

0.38 wt % oxygen. In this alloy, β-phase stabilized by the iron has also been shown to contain the ω-phase, resulting in a very susceptible condition.

2. Effect on Velocity - Ti:8-1-1:

The formation of ordered particles of α_2 in the α-phase although in many cases having a relatively small effect on initiation load has a much larger effect on crack velocity. Figure 27 illustrates the change of velocity with heat treatment for two sheets of Ti:8-1-1. It can be seen that the velocity changes by a factor $\sim$4 between 600 and 700°C. Figure 27 also illustrates the intrinsic differences observed between various sheets of Ti:8-1-1, i.e., sheet 2194 always has a higher velocity than sheet 2283, and it should be emphasized that more extreme differences have been encountered. However, the general shape of velocity: heat treatment curves are the same, i.e., differences being in the absolute velocity values. Velocity is not changed to a large extent by heat treatment in argon or vacuum.

3. Ti:8 % Aluminum

Much less testing has been performed on these alloys and only preliminary results are presented here. The same trends can be observed as in Ti:8-1-1. Thus, with increasing solution treatment temperature the net area initiation stress σ_I* tends to increase and the velocity tends to decrease. As

---

* σ_I is used rather than the initiation load as several different thicknesses were tested.

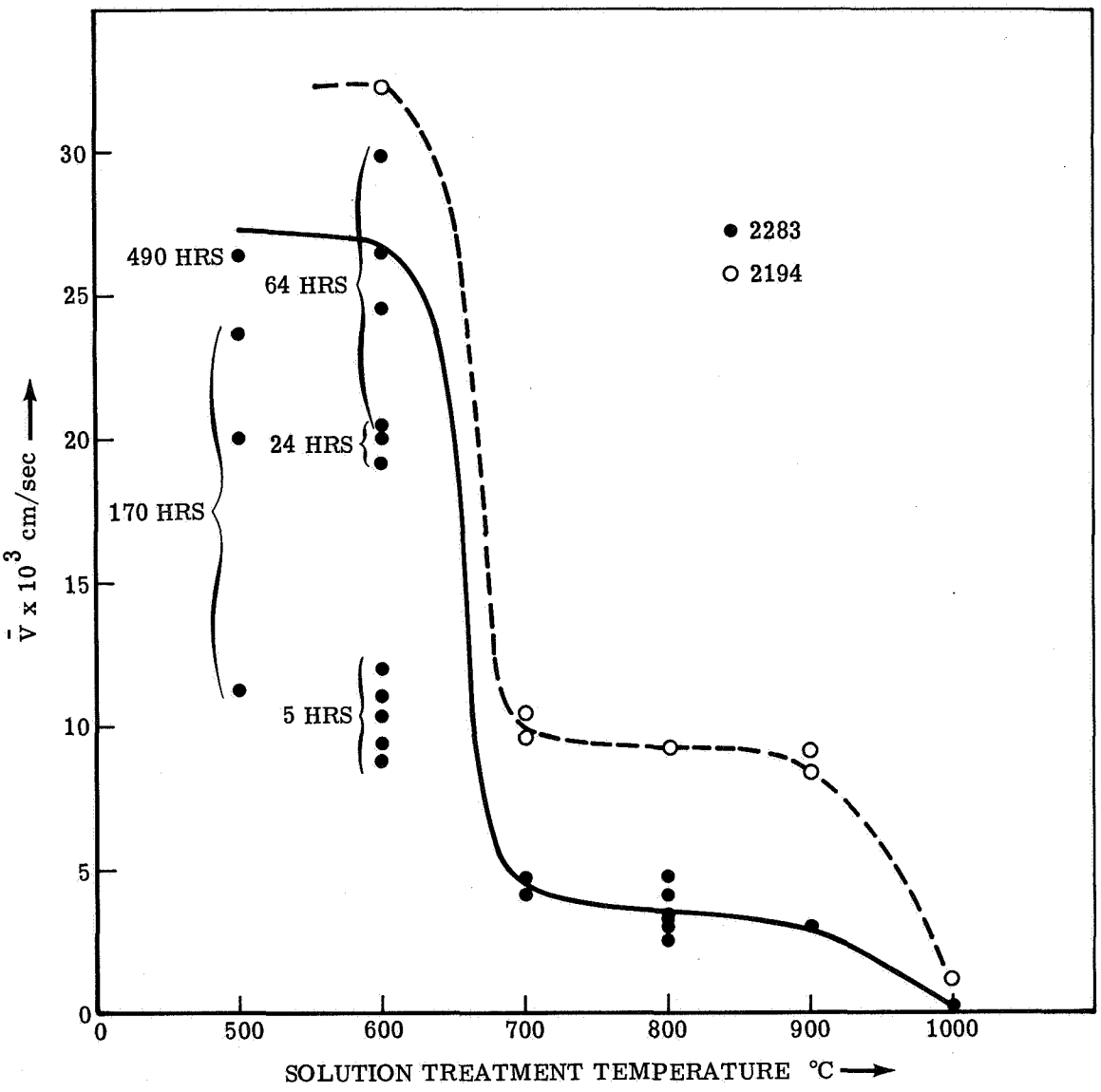

FIG. 27 Variation of Velocity ($\bar{V}$) with Solution Treatment Temperature

with Ti:8-1-1, the velocity shows a discontinuity between 700-800°C, the temperature range in which the α_2 phase boundary is crossed. Grain size has a large effect on v_I as can be seen in Figure 28. In the large-grained specimens, step cooled to produce a dispersion of α_2 phase particles, the velocity was estimated at >0.1 cm/sec and there the fracture may have contained a high proportion of mechanical cleavage. In the fracture of these large grained specimens the amount of plastic flow is very limited. (See Fig. 25).

e. Effect of Stress Intensity

Crack velocity always changes during a test, (See Fig. 14) and it can also be varied by heat treatment. In order to investigate the influence of stress on velocity we have used the methods of linear eleastic mechanics to compute the stress intensity factor, K at the crack tip. Calculations were made for plane strain conditions which are valid over a considerable range of K values in the 0.500" plate specimen but are only valid for low temperature aged or step cooled material in the 0.060" specimens. The data from the 0.060" sheet however shows similar trends as that for the plate material and the results may be used to establish some general behavior patterns.

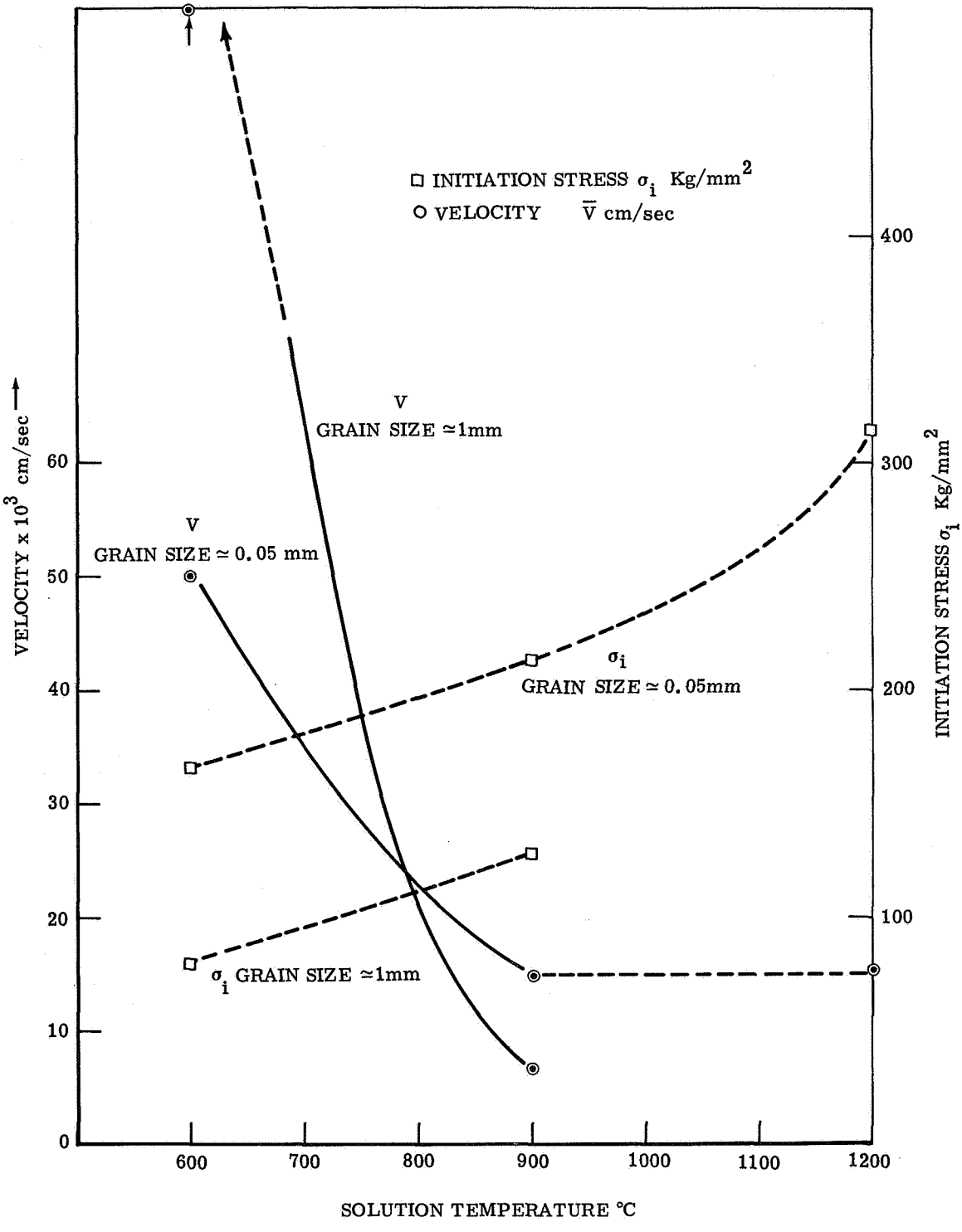

FIG. 28 Summary of fracture and velocity data obtained for Ti:8.65 wt% Al

The results for the 0.5" plate were analyzed both for the variation of velocity with the K value and for the variation of velocity with the time dependent change of K; $\frac{\Delta K}{\Delta t}$. It was found that there was a considerable variation of behavior dependent upon the heat treament of the specimens. Figs. 29 a, b & c illustrate the results for several heat treatment conditions of the 0.500" plate and Fig. 30 illustrates the results for the 0.060" sheet aged at 600° C. The following general observations can be made (at a fixed concentration and potential).

(i) The crack tends to accelerate after initiation. The rate of acceleration varies with heat treatment. Velocity (in cm/sec) varying as $3\text{-}4 \times 10^{-3}$ K, (600° C); $\sim 1 \times 10^{-3}$ K (700° C); and $\sim 0.7 \times 10^{-3}$ (800° C) (K in ksi $\sqrt{\text{in}}$).

(ii) In the 600° C specimen tested under static cross head conditions, the crack appears to reach a constant velocity which is relatively independent of the K level.†

(iii) In the 600° C aged specimen, the acceleration is independent of initial K level.

---

†The velocity tends to increase again in the later stages of a test when $K \rightarrow K_{IC}$

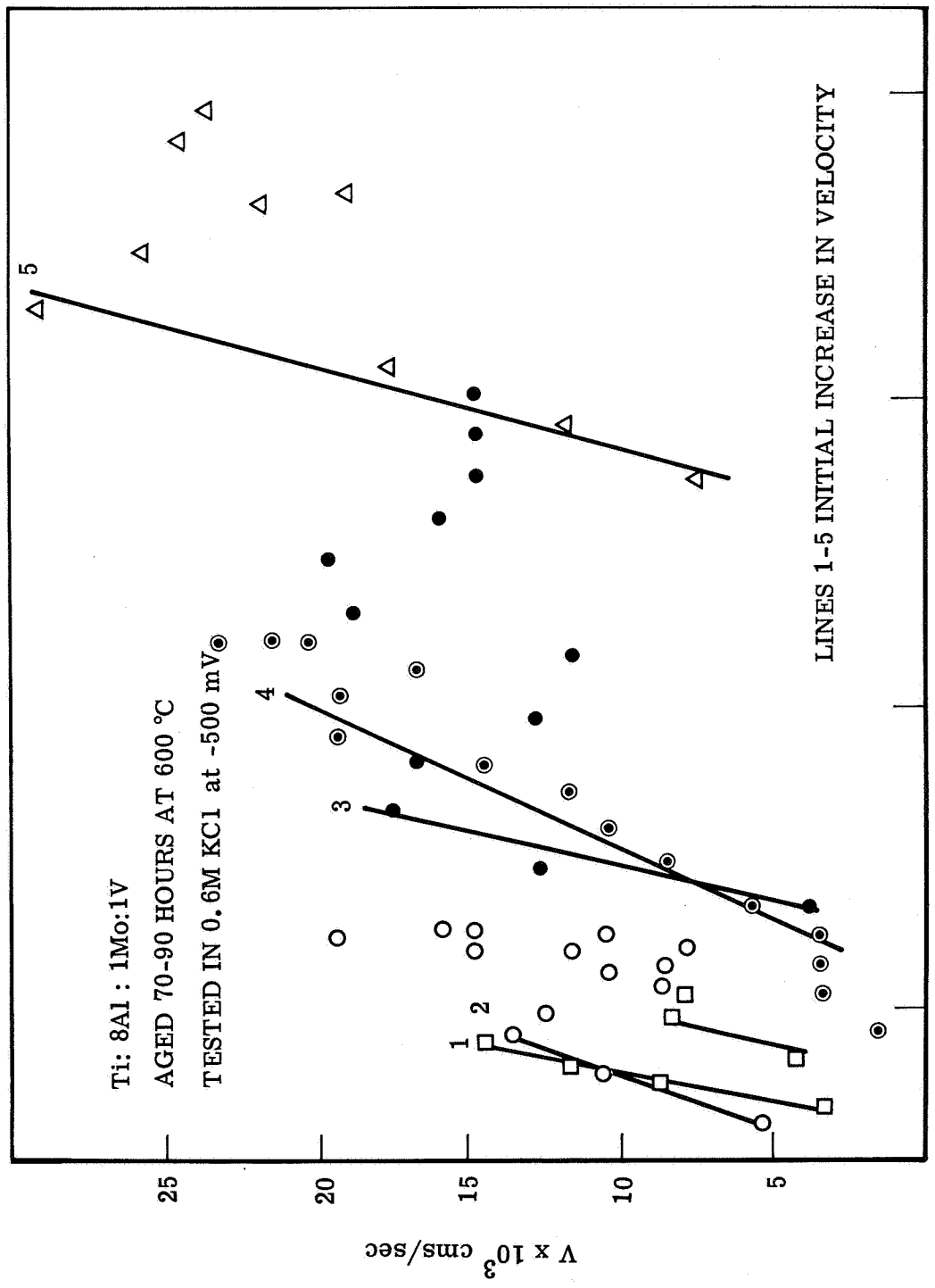

FIG. 29 0.5 inch Plate, Four Point Bend Specimens

(a) Variation of velocity with stress intensity factor (K)

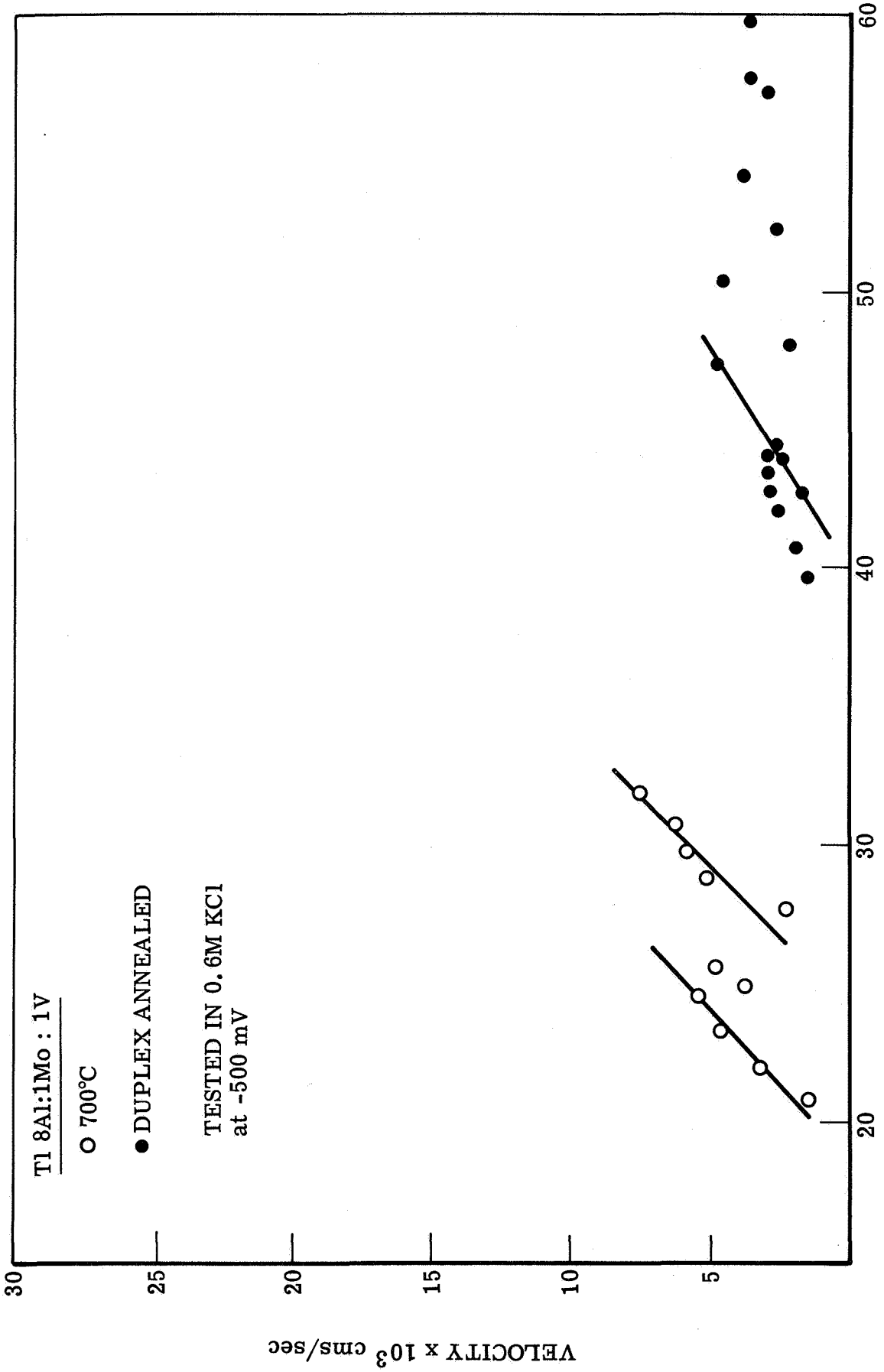

FIG. 29 0.5 inch Plate, Four Point Bend Specimens

(b) Variation of velocity with stress intensity factor (K)

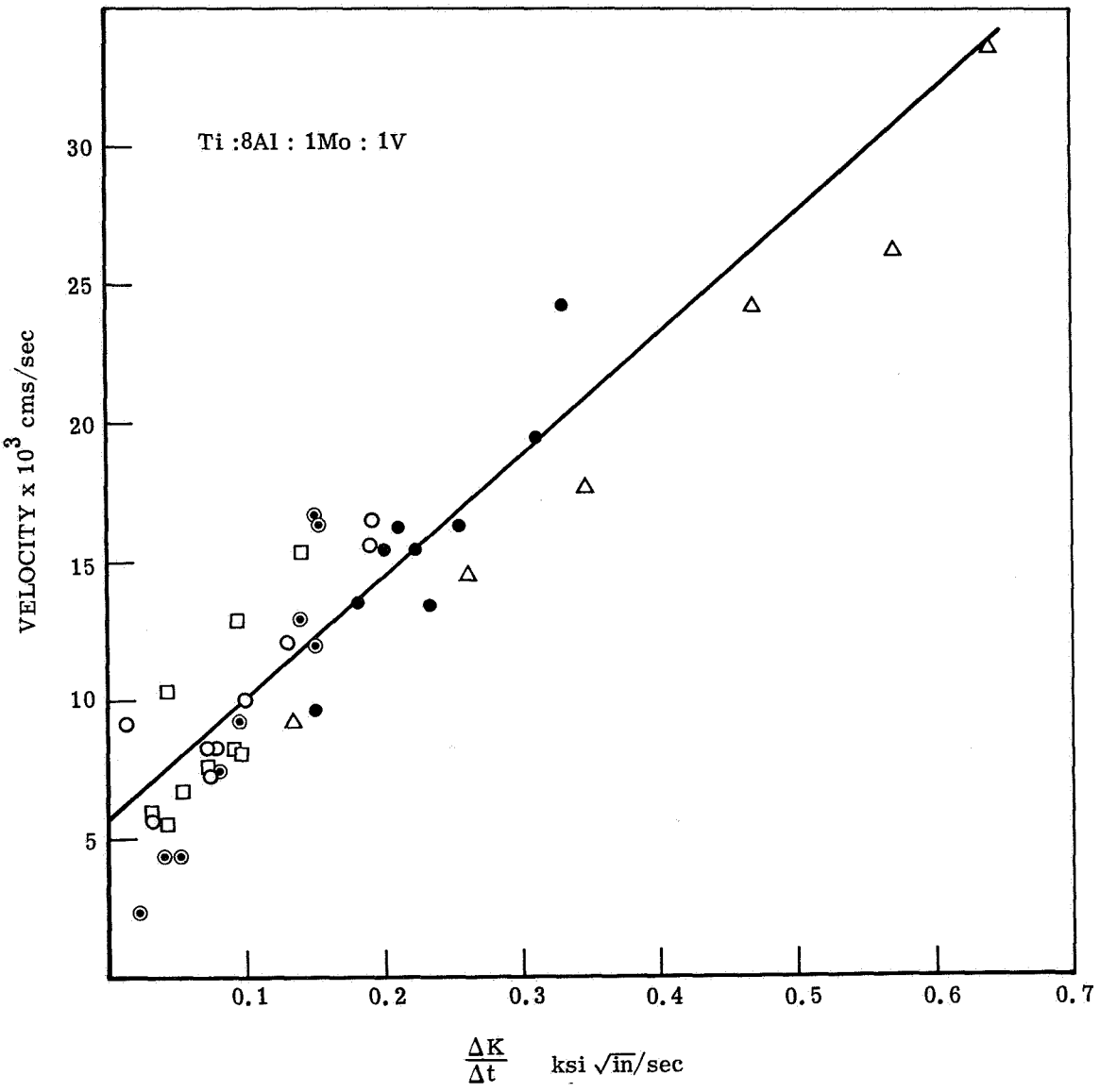

FIG. 29 0.5 inch Plate, Four Point Bend Specimens

(c) Variation of velocity with $\frac{\Delta K}{\Delta t}$; data from Fig. 16(a)

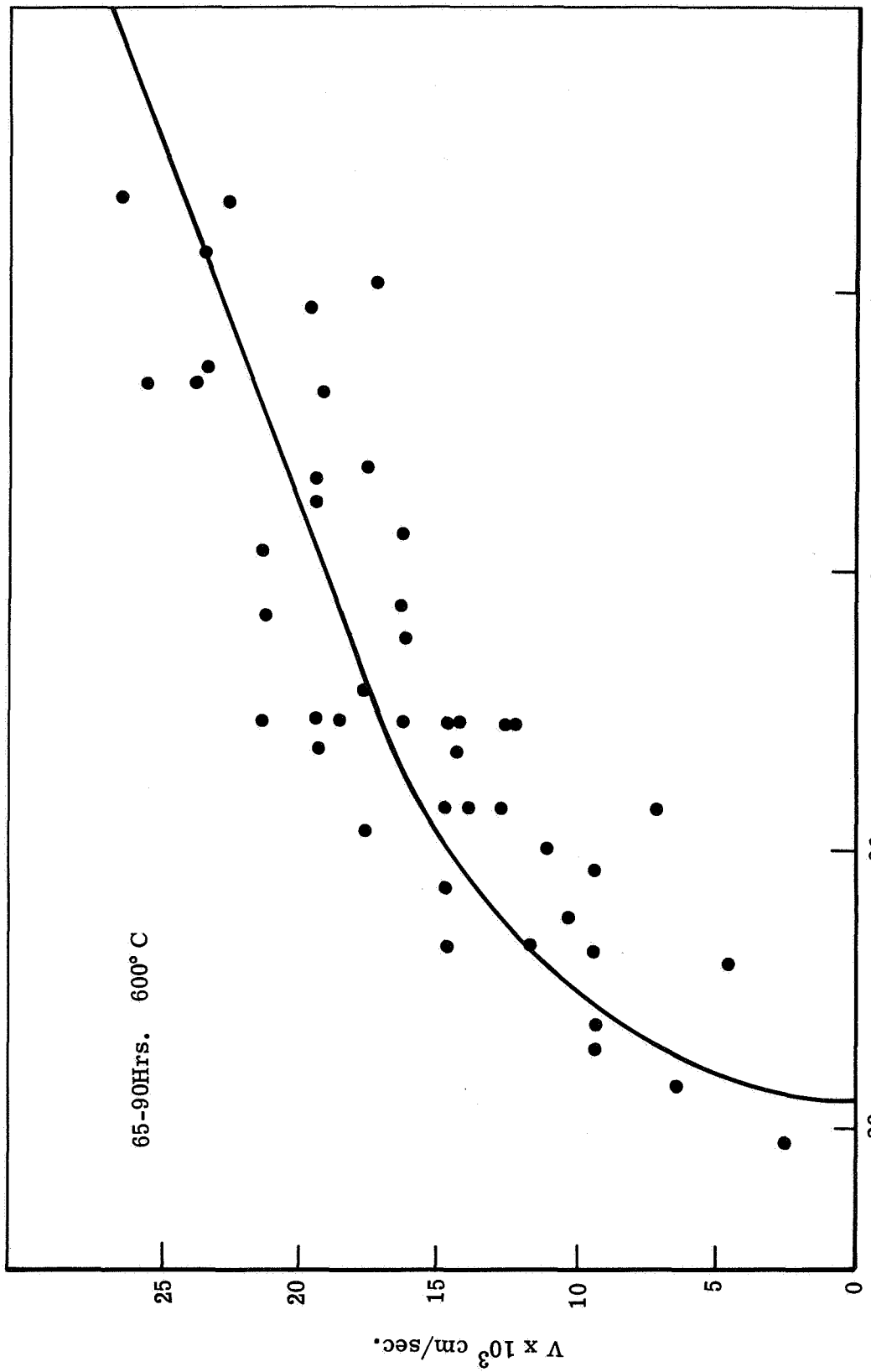

FIG. 30 Sheet 2283. Variation of velocity with K (static crosshead conditions)

(iv) There is a general upward trend of velocity with K level in the 600° C specimens. This is more evident in Fig. 30 for the 0.06" sheet, in which the tests were run under static crosshead conditions. The results shown in Fig. 29 include tests in which the crosshead was reversed and it was found that this influences the velocity.

As the velocity of the cracking appeared to change with the loading conditions, i.e., the rate of change of K, the data shown in Fig. 16a for the 600° C specimen was replotted as velocity versus $\frac{\Delta K}{\Delta t}$. The resultant plot is shown in Fig. 29 from which it can be seen that although there is still considerable scatter, there appears to be a linear correlation. (The correlation from a single test is often good and the scatter possibly reflects slight differences between specimens.) Further, the velocity was found to be approximately constant if a reversed crosshead test was conducted in which K was held constant and thus $\frac{\Delta K}{\Delta t} \simeq 0$. Fig. 31 shows the variation of velocity with potential in such tests. Finally, the variation of velocity with $\frac{\Delta K}{\Delta t}$ for tests at three different potentials is shown in Fig. 32. Somewhat surprisingly, these results appear to lie on the same straight line with slight deviations at large values of $\frac{\Delta K}{\Delta t}$.

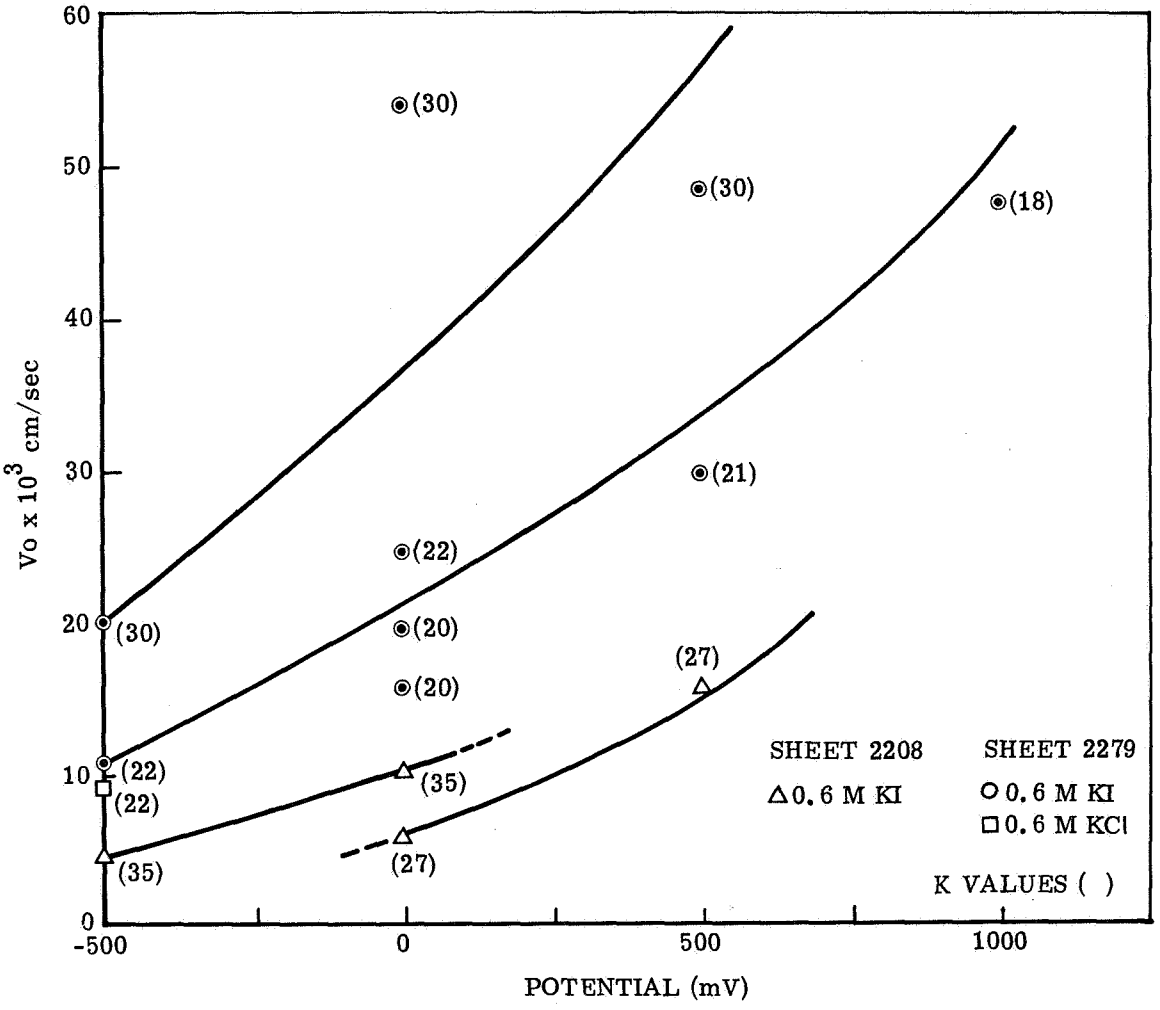

FIG. 31 Sheets 2279 and 2208. Velocity vs. potential (K const, $\frac{\Delta K}{\Delta t} \sim 0$)

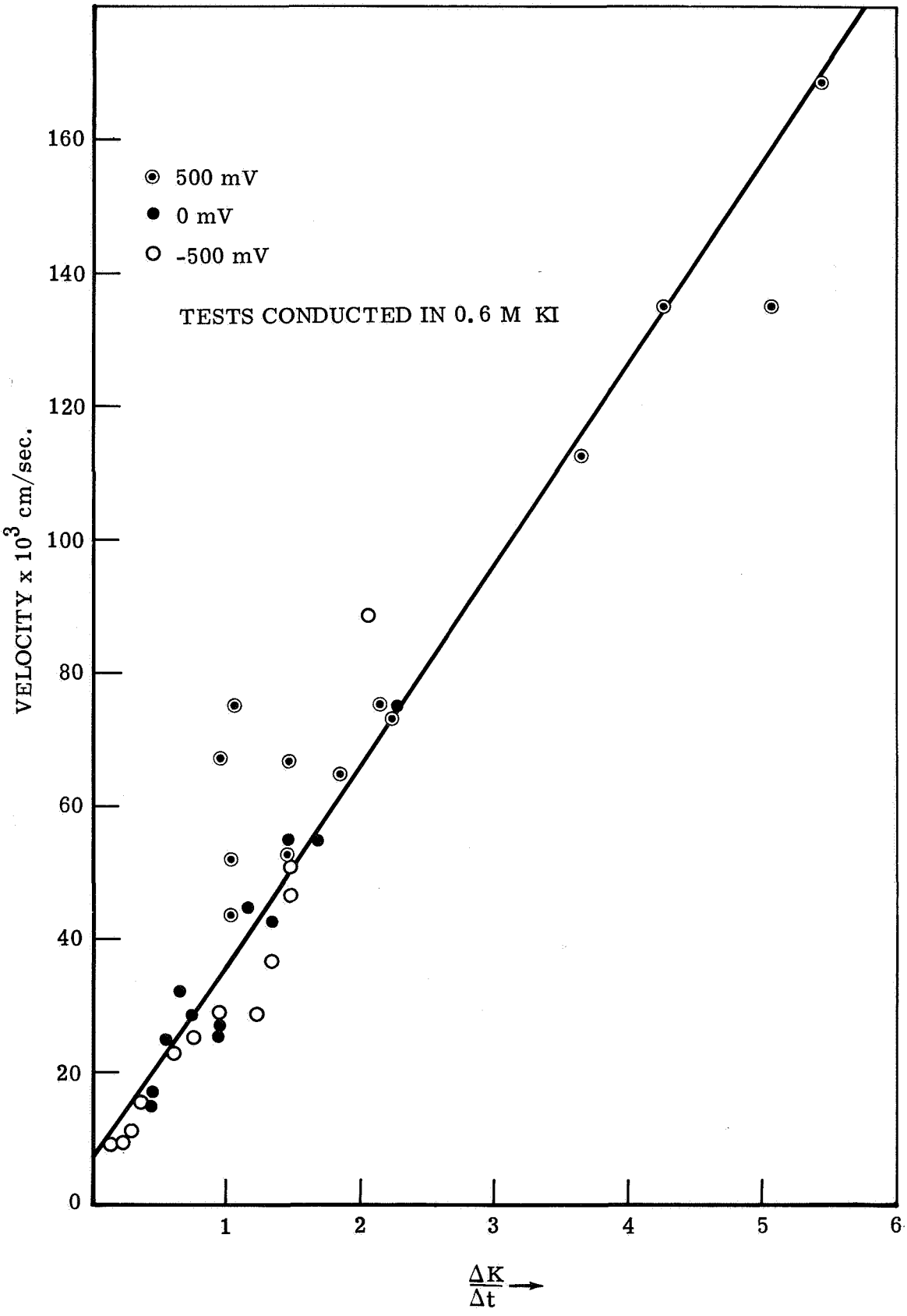

FIG. 32 Sheet 2279. Variation of velocity with $\frac{\Delta K}{\Delta t}$ at several potentials

f. The Effect of Potential Vs. Velocity

A linear relationship of velocity of crack propagation to potential has previously been decribed (1). This determination was for one sheet of material. Although a linear relationship is usually observed, a considerable variation in slope and the intercept for zero velocity has subsequently been found. Fig. 33 illustrates two of the structural parameters that appear to influence such curves. Curves one and two show the variation for specimen orientation taken for one sheet, as can be seen when the crack propagates in the transverse direction the velocity is considerably faster than for a longitudinally propagating crack. Further, a longitudinal crack often propagated at an angle of 30° to the normal stress axis. A second factor is heat treatment, illustrated in curves 3 and 4. From these it can be seen that specimens heat treated below 700° C have a more rapid propagation and are susceptible to lower (more negative) potentials.

g. Preferred Orientation

This effect has not been investigated systematically at present. However, it may be expected that as the cleavage plane is near the basal plane that its general orientation to the applied stress (see discussion) may affect susceptibility. The relationship between preferred orientation and susceptibility to SCC has been demonstrated by Fager and Spurr[17]

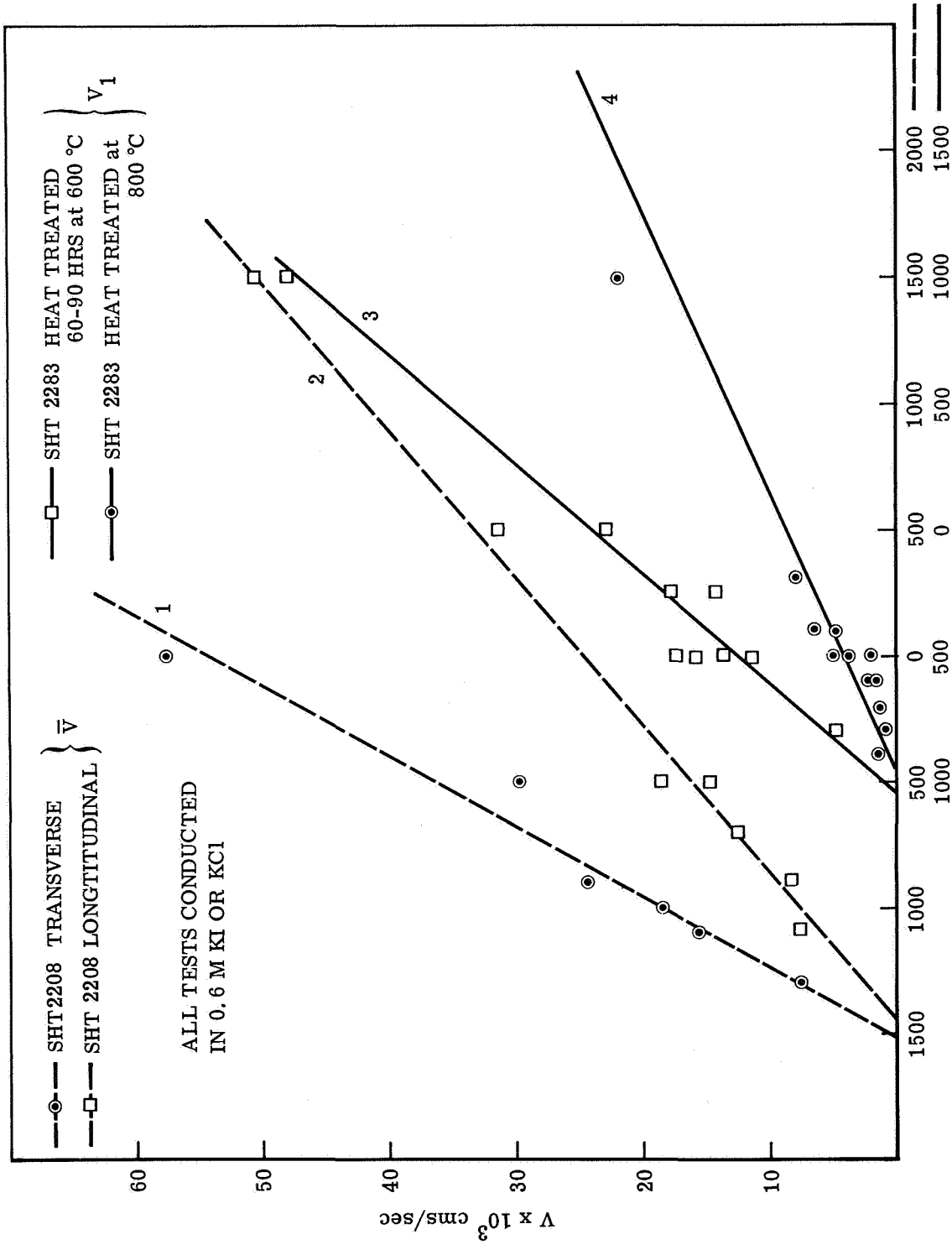

FIG. 33 Variation of Velocity with Potential Showing the Influence of Specimen Orientation and Heat Treatment

for Ti:8-1-1. They showed that when the average cleavage plane is directed parallel to the applied stress then the alloy was essentially immune to SCC. The differences observed in sheet 2208 tested in the transverse and longitudinal directions may have their origin in a preferred orientation effect.

h. Effect of Loading and Unloading Rates

We have described in Sections a & e, the effect of loading and unloading rates on the crack velocity. It is considered that the two stage curves, i.e., showing V_1 and V_2 sections are produced by a mechanical factor in the loading of specimens, i.e., the rigid wedge type grips (3, 3rd Quarterly). If specimens are pin loaded or four point loaded, although the crack still accelerates, the shape of the curve is generally concave upwards rather than divided into two distinct sections.

The second point of importance is whether the initiation of the process is a dynamic or static effect. For instance, it may be postulated that slip has to occur in order to produce fresh surface with which the environment can react. Two observations are relevant to this; firstly the rate at which a crack accelerates is related to the initial loading rate as shown in Fig. 34. Secondly, however, specimens loaded to the SCC initiation load

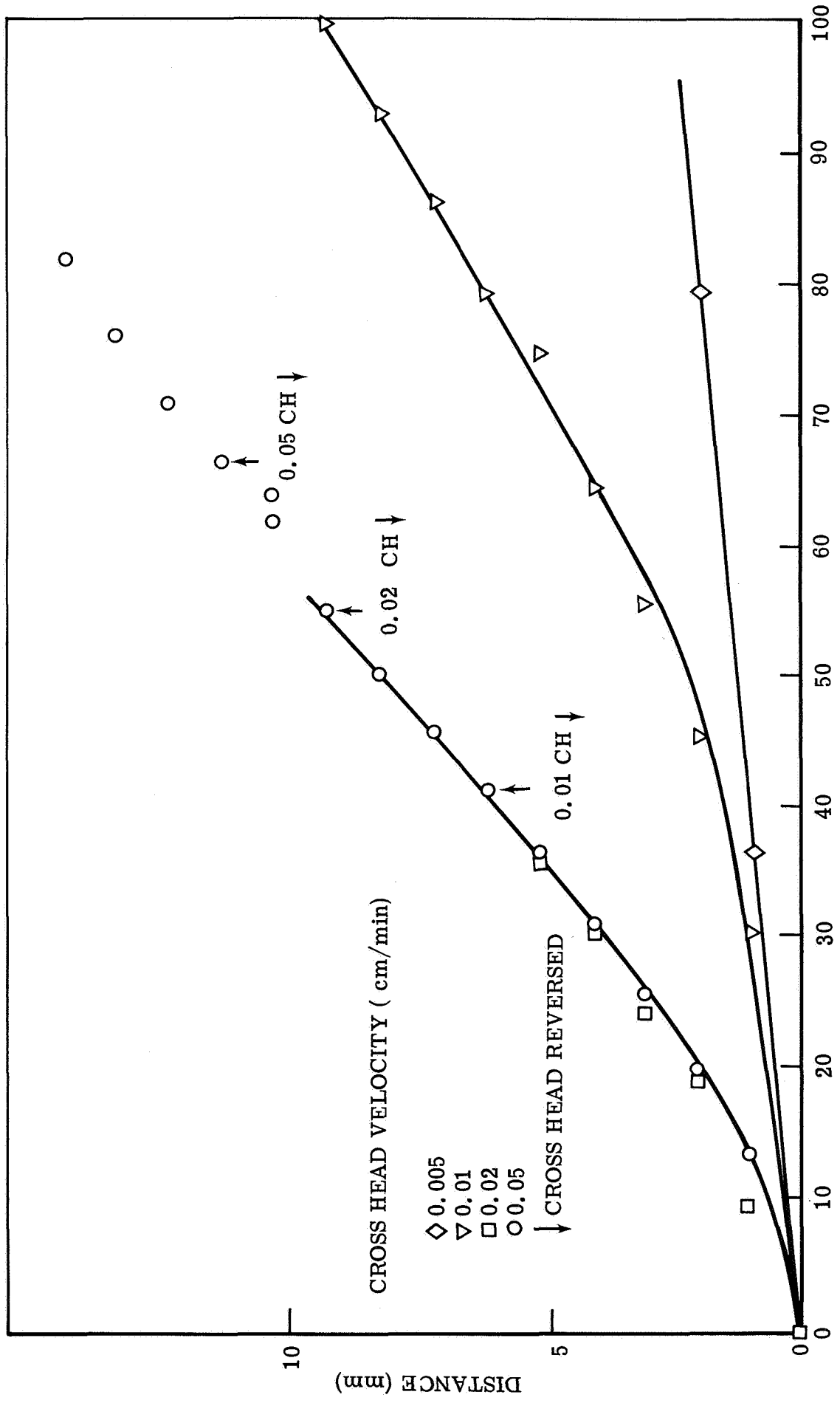

FIG. 34 Distance vs. time for different initial cross head velocity (cross head stopped at crack initiation)

in air and left for periods up to sixteen hours show exactly the same behavior, when the solution is added, as a dynamically loaded specimen, i.e., there appeared to be no induction time before cracking initiated.

3.2.3 Discussion

From this mass of results obtained in aqueous solutions we have to try to extract some of the salient points. Some interpretations are presented here.

(a) Fracture Initiation Criterion

We shall consider a crack initiating under plane strain conditions. As this appears to be a cleavage type process, we shall postulate that these conditions are necessary for SCC of a susceptible alloy:

(i) A critical normal stress.

(ii) The presence of an active environment.

(iii) Rupture of the oxide film (initiation only).

The evidence for the first point is that there is a well defined minimum stress intensity (all other conditions being specified) below which fracture will not initiate or propagate. The evidence for the second point is that if the environment is removed or potential changed to a large cathodic value (-2000 mV) the cracking stops. (Under both

plane strain and mixed conditions). The evidence for the third point is perhaps inconclusive (See Section 3.2.2h) and not really essential to the argument.

We should next attempt to evaluate the normal stress condition for failure. Here the analysis of Hahn and Rosenfield[18] is of relevance as we are dealing with the onset of slow crack propagation and not the actual process of propagation. These workers show that the plastic constraint factor (pcf) in front of a sharp notch under plane strain conditions can be expressed for mild steel by $pcf = 1 + 2\ \frac{K}{Y}$ where K = stress intensity factor and Y = yield stress. This relation is in general agreement with the results of Barton and Hall[19].

The minimum value of K_{INT} (initiation) that we have observed in Ti:8-1-1 is $\sim$10 Ksi $\sqrt{in}$ with a corresponding yield stress Y = 150 Ksi which gives a value of σmax = 1.13Y. For duplex annealed material $K_{INT} \sim 40$ Ksi $\sqrt{in}$ which for a yield stress of 120 Ksi give σmax = 1.66Y. Thus for duplex annealed material it is probable that SCC will occur only under plane strain conditions and thus there will be a limiting sheet thickness below which SCC will not occur. Such a thickness dependence

is in fact observed. K_{INT} tends to decrease as the Ti:8-1-1 is strengthened by precipitation of α_2 i.e. as the yield stress increases, thus at the highest yield strength (150 Ksi) it should become possible to produce SCC under plane stress condition or even in a uniaxial tension test. This is true in the case of Sheet 2279 as shown in Figure 35 which shows the drastic reduction in elongation produced by conducting a tension test in 1.0 M KCl at a potential of -500 mV. To obtain a complete analysis of fracture initiation, for one heat treatment we must consider the following factors: potential, concentration and preferred orientation. The first point is discussed in section 3.1. The variation of K_{INT} with concentration (of HCl) is shown in Figure 36. Finally, to account for the effect of preferred orientation we resolve the applied stress on to the average cleavage plane. Thus we could write

$$K_{INT} = \frac{K'}{\cos^2\phi} \pm (\text{potential term}) \pm (2.25 \text{ Ksi } \sqrt{\text{in}}/\text{decade M})^*$$

Equation 24

* 0.6M = 0

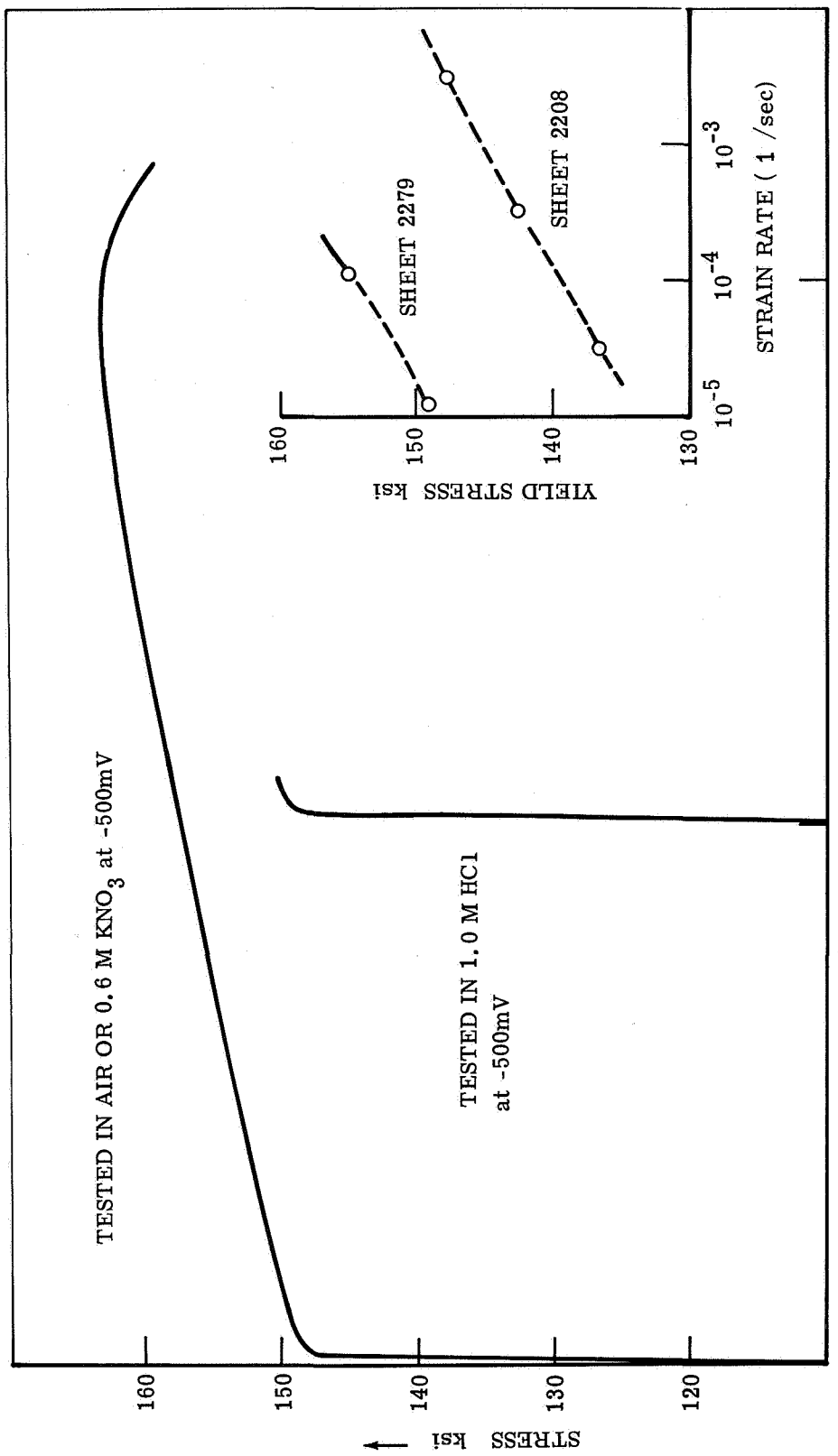

FIG. 35 Sheet 2279. Stress-strain curves for unnotched electropolished specimens tested in several environments

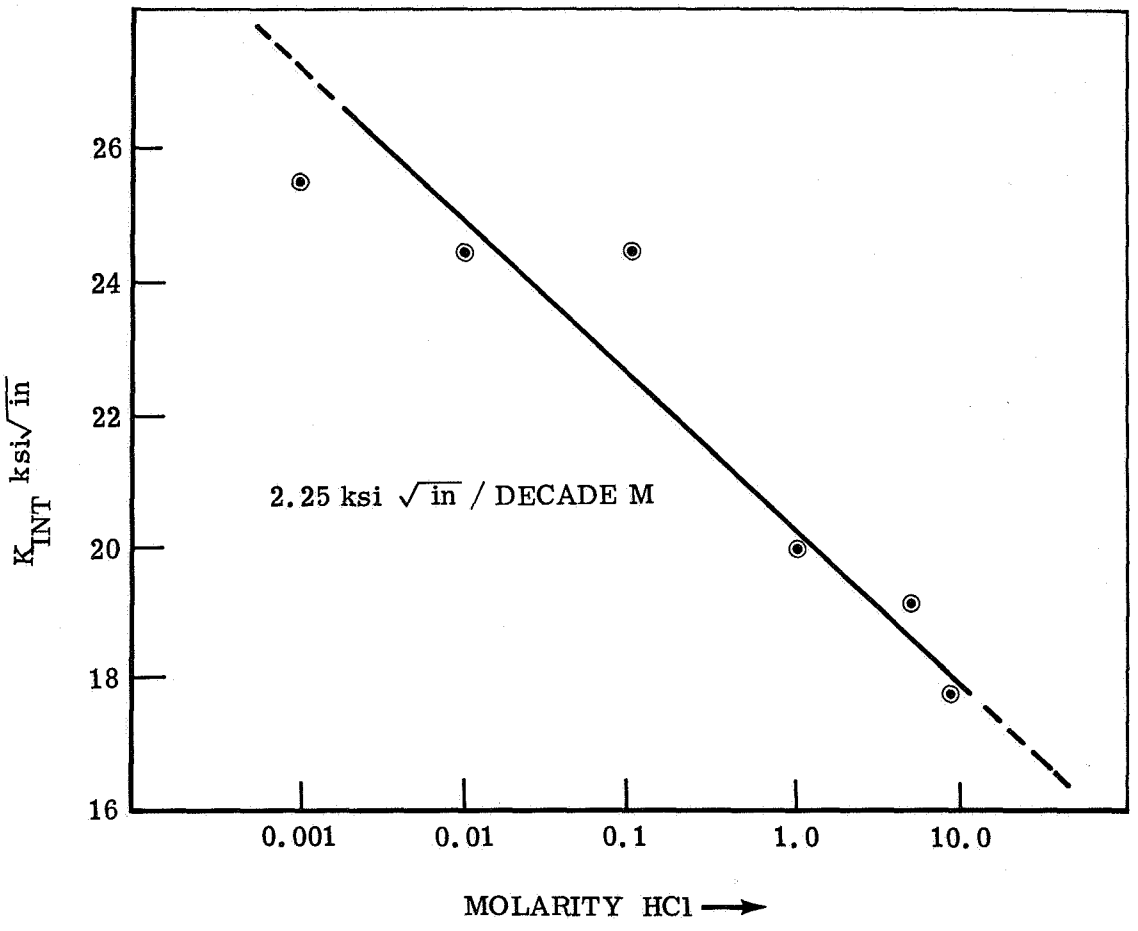

FIG. 36 Sheet 2208. Variation of K_{INT} with Molarity of HCl at -500 mV

where $K'' = K$ when $\phi = 0$, ϕ is the angle between the applied stress axis and the average cleavage plane normal. The variation of K_{INT} with heat treatment below 900° C appears to be approximately proportional to the uniaxial yield stress (Y) and can be expressed by

$$K_{INT} = (240 - 1.56\ Y) \qquad \text{Equation 25}$$

which appears to fit the results for several but unfortunately not all sheets of Ti:8-1-1 that have been tested. It is no doubt possible to construct such empirical equations for K_{INT} for several titanium alloys but due to the number of variables, the amount of work involved is considerable.

(b) Propagation

It has been shown above that the velocity of crack propagation depends upon:

1. Heat treatment
2. K level and $\frac{\Delta K}{\Delta t}$ in some conditions
3. electrochemistry (potential and concentration)
4. preferred orientation

† Y in ksi

We shall not discuss the effect of concentration or preferred orientation here. Consider the alloy after a heat treatment which renders it susceptible to SCC, i.e., heat treated below 900° C. Analysis of the stress intensity at the root of a growing crack and its variation with time has shown the following:

(i) In specimens quenched from above the $\alpha \rightarrow \alpha + \alpha_2$ phase boundary, velocity shows little dependence on K or $\frac{\Delta K}{\Delta t}$, whereas specimens containing a dispersion of α_2 do show a strong dependence.

(ii) The higher the yield stress and more brittle the alloy, the larger dependence upon K and $\frac{\Delta K}{\Delta t}$ (Figure 29 and b).

(iii) The dependence on K level is not easily analyzed from a test in which the K level changes unsystematically (Figure 29 (a))

(iv) The dependence on $\frac{\Delta K}{\Delta t}$ appears to be linear and not much affected by potential (Figure 32).

(v) In test where K is constant and $\frac{\Delta K}{\Delta t} \sim 0$ a constant velocity, V_o, is obtained but V_o is dependent upon the K level (Figure 31)

From these results we conclude that the velocity of crack propagation in a specimen that does not contain α_2 particles is controlled by the electrochemical velocity, V_o. This velocity may have a slight K or stress dependence. It is possible that as K approaches K_{IC} the velocity may increase due to a mechanical contribution to fracture. Analysis of the fracture surfaces indicates that such mechanical failure is ductile and thus Krafft's model[20] may apply.

In alloys containing a dispersion of α_2 the dependence of crack velocity on stress intensity parameters indicates that we have a contribution from both mechanical and electrochemical failure. Such a combination of failure events has been postulated in several models for stress corrosion cracking[21]. In many face centered cubic alloy systems it is difficult to envisage cleavage failure in air as such failures cannot be produced by purely mechanical means. However, such failures can be produced at high strain rates in Ti:8-1-1 containing a dispersion of α_2 phase. Thus we consider that the velocity, V, can be expressed by two terms which are assumed to be additive, i.e.,

$V = V_o + f(\frac{\Delta K}{\Delta t})$ (fixed concentration & heat treatment 600° C) Equation 26

where V_o (a function of K) is the electrochemical term and $f(\frac{\Delta K}{\Delta t})$ is a mechanical term. Insufficient testing has been performed to provide a complete test of this hypothesis but one series of experiments has been performed in KI which indicate that it may apply. Considering first V_o; this increases with potential (See Fig. 31) and also depends upon K level. Tests were conducted at -500, 0 & +500 mV in which range the potential variation can be expressed by

$V_o \times 10^3 = 18(1.100 + \phi)$ where ϕ is the potential in volts. Equation 27

The dependence of V_o upon K can be represented by

$V_o \times 10^3 = (0.5(K) + E)$ where E is a function of potential Equation 28

Thus we can compute V_o for a test at a given potential and a known K level. If the above equation applies then

$$V - V_o = f\left(\frac{\Delta K}{\Delta t}\right) \qquad \text{Equation 29}$$

The data from Fig. 32 are plotted according to this formulation and the resultant plot is shown in Fig. 37 which indicates some validity for the analysis. The exact physical interpretation of the terms in the equation are not clear, but the variation of V_o with K may be related to the crack angle γ, in the electrochemical mass-transport-kinetic model. It is tempting to associate the term $f(\frac{\Delta K}{\Delta t})$ with the strain rate at the end of the crack. It is probable however, that local strain rates are rather high due to the non-uniform crack propagation. The cleavage stress for purely mechanical failure is higher than that for electrochemical mechanical failure and this may explain in part the $\frac{\Delta K}{\Delta t}$ dependence. Further, mechanical cleavage failure probably occurs rapidly, leading to higher overall velocities. This analysis is an over simplification for there is evidence, from Fig. 31, of deviations from the simple (linear) V_o function with potential or K level. Further, if the $\frac{\Delta K}{\Delta t}$ dependence is associated with strain rate this may also be a function of K.

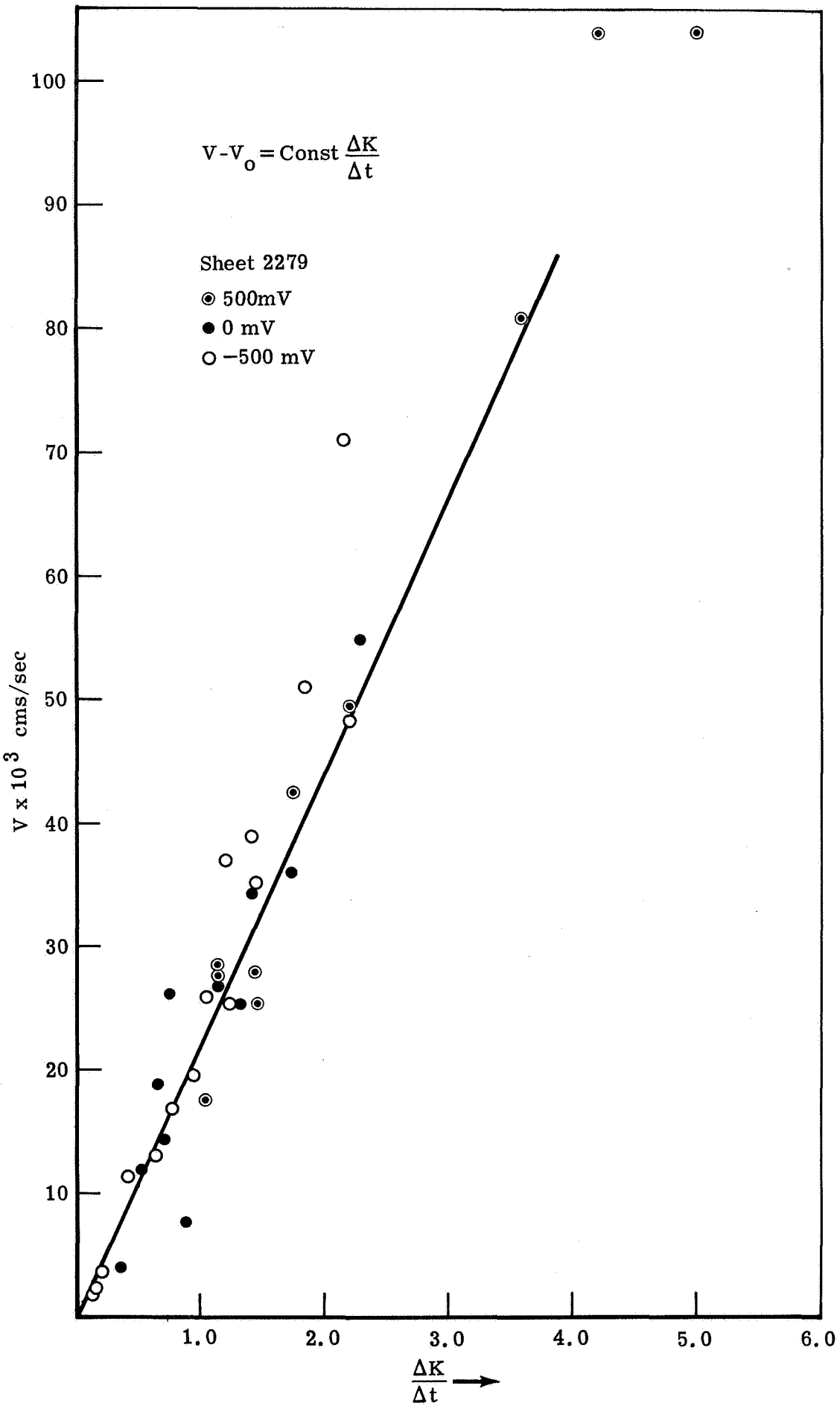

FIG. 37 Sheet 2279. Data from Fig. 19 replotted as (V-Vo) = const $\Delta K/\Delta t$

For instance, Hahn and Rosenfield's formulation[18] of the strain rate at the end of a crack includes a term $\frac{K}{Y}$.

The above analysis applies to high yield stress (and brittle) specimens of Ti:8-1-1. As the yield stress is reduced and ductility increases it appears that both V_o and the $\frac{\Delta K}{\Delta t}$ dependence is reduced and thus for the alloy heat treated above 700° C the dependence of velocity upon $\frac{\Delta K}{\Delta t}$ virtually disappears and the V_o dependence on K also is reduced. This behavior is represented diagrammatically in Figure 38.

(c) Susceptibility Criterion

We consider that the metallurgical factors control the suceptibility of titanium alloys to SCC. Essentially we have to explain:

1. What determines the suceptibility of a given alloy.
2. How does heat treatment etc., effect susceptibility within this specified alloy.

Our general postulate is that is aluminum content of the α-phase has the predominant influence on susceptibility in α and super α alloys. (We have performed little work on β or predominantly β-phase alloys. However, it has been shown that the Ti:Mn and 1311-11Cr-3Al

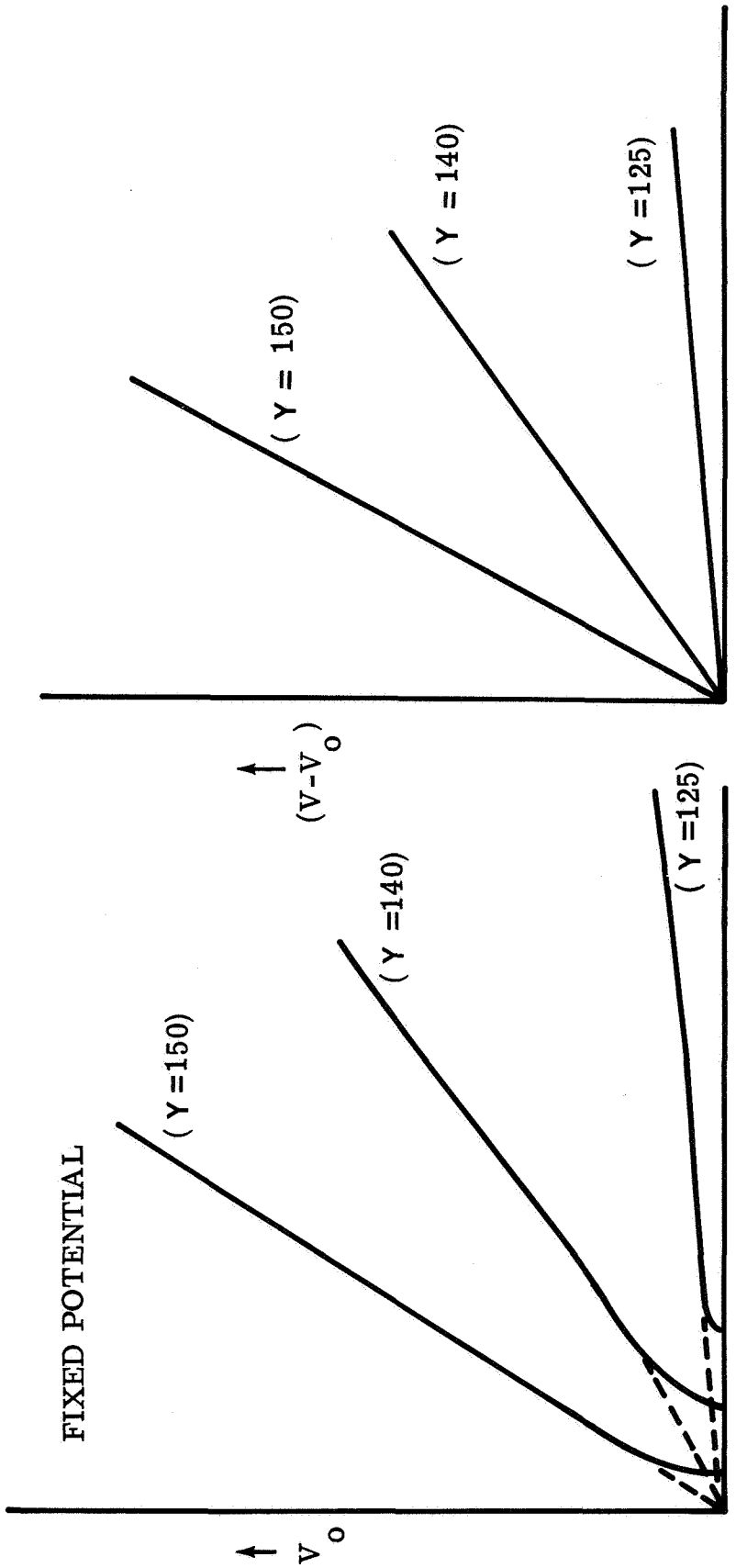

FIG. 38 Diagamatic representation of the variation of V_o and $(V-V_o)$ with K and $\Delta K/\Delta t$

alloys are susceptible whereas we have found that a Ti- 11.6% Mo alloy at least in the as quenched and $\beta + \omega$ aged conditions is not.) Until more systematic work is performed on binary alloys the effect of other alloying elements remains unknown. One may expect that alloying elements that behave in a similar fashion to aluminum may have the same effect, e.g., Sn, In, Ga, etc., and possibly oxygen as long as the electrochemical factors remain about the same.

Returning to our postulate, aluminum additions have been shown to promote the following:

(i) Increased yield strength

(ii) Coplanar slip

(iii) Decreased number of slip systems.

The possible origin of these effects will be described in a separate paper[22]. These factors influence the ductility, plastic anisotropy and work hardening characteristics of the α-phase. Coplanar slip is usually considered a necessary condition for susceptibility to SCC; the arguments usually advanced depend either on the formation of a large slip step for crack nucleation or on a stress concentration at a piled up group to produce a brittle crack. We have no direct evidence for

either of these events but would agree that both probably occur. We would, however, suggest that what may be more important is the inability of the material to relax stress concentrations around a propagating crack. If this is a factor, then the mobility of dislocations would be an important parameter. Possible indirect evidence for this is the behavior of alloys containing the β- phase which has been embrittled by a dispersion of the ω-phase. As the initiation load remains almost unchanged, fracture initiation is still controlled by the α-phase but the velocity of crack propagation is increased. Thus the β-particles no longer act as ductile inclusions and increase the ability of the material to sustain a sharp crack. It has been shown that the cleavage plane in these alloys is of the type $\{10\bar{1}7\}$ - $\{10\bar{1}8\}$ and that the predominant slip vector is $<11\bar{2}0>$. As there is only a 12-15° mis-orientation between the slip vector and the cleavage plane, it is apparent that grains favorably oriented for cleavage will have a low resolved shear stress on the slip systems. Thus it will be difficult to relax any stress concentration by slip and this will accentuate the influence of preferred orientation. Essentially,

we conclude that planar slip may influence nucleation of a crack but the factors listed above result in the ability of the material to sustain a sharp (and propagating crack) in the presence of an active environment. These general considerations explain the increasing susceptibility of Ti:Al alloys with increasing Al content.

In Ti:Al alloy containing 7 wt % Al we have an additional effect, i.e., formation of α_2-phase. Presence of this phase leads to a mechanical component of SCC. There is a correlation in both Ti:8-1-1 and Ti:8 % Al between susceptibility and increasing yield strength. The yield stress associated with α_2 precipitation depends upon the size and volume fraction of these α_2 particles. It has been shown that step cooling produces several sizes of particles. It is to be expected that such a treatment leads to an increased volume fraction of particles compared with an isothermal aging treatment, i.e., one cannot produce a large volume fraction of large particles by an isothermal aging treatment. Yield strength increases with both particle size and volume fraction if the particles are sheared; which occurs in these alloys. This increased yield strength is

accompanied by a reduced ductility and an increased tendency to fail by cleavage. This gives some insight, albeit qualitative, into the increased susceptibility of these alloys containing a dispersion of the α_2 phase.

Finally, considering the variation of susceptibility with solution treatment temperature (>900° C) in the Ti:8-1-1 alloy. The reduction in susceptibility on quenching from high temperatures is associated with the increasing volume fraction of the non-susceptible phases β, α' and α'' and to the corresponding reduction of volume fraction and mean free path in the α-phase. The reasons for the nonsusceptibility of these phases is probably electrochemical in nature and is discussed below.

(d) Electrochemistry

Some of the many of the aspects of the phenomena which are included under this heading have been considered (Section 3.1 and Refs. 1, 3, 4). We will only comment on two factors, which are metallurgical in origin but which have an influence on the electrochemistry. Firstly, β, α' and α'' phases are not susceptible to SCC, while the β-phase in Ti-Mn and Ti:13-11-3(VCA120)and the α''

phases in Ti-Al and Ti:5Al-2.5 Sn are. The most obvious differences between the susceptible and non-susceptible phases are chemical as structurally marked differences have not been detected, e.g., the α'' in Ti-Al and Ti:8-1-1 appear microstructurally identical. Thus we, as other workers, attribute non-susceptibility to the molybdenum and possibly vanadium content of the non-susceptible phases. Secondly, there appears to be electrochemical differences between the behavior of an α-phase containing α_2 particles and one that does not, e.g., in V_o values and in the intercept of potential velocity plots. We do not suggest explanations for either of these observations but they are obviously of practical importance.

In this study we have tried to separate the variables that contribute to SCC of titanium alloys. We consider that it has been shown that the process in neither hydrogen embrittlement (HE) or an oxide wedging process (Section 3.1 and Ref. 3). However, in the above discussion we do not specify the mechanism of interaction of the environment with the metal at the crack tip. Until this is elucidated we consider it premature to attempt quantitative application of dislocation models to the fracture process. Such models treat the

cracking as essentially mechanical, the environment effects being included in the rather nebulous surface energy terms. The evaluation of such energy terms will involve a detailed knowledge of at least the shape of the crack tip, the structure of the electrolyte on this scale and its effect on the surface and possibly on dislocation mobility. Until this stage is reached, it is considered that the continuum and semi-empirical approach used here is the most realistic.

3.3 Proposed Relation of Electrochemical, Metallurgical and Mechanical Effects

An attempt will be made in this section to place the electrochemical, metallurgical and mechanical aspects of SCC of titanium alloys in broad perspective and show how they might be interrelated.

Fig. 39 illustrates an arbitrary conceptual division of regions of study in and around a propagating SCC crack. Linear elastic continuum mechanics can predict the stress field in the elastic region around a crack. Considerable effort has been expended by others in this direction. Continuum plastic models can be applied to the plastic zone around the tip of a propagating crack. Much less work has been done in this area. As a further complication, inhomogeneities in composition and structure can cause perterbations from these continuum approaches, at scales

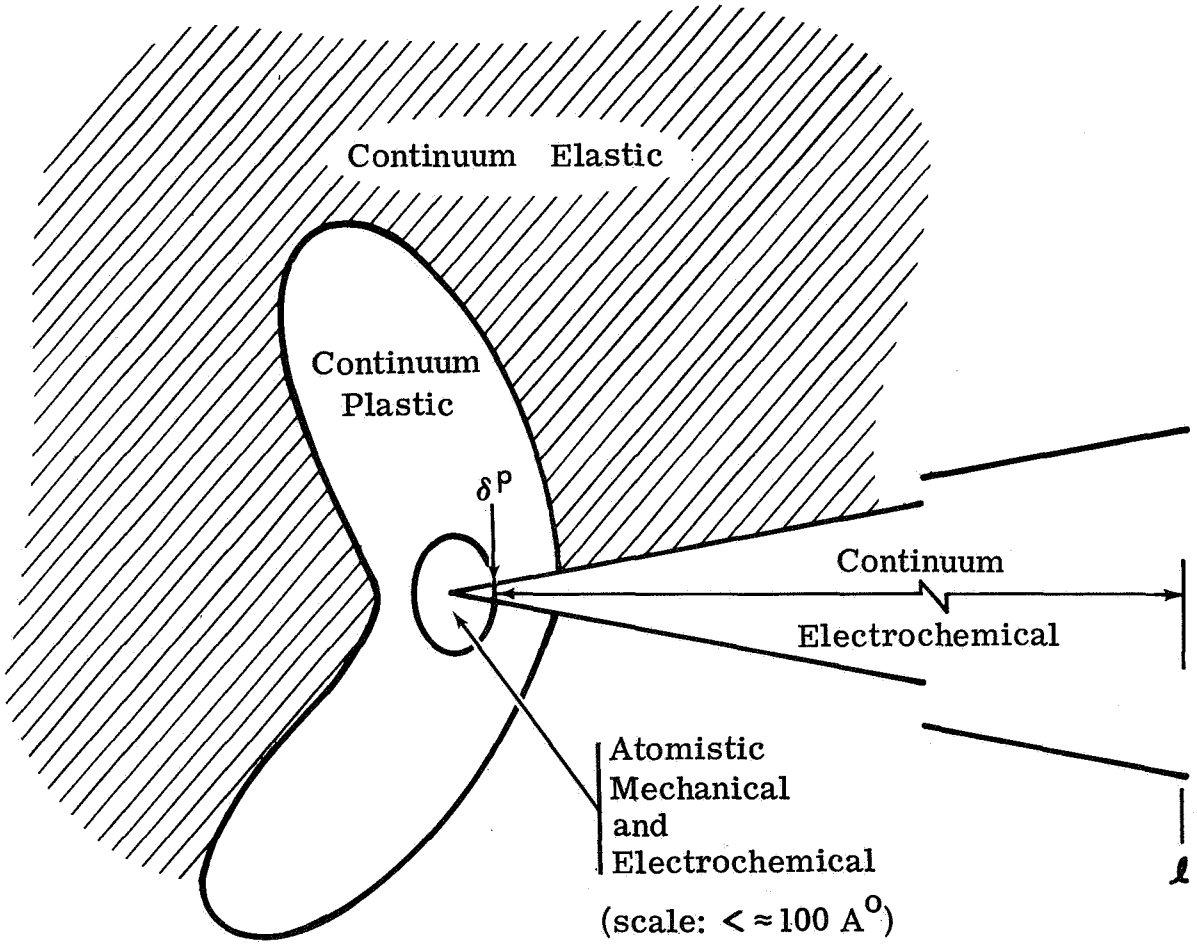

FIG. 39 Regions of Study in and Around a Propagating SCC Crack

considerably larger than atomic. A continuum electrochemical mass-transport-kinetic approach can be applied to the walls and the electrolyte in the crack and results of this approach have been discussed in Section 3.1.

A real understanding of SCC will require knowledge of the interactions between metal atoms and their stress fields at the tip of a crack with the environmental species at an atomic level. Speculations on events at this level will not be fruitful until the events at the macroscopic (compared to atomic dimensions) continuum level are well understood. Nevertheless there are some interactions between the continuum electrochemical, elastic and plastic zones that can be explored.

The continuum mass-transport-kinetic model has two types of parameters that can be related to mechanical or metallurgical effects; the angle, γ, and the kinetic parameters, i.e. the exchange current densities for halide, oxide and hydrogen ion reduction reactions. Outside of the plastic zone the angle, γ, can be shown to be directly related to the stress intensity factor. Within the plastic zone, it is not clear yet what determines the angle so a uniform has been assumed for the whole crack. It is proposed that the approximately linear relation of V_o to stress intensity factor over a range of K (Fig. 38) operates through the crack angle, γ. The differences in SCC behavior between different alloys (Section 3.2) might be related to electrochemical kinetics. Further electrochemical kinetics experiments will be conducted with alloys other than Ti:8-1-1 in order to resolve this question.

The data on SCC velocity versus heat treatment temperature suggest that there may be three regimes of velocity control as illustrated in Fig. 40. Duplex annealed Ti:8-1-1 appears to exhibit nearly pure electrochemical velocity control given by:

$$V_o = a\gamma f(j_o, \phi^o, C^o) \qquad \text{Equation 30}$$

where:

a = a constant

γ = crack angle, $\gamma = bK$

K = stress intensity factor, b = a constant

j_o = exchange current densities

Lower temperature solution treatments have empirically given the relation:

$$V = V_o + \beta\frac{dK}{d\tau} \qquad \text{Equation 26}$$

It is proposed that the $\frac{dK}{d\tau}$ term arises from transmission of shear through the plastic zone to the crack tip, i.e., the strain rate at the crack front possibly raises the local stress level to that for mechanical cleavage. For a given alloy and heat treatment, the greater the value of $\frac{dK}{dT}$ the greater the mechanical cleavage contribution. The velocity might also be described by:

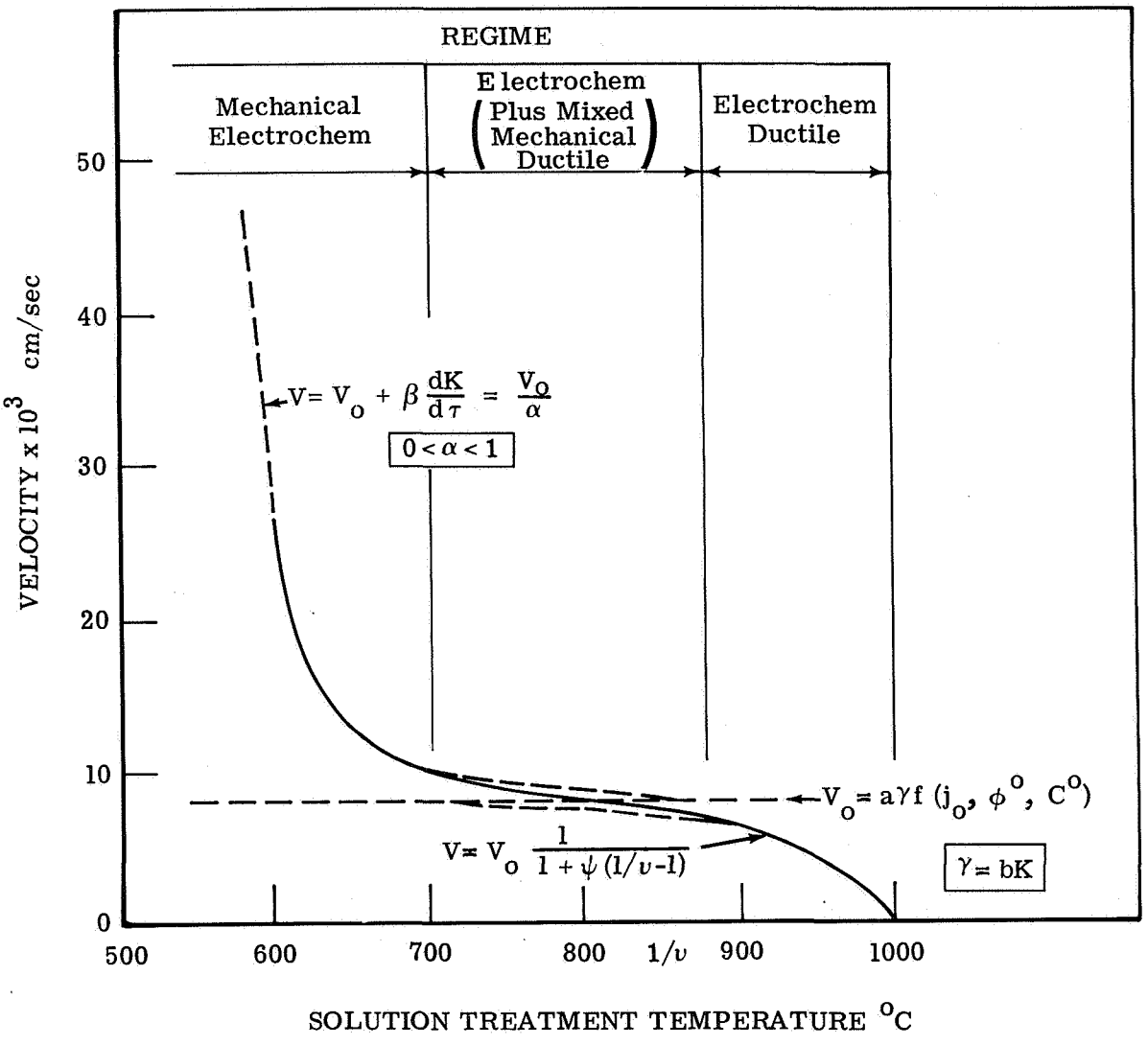

FIG. 40 Proposed Regimes of SCC Mechanisms Versus Solution Treatment Temperature for Ti:8-1-1 in 0.6M KCI @ -500 MV (Note: the value of V_o can shift with heat treatment due to changes in γ or j_o)

$$V = \frac{V_o}{\alpha} \qquad \text{Equation 31}$$

where: α = fraction of environmental (halide) cleavage and $o<\alpha<1$.

Higher temperature solution treatments give ductile inclusions. The crack either has to go around or through these. To go through, the inclusion must fail by mechanical means or by corrosion or oxide or hydrogen embrittlement. (If the velocity through the ductile inclusions is low enough the oxide and hydrogen embrittlement mechanisms may not necessarily be excluded as they are from the main electrochemical mechanism). The velocity may then be described by:

$$V = V_o \frac{1}{1 + \psi\left(\frac{1}{\upsilon} - 1\right)} \qquad \text{Equation 32}$$

where: ψ = fraction of ductile phase

$\upsilon = V_{d/V_o}$ velocity ratio, ductile to pure electrochemical.

The fraction of ductile phase, ψ, that the crack traverses may vary with direction.

While these speculations on interrelation of electrochemical, metallurgical and mechanical parameters on a macroscopic scale are somewhat nebulous they provide a framework for more definitive quantitative experiments.

4.0 CONCLUSIONS

The following conclusions are based on the work accomplished in the period of April 1 through June 31, 1967.

1. An electrochemical mass-transport-kinetic model predicts a limiting tip current corresponding to a monolayer of adsorbed halide ions or titanium halide. A hydrogen ion tip current is excluded by the model.
2. Transient potential time data are consistent with concentration overpotential predicted by the model and theory for decay of concentration overpotential.
3. The -800 mv open circuit potential observed in neutral chloride, bromide and iodide solutions is consistent with a mixed potential in acid solution; therefore, a hydrolysis reaction is suspected near the tip.
4. A cathodic current at potentials more negative than -800 mv is consistent with the mass-transport-kinetic model.
5. The relation of SCC velocity to bulk concentration also indicates hydrolysis. An equation for a simple hydrolysis model was derived which roughly fits the velocity vs. concentration behavior. Many similarities to the previously derived pitting corrosion model exist.
6. A high strength, brittle, form of Ti:8-1-1 produced by step cooling from 800° C gave SCC velocities greater than predicted by the electrochemical model, and evidences of pure mechanical cleavage. The velocity could be expressed by

$$V = V_o + \beta \frac{dK}{d\tau}$$

where V_o is the electrochemically controlled velocity and $\frac{dK}{d\tau}$ is the rate of change of stress intensity factor with β a constant for the particular alloy and heat treatment.

7. Four-point-loaded, 0.5 in. thick specimens gave velocity data consistent with 0.06 in. thick notched tensile specimens.

5.0 FUTURE WORK

The following items of work are planned for the immediate future:

1. Resolve the chloride analysis problem.
2. Refine and extend kinetic studies to other alloys.
3. Include hydrolysis in mass-transport-kinetic model.
4. Investigate metallurgical and mechanical parameters further and develop more quantitiative relationships.

6.0 REFERENCES

1. T. R. Beck, Boeing Document, D1-82-0554, July, 1966, and J. Electrochem. Soc., 114, 551 (1967)
2. T. R. Beck and M. J. Blackburn, Research Proposal, D1-82-0467, August 1965.
3. T. R. Beck, Contract NAS7-489 Quarterly Progress Reports 1, 2 & 3.
4. T. R. Beck and E. A. Grens II, "Analysis of Current Density Distribution in a Propagating Stress Corrosion Crack", presented to the Electrochemical Society, May 9, 1967, Dallas.
5. H. A. Johanson, G. B. Adams, and P. Van Rysselberghe, J. Electrochem. Soc., 104, 339 (1957)
6. W. Latimer, "Oxidation Potentials", 2nd Ed., Prentice-Hall, Englewood Cliffs, N.J., 1952
7. K. S. Vetter, "Electrochemical Kinetics", (Translation) Academic Press, New York, 1967
8. W. F. Spurr, Boeing Document D6A10065-1, p. 18, March, 1966.
9. J. E. Srawley & W. F. Brown,"Fracture Toughness Testing and Its Applications", ASTM, p. 133, 1965.
10. M. J. Blackburn, to be published in Trans AIME, August, 1967.
11. M. J. Blackburn, Trans ASM, 59, p. 694, 1966.
12. M. J. Blackburn, ibid, 59, p. 876, 1966.
13. J. C. Williams & M. J. Blackburn, to be published in ASM Trans, September, 1967.

14. R. D. Jaffee, Progress in Metal Physics, 7, p. 75, Pergammon Press, 1958.

15. F. A. Crossley & W. F. Carew, Trans AIME, 209, p. 43, 1957.

16. G. Sandoz and R. L. Newbegin, Report of NRL Progress, March 1967, p. 28.

17. D. N. Fager & W. F. Spurr, private communication.

18. G. Hahn & A. Rosenfield, Trans ASM, 59, p. 909, 1966.

19. F. W. Barton and W. J. Hall, Ship Structure Committee Report SSC-147 (1963).

20. J. M. Krafft, Report of NRL Progress, March, 1966, p. 6.

21. H. Logan, The Stress Corrosion of Metals, Chapter 1, Wylie, 1966.

7.0 APPENDIX

A. NOMENCLATURE

A = a constant

B = constant in high field equation

C = concentration, mole/cm^3

C^o = bulk concentration

D = diffusivity, cm^2/sec

F = Faraday, 96500 coul/equiv, or 23,060 cal/volt equiv

I = current along axis of crack in unit width specimen, amp/cm

i = current density in cross section of crack, amp/cm^2

j = current density, amp/cm^2

K = a constant

K = stress intensity factor, KSI $\sqrt{in}$ (plain strain opening mode)

ℓ = crack length to position where current enters from sides, cm

N = flux, mole/cm^2 sec

n = number of electrons in rate determining step

Q = charge density of surface species, coul/cm^2

Q_o for oxide, Q_x for halide

R = gas constant, 1.987 cal/deg mole

R_e = resistance, ohms

T = temperature, ^oK

V = crack propagation velocity, cm/sec

w = thickness, cm

Y = yield stress

y = distance from apex of crack, cm

z = equiv/mole

γ = crack angle, radians

δ = distance from crack apex to position where monolayer of oxide is complete, cm

δ^p = distance from crack apex to position where electrical double layers intersect, cm

η = overpotential, volts or mv

θ = oxide coverage, dimensionless

ρ = resistivity, ohm cm

σ = stress

τ = time, sec

ϕ = potential, volts or mv

ϕ = angle between applied stress axis and cleavage plane normal

$\Phi = \frac{F}{RT}\phi$, dimensionless potential

Subscripts

$+$ = cation

$-$ = halide ion

H = hydrogen ion

I = signifies initiation stress

IC = signifies K value of instability (fracture mechanics)

INT = signifies K level for initiation of SCC

m = metal

o = oxide

s = surface

x = halide

Superscripts

h = position in crack where hydrolysis occurs

o = bulk

p = position in crack where double layers intersect

s = pure solvent

B. EXTRACTION OF CHLORIDE FROM METAL

Recent analyses of titanium alloys have indicated chloride concentrations from less than 0.5 ppm atomic by a wet chemistry technique (3, 3rd Quarterly) to over 100 ppm atomic by mass spectrograph. Analyses are being continued by these techniques and by neutron activation to resolve the differences in analyses. In order to estimate the length of crack required to make available from the metal enough chloride to form an adsorbed monolayer in the tip zone a mean concentration of 10 ppm atomic will be assumed.

It will be further assumed that all of the chloride required for stress corrosion cracking comes from the metal in a distilled water environment and that, once extracted, the chloride is conserved in the tip zone. It will be assumed that the chloride is extracted from only the exposed surface atomic layer of metal, i.e., no diffusion from the bulk metal. Chloride is probably extracted from more than a monatomic layer and more than a monolayer of adsorbed ions are required for SCC but these two corrections are compensating. The calculation is to obtain an order-of-magnitude length only.

Consider a unit square array of metal atoms on the surface with dimensions of 10^3 x 10^3 atoms. This square would contain 10^6 metal atoms and, statistically, 10 chlorine atoms. To obtain one 10^3 atom row of chlorine atoms would require crack advancement of $10^3/10 = 100$ unit square arrays. For a tip zone of 10^{-6} cm length, the number of rows of adsorbed

chloride ions in a square array is $10^{-6}/d$, where d is the chloride ion diameter. Assuming a one-to-one correspondence of adsorbed chloride ions to surface metal atoms, the length of crack required to gather sufficient chloride ions is:

$$L = (100 \text{ units/row } Cl^-)\,(10^3 \text{ Ti atoms/unit})(d \text{ cm/Ti atom})\left(\frac{10^{-6} \text{ cm}}{d \text{ cm/row } Cl^-}\right) = 10^{-1} \text{ cm}$$

This is about the length of the fatigue crack put in the metal. Thus if the distilled water entering the crack sweeps the surface chloride to the tip (by migration) the crack could initiate immediately. Without a fatigue crack, an induction period would be required to gather chloride from the surface of the metal deformed plastically and breaking the surface oxide at the root of a notch.

If this analysis is correct the susceptibility of titanium alloys to SCC in pure non-halide containing solvents should be considerably reduced by a more complete removal of chlorine from the metal. Perhaps a small amount of silver could be added to the alloy to tie up the residual chlorine. The argument would not, of course, apply to a chloride-containing environment. Inhibition of SCC by parts per million of nitrate or sulfate in distilled water and methanol (3, 3rd Quarterly) is probably due to these ions reaching the tip zone from the environment and adsorbing and passivating (mechanism unknown) before sufficient chloride is extracted from the metal.

C. DERIVATION OF EQUATION FOR SIMPLE HYDROLYSIS MODEL

A diagramatic representation of the model is given in Figure 9 of the text. The basic assumptions are also listed in the test in connection with Figure 9.

For this system:

$$z_H = +1,\ z_- = -1$$

$$C_H = C_- = C \qquad \text{(electroneutrality)}$$

Flux equations:

$$N_- = -D_- \frac{dC}{dy} + D_- C \frac{d\Phi}{dy}$$

$$N_+ = -D_H \frac{dC}{dy} - D_H C \frac{d\Phi}{dy}$$

Relation of current density and fluxes:

$$i = F (-N_- + N_H)$$

Relation of total current to current density:

$$I = i \gamma y$$

In the region $\delta^p \lesssim y \lesssim \delta^h$:

$$N_H = 0$$

$$i = -FN_-$$

$$I = 2\, n\, Q_x\, V \qquad \text{(constant current)}$$

$$N_- = -\frac{2nQ_xV}{F\gamma\, y} = -\,2D_-\,\frac{d\,C}{dy}$$

or

$$d\,C = \frac{nQ_xV}{D_-F\gamma}\,\frac{dy}{y}$$

and

$$C = C^p + \frac{nQ_xV}{D_-F\gamma}\,\ell n\left(\frac{y}{\delta^p}\right)$$

and

$$C^h = C^p + \frac{nQ_xV}{D_-F\gamma}\,\ell n\left(\frac{\delta^h}{\delta^p}\right)$$

At limiting mass transport rate:

$$C^p << \frac{nQ_xV}{D_-F\gamma}\,\ell n\left(\frac{\delta^h}{\delta^p}\right)$$

$\therefore$ Assume $C^p = 0$

Similarly in the region $\delta^h \lesssim y \lesssim \ell$:

$$N_{-} = 0$$

$$i = FN_{H}$$

$$I = 4nQ_{x}V$$

and

$$C = C^{o} + \frac{2nQ_{x}V}{D_{H}F\gamma} \ell n\left(\frac{\ell}{y}\right)$$

and

$$C^{h} = C^{o} + \frac{2nQ_{x}V}{D_{H}F\gamma} \ell n\left(\frac{\ell}{\delta^{h}}\right)$$

Eliminating C^{h} from equations for two regions:

$$C^{o} = \frac{2nQ_{x}V}{D_{H}F\gamma}\left[\frac{D_{H}}{2D_{-}} \ell n\left(\frac{\delta^{h}}{\delta^{p}}\right) - \ell n\left(\frac{\ell}{\delta^{h}}\right)\right]$$

$$= \frac{2nQ_{x}V}{D_{H}F\gamma}\left[\ell n\left(\frac{\delta^{h}}{\delta^{p}}\right)^{\left(\frac{D_{H}}{2D_{-}}\right)} + \ell n\left(\frac{\delta^{h}}{\ell}\right)\right]$$

$$= \frac{2nQ_{x}V}{D_{H}F\gamma} \ell n \frac{\left(\delta^{h}\right)^{\left(1 + \frac{D_{H}}{2D_{-}}\right)}}{\left(\delta^{p}\right)^{\left(\frac{D_{H}}{2D_{-}}\right)} \ell}$$

Assume @ $C^{o} = 0$, $V = V^{s}$, $\delta^{h} = \delta^{hs}$:

$$(\delta^{hs}) = \left[(\delta^{p})^{\left(\frac{D_{H}}{2D_{-}}\right)} \ell\right]^{\left(\frac{1}{1 + \frac{D_{H}}{2D_{-}}}\right)}$$

Assume constant hydrolysis time:

$$\therefore \delta^{h} = \delta^{hs} \frac{V}{V^{s}}$$

and

$$C^{o} = \frac{2n\left(1 + \frac{D_H}{2D}\right) Q_x}{D_H F_Y} V \ell n \left(\frac{V}{V^s}\right)$$